The role of the NLRP3 inflammasome in neuroinflammation after neonatal hypoxic-ischemic brain injury

Doctoral thesis

to obtain a doctorate (PhD)

from the Faculty of Medicine

of the University of Bonn

Hannah Katharina Burkard

from Frankfurt am Main, Germany

2026

Written with authorization of

the Faculty of Medicine of the University of Bonn

First reviewer: Prof. Dr. med. Hemmen Sabir

Second reviewer: Prof. Dr. rer. medic. Ivo Bendix

Day of oral examination: 30.04.2026

From the Clinic and Policlinic for Neonatology and Pediatric Intensive Care

Table of contents

List of abbreviations

AHA	l-azidohomoalanine
ASC	apoptosis-associated speck-like protein with caspase recruitment domain
APC	antigen-presenting cell
APS	ammonium persulfate
ATP	adenosine triphosphate
BAX	bcl-2-associated x protein
BBB	blood-brain-barrier
BCA	bicinchoninic acid
B-cell	bursa-derived cells
BCL-2	b-cell lymphoma 2
BIS-TRIS	bis(2-hydroxyethyl)amino-tris(hydroxymethyl)methan
BSA	bovine serum albumin
CAPS	cryopyrin-associated periodic syndrome
CARD	caspase recruitment domain
CC	control + Crid3
CD	cluster of differentiation
cDNA	complementary DNA
CNS	central nervous system
Crid3	cytokine release inhibitory drug 3
CTR	control
CuAAC	copper-catalyzed azide-alkyne cycloaddition
Cys	cysteine
DAMP	damage-associated molecular patterns
DAPI	4′,6-diamidin-2-phenylindol
ddH_2O	double-distilled water
DMSO	dimethyl sulfoxide
DNA	deoxyribonucleic acid
dNTP	deoxynucleotide triphosphates
ECL	enhanced chemiluminescence
EDTA	ethylenediaminetetraacetic acid

ELISA	enzyme-linked immunosorbent assay
FACS	fluorescence-activated cell sorting
FBS	fetal bovine serum
FDR	false discovery rate
GD	glucose-deprivation
Grb2	growth factor receptor bound protein 2
GSDMD	gasdermin D
GSDMD-NT	n-terminal gasdermin D
HBSS	hank’s balanced salt solution
HI	hypoxia-ischemia
HIE	hypoxic-ischemic encephalopathy
HS	horse serum
Iba-1	ionized calcium binding adaptor molecule 1
IHC	immunohistochemistry
i.p.	intraperitoneal
IL	interleukin
LC-MS/MS	liquid chromatography-mass spectrometry/mass spectrometry
Log2FC	log^2 fold change
LPS	lipopolysaccharide
MACS	magnetic-activated cell sorting
MAPK	mitogen-activated protein kinase
MCAO	middle cerebral artery occlusion
MEM-NEAA	minimum essential medium with non-essential amino acids
MES	2-morpholinoethanesulphonic acid
MOPS	(3-(N-morpholino)propanesulfonic acid, 4-morpholino propanesulfonic Acid)
MRI	magnetic resonance imaging
MS	mass spectrometry
mTOR	mechanistic target of rapamycin
MTT	(3-(4,5-dimethylthiazol-2-yl)-2,5-diphenyltetrazolium bromide)
MWS	Muckle-Wells-Syndrome
NaCl	sodium chloride

NE	neonatal encephalopathy
NEK7	NIMA-related kinase 7
NFκB	nuclear factor 'kappa-light-chain-enhancer' of activated B-cells
NIMA	never in mitosis gene a
NK	natural killer
NLR	NOD-like receptor
NLRP3	NOD-like receptor family pyrin domain-containing protein 3
NOD	nucleotide-binding oligomerization domain
NOR	novel object recognition
OC	OGD + Crid3
OD	oxygen-deprivation
OGD	oxygen-glucose-deprivation
P4hb	prolyl 4-hydroxylase subunit beta
PAMP	pathogen-associated molecular patterns
PBS	phosphate-buffered saline
PCR	polymerase chain reaction
PE	Phycoerythrin
Pen/Strep	penicillin/streptomycin
PFA	paraformaldehyde
PI	propidium iodide
PLL	poly-L-lysine
PRR	pattern recognition receptor
Psma8	proteasome 20S subunit alpha 8 [
Psmb3	proteasome 20S subunit beta 3
Psme2	proteasome activator subunit 2
Ptprz1	protein tyrosine phosphatase receptor type Z1
RIPA	radioimmunoprecipitation assay
RNA	ribonucleic acid
ROS	reactive oxygen species
RT	room temperature
RT-PCR	reverse transcription polymerase chain reaction
s.c.	subcutaneous

SDS-PAGE	sodium dodecyl sulfate - polyacrylamid gel electrophoresis
siRNA	small interfering RNA
SN	supernatant
STING	stimulator of interferon genes
TBI	traumatic brain injury
TBS	tris-buffered saline
TBS-T	tris-buffered saline with tween20
T-cell	thymus-dependent lymphocytes
TCR	t-cell-receptor
TGF-β	transforming growth factor beta
TLR	toll-like receptor
TMB	3,3',5,5'-tetramethylbenzidine
TNF	tumor necrosis factor
Tollip	toll interacting protein
T_{rec}	rectal temperature
UV	ultraviolet

1 Introduction

1.1 Hypoxic-ischemic encephalopathy

Neonatal hypoxic-ischemic encephalopathy (HIE) describes the pathology of brain damage and its consequences after a hypoxic-ischemic event before, during and after birth. The neonates suffer from brain damage due to an oxygen lack in the brain which may lead to mild to severe encephalopathies. Neonatal HIE occurs when the brain is not provided with enough blood and oxygen to maintain oxidative metabolism (Vannucci, 1990). The metabolism has to shift towards anaerobic glycolysis and cannot provide enough energy anymore, which results in energy failures and cell death if not shifting back (Vannucci, 1990; Rocha-Ferreira and Hristova, 2016). The immature brain consumes a high amount of oxygen; consequently, it is more susceptible to oxygen depletion (Demarest et al., 2016; Qin et al., 2019). The consequences of these energy failures in the brain are determined by the severity of the insult and the stage of brain development (Rocha-Ferreira and Hristova, 2016; Ranjan and Gulati, 2023). Depending on these circumstances, HIE can lead to impaired neurological and motor functions, disability and to neonatal death (Tagin et al., 2015; Ehlting et al., 2022; Ranjan and Gulati, 2023).

HIE is affecting neonates all around the world. In developed countries, there are 1.5 cases per 1000 live births (Kurinczuk et al., 2010). HIE especially has an impact on low-income countries as the incidence is 10- to 20-fold higher compared to high-income countries (Kurinczuk et al., 2010; Lee et al., 2013; Thayyil et al., 2021). In a population-based study including 125 million babies born in 2010 worldwide, 717,000 neonatal deaths, 1,200,000 stillbirths, and 1,150,000 cases of neonatal encephalopathy (NE) were recorded (Lee et al., 2013). 413,000 cases of NE showed neurodevelopmental impairment; the number of long-term disability cases could not be determined (Lee et al., 2013). Based on the severity of the insult, HIE is categorized into mild, moderate and severe HIE (Lee et al., 2013; Ranjan and Gulati, 2023). Additionally, several factors can influence the pathology of HIE. Maternal factors, placental pathologies, genetics and perinatal infections play a role in the progress of HIE (Kurinczuk et al., 2010; Danladi and Sabir, 2021; Ranjan and Gulati, 2023).

1.1.1 Phases of HIE

Hypoxia-Ischemia (HI) is characterized by a low blood and oxygen flow to the brain. The resulting reduction in energy metabolism leads to a primary energy failure. During this phase, the adenosine triphosphate (ATP) and glucose levels decrease and there is an increased glutamate release and calcium influx which all together can lead to cell death. Thereafter, a latent phase follows for recovery and homeostasis. Eventually, the insult is leading to a secondary energy failure. Characterized by oxidative stress, excitotoxicity and inflammation, this phase results in cell death. Subsequently, the tertiary energy failure can last for months, characterized by brain remodeling and cell repair (figure 1) (Rocha-Ferreira and Hristova, 2016; Luo et al., 2021; Tetorou et al., 2021).

Between the first and second energy failure phases, there is a time period for therapeutic interventions. Up to 6 hours after the insult, therapies can reduce the development of the second energy failure and rescue cell death and tissue damage. In contrast, therapies applied too late can worsen the damage (Sabir et al., 2012; Luo et al., 2021; Chen et al., 2023b).

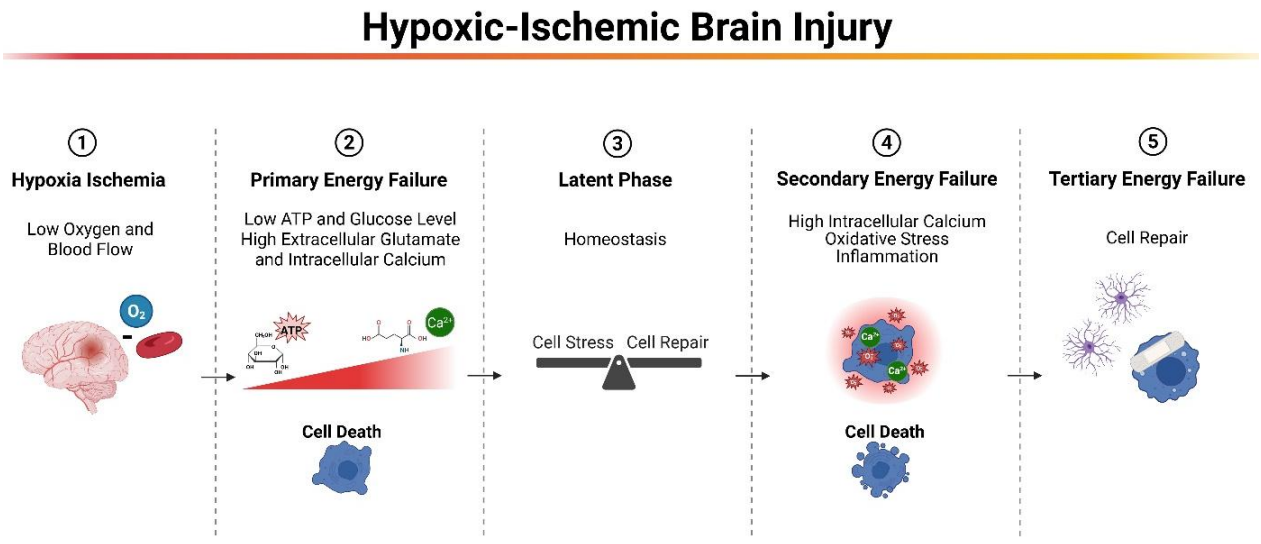

Figure 1: Phases of hypoxic-ischemic brain injury. Hypoxia-ischemia is described by low oxygen and blood flow to the brain, which leads to several energy failures and cell death in the brain. Created with BioRender.com.

1.1.2 Therapeutic hypothermia

Therapeutic hypothermia (HT) is the sole therapy regularly used for treating newborns with moderate to severe HIE. By cooling the body temperature to 33-34 °C for 72 hours, the metabolism is downregulated (Rosomoff and Holaday, 1954; Zhou et al., 2022). With every decreasing degree of body temperature, the metabolic rate decreases by 6-7 % (Rosomoff and Holaday, 1954). The effect of HT is anti-inflammatory, anti-excitatory and thereby suppresses cell death and damage (Zhou et al., 2022). In animal models, HT provides neuroprotection within 6 hours after the insult and improves motor long-term functions (Sabir et al., 2012; Ehlting et al., 2022). Nonetheless, the application and efficacy of HT has its restrictions. Using HT in a model of pre-sensitized inflammatory HI, HT is not neuroprotective (Osredkar et al., 2014; Osredkar et al., 2015). When treating the animals after the treatment window of 6 hours, HT even increases the brain injury following HI (Sabir et al., 2012). The search for additional or replacing treatments is ongoing to provide a reliable treatment option for HIE.

1.1.3 Lipopolysaccharide

Lipopolysaccharide (LPS) is a glycolipid and part of the outer membrane of gram-negative bacteria where it fulfills the function of stabilization and integrity (Yang et al., 2020a; Skrzypczak-Wiercioch and Sałat, 2022). In animals, it induces inflammatory responses and therefore is used as an inflammation model (Seemann et al., 2017; Skrzypczak-Wiercioch and Sałat, 2022). The pre-sensitization with LPS causes increased brain area loss, microglia activation and neuronal injury in a HI model (Serdar et al., 2019). LPS promotes increased cytokine levels (Qiu et al., 2019; Beyer et al., 2020; Akbal et al., 2022), eventually via the nucleotide-binding oligomerization domain-like receptor family pyrin domain-containing protein 3 (NLRP3) pathway, as the NLRP3 pathway proteins show increased protein and mRNA levels after LPS treatment (Qiu et al., 2019). Additionally, using NLRP3 inhibitors, the inflammatory effect of LPS can be prevented (Qiu et al., 2019).

1.2 Immune system

The immune system provides protection against pathogens. Its anatomical and physiological barriers prevent the intrusion with an intact skin, ciliary clearance mechanisms, a low stomach pH and bacteriolytic lysozyme in tears, saliva and other secretions (Turvey and Broide, 2010).

When the pathogen comes through this barrier, the innate immune system represents the first answer to invading pathogens. Macrophages, neutrophils, eosinophils, basophils, mast cells, dendritic cells and natural killer (NK) cells distinguish foreign cells and respond via releasing cytokines and other chemicals initiating an inflammatory reaction. These components of the innate immunity can be short-lived as neutrophils or long-lived as macrophages and target various pathogens from parasites to bacteria and viruses to tumor cells. Macrophages can act by presenting pathogen molecules on their surface to activate thymus-dependent lymphocytes (T-cells). Neutrophils and NK cells directly interact with invading cells and eliminate them (Turvey and Broide, 2010; Marshall et al., 2018). The complement system recruits immune cells to the infection site and bridges the innate with the adaptive immune system.

In contrast to the innate immune system, the adaptive immune system reacts delayed via thymus-dependent lymphocytes (T-cells) and bursa-derived cells (B-cells). It is antigen-dependent and antigen-specific and has an immunologic memory. It recognizes the antigens and generates the answer via activating eliminating pathways (Turvey and Broide, 2010; Marshall et al., 2018) (figure 2).

When the immune system is dysregulated, it can lead to overactivation (hypersensitivity), to an unwarranted reaction to the own system (autoimmunity), and to impaired immune responses (immunodeficiency) (Marshall et al., 2018).

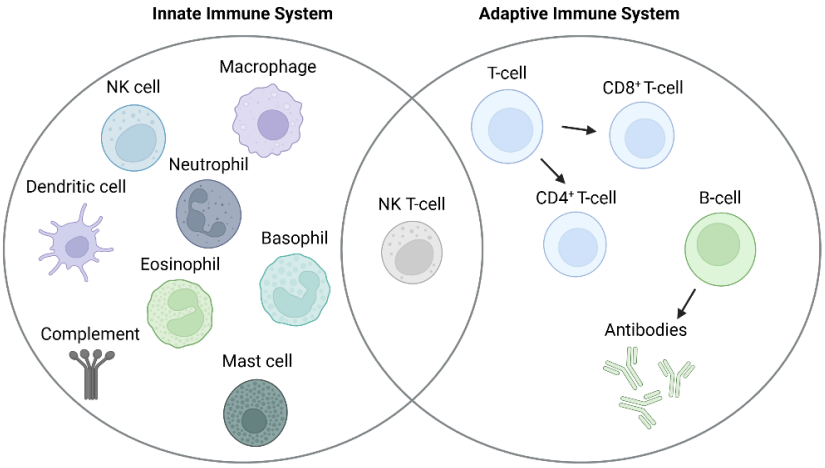

Figure 2: Components of the immune system. The left circle contains the innate immune system and the right circle describes the adaptive immune system. Created with BioRender.com.

1.2.1 Microglia

Within the central nervous system (CNS), immune responses are primarily mediated by microglia, the resident immune cells of the brain. They derive from primitive macrophages in the embryonic yolk sac and migrate into the brain to distribute throughout the CNS (Ajami et al., 2007; Ginhoux et al., 2010; Stratoulias et al., 2019; Paolicelli et al., 2022; Isik et al., 2023). In the brain, there are long-lived and maintained by local self-renewal (Ajami et al., 2007; Askew et al., 2017; Paolicelli et al., 2022). They fulfill the function of sensing changes in their environment and respond dynamically to them. Microglia are the first cells reacting to brain pathologies (Ajami et al., 2007; Ni and Aschner, 2010). They change their morphology and function depending on the invading target (Stratoulias et al., 2019; Paolicelli et al., 2022). As mediators of inflammation, infection, trauma and neurodegenerative diseases, they produce pro- and anti-inflammatory cytokines, prostaglandins and interleukins (Ni and Aschner, 2010; Stratoulias et al., 2019; Jiang et al., 2020a; Bernis et al., 2022; Isik et al., 2023). Consequently, they can contribute to cellular damage but also dampen it and recruit other immune cells (Ajami et al., 2007; Ni and Aschner, 2010). Microglia can communicate with each other and other cell types by releasing different molecules (Stratoulias et al., 2019; Borst et al., 2021; Isik et al., 2023). In the case of neurons, they express a wide range of receptors, which are targeted by released molecules of microglia. Thereby, microglia can regulate neuronal functions and

lead to apoptosis and cell stress in neuronal cells (Wen et al., 2006; Bessis et al., 2007; Dai et al., 2015; Marinelli et al., 2019; Wang et al., 2023a). Conversely, microglia are also dependent on neuronal signaling (Biber et al., 2007).

1.2.1.1 Functions of microglia

The role of microglia can be neuroprotective as well as neurotoxic (Goshi et al., 2020; Isik et al., 2023). They are involved in neurogenesis, synapse remodeling, neuronal function, tissue repair, inflammation and blood-brain-barrier (BBB) permeability (Paolicelli et al., 2022). Microglia exhibit a variety of different states and they can switch dynamically between them (Peferoen et al., 2015; Paolicelli et al., 2022). The states determine the function of the cells. As the morphology, ultrastructure and molecular profile of the cells change within different states, the cells can release pro-inflammatory cytokines like tumor necrosis factor-alpha (TNF-α) or interleukin-6 (IL-6) and promote neuronal degeneration and oxidative stress, or they can release anti-inflammatory cytokines like transforming growth factor beta (TGF-β) and lead to phagocytosis and neuronal survival (Peferoen et al., 2015; Isik et al., 2023).

The morphology of microglia depends on the dynamic microtubules which are regulated depending on the stimulation of the cells (Adrian et al., 2023). Homeostatic microglia have a ramified phenotype with elongated dendrites, whereas microglia responding to a signal transform towards an amoeboid shape to enable migration through the parenchyma (Zhou et al., 2017; Goshi et al., 2020). Microglia can differ across brain regions and fulfill different functions because of their regional heterogeneity (Tan et al., 2020).

1.2.1.2 Microglia and HI

In response to HI, microglia express a state, promoting the pro-inflammatory cytokine release at an early time point (24 hours) (Hellström Erkenstam et al., 2016; Serdar et al., 2019). HIE leads to pyroptosis, descended by microglia activation (Lv et al., 2020). Pyroptosis is an inflammatory form of cell death. The formation of membrane pores causes cell swelling and membrane rupture, leading to the release of pro-inflammatory intracellular content (Bergsbaken et al., 2009; Rayamajhi et al., 2013; Sagulenko et al., 2013; Swanson et al., 2019). At later time points, anti-inflammatory cytokines are

released, supporting the recovery after the insult (Hellström Erkenstam et al., 2016; Serdar et al., 2019). In models of pre-sensitized HI with LPS, the same trend is visible. The activation of microglia after HI also appears by an upregulation of the protein NLRP3 at an early time point after the insult (Serdar et al., 2020; Bernis et al., 2022).

1.3 NLRP3

The NLRP3 (nucleotide-binding oligomerization domain-like receptor family pyrin domain-containing protein 3) inflammasome complex is part of the innate immune system and well described in the literature; however, its precise role in inflammatory processes remains to be fully elucidated (He et al., 2023). It is expressed in microglia, astrocytes, neutrophils and neurons (Ystgaard et al., 2015; Gong et al., 2018; Serdar et al., 2020; Kaufmann et al., 2022; Paget et al., 2022; Wu et al., 2023a) and mediates inflammatory responses and thereby needs to be tightly regulated (Menu and Vince, 2011; Mangan et al., 2018).
NLRP3 is a tripartite protein, consisting of an amino-terminal pyrin domain (PYD), a nucleotide-binding domain (NACHT) and a carboxy-terminal leucine-rich repeat (LRR). The function of PYD represents the recruitment of the apoptosis-associated speck-like protein with caspase recruitment domain (ASC) to form the inflammasome complex. The NACHT domain possesses ATPase activity, whereas the LRR binds (never in mitosis gene a)-related kinase 7 (NEK7) to activate the inflammasome complex and has auto-inhibition as well as recognition functions (figure 3) (Mangan et al., 2018; Swanson et al., 2019; He et al., 2023).

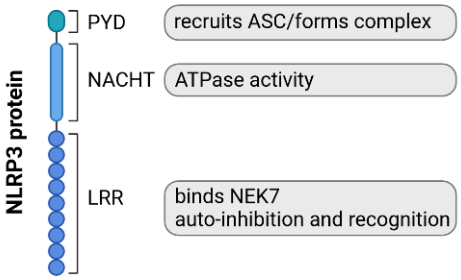

Figure 3: NLRP3 domains and their functions. Created with BioRender.com.

Upon activation, the NLRP3 inflammasome complex oligomerizes. The c-terminal lobe of the serine/threonine kinase NEK7 binds to the LRR and NACHT domains of NLRP3, thereby facilitating the complex formation (Chen et al., 2019a; Sharif et al., 2019; Leu et

al., 2023). The NACHT domains of NLRP3 interact with each other and the PYD domains of NLRP3 interact with the PYD domains of ASC to build a platform recruiting caspase-1. Consequently, caspase-1 assembles with the complex via CARD-CARD interactions (Kelley et al., 2019; Swanson et al., 2019; Paget et al., 2022). NLRP3 represents the sensor, ASC the adaptor and caspase-1 the effector of the inflammasome complex. Caspase-1 is activated through proximity-induced self-cleavage to cleaved caspase-1 (Mangan et al., 2018; Kelley et al., 2019; Swanson et al., 2019; He et al., 2023). When activated, caspase-1 cleaves and activates the interleukins pro-IL-1β and pro-IL-18 and the protein gasdermin D (GSDMD) (Downs et al., 2020; McKee and Coll, 2020; O'Brien et al., 2020). GSDMD is cleaved into two domains, the c-terminal GSDMD-CT and the n-terminal GSDMD-NT. GSDMD-NT translocates to the plasma membrane where it binds to lipids in the membrane. Upon oligomerization, GSDMD-NT assembles into a stable ring-like structure, thereby forming pores in the membrane with an inner diameter of 10–16 nm (Ding et al., 2016; Liu et al., 2016; Xia et al., 2020). The cleaved and activated interleukins can pass through these pores and lead to pyroptosis (figure 4) (Bergsbaken et al., 2009; Liu et al., 2016).

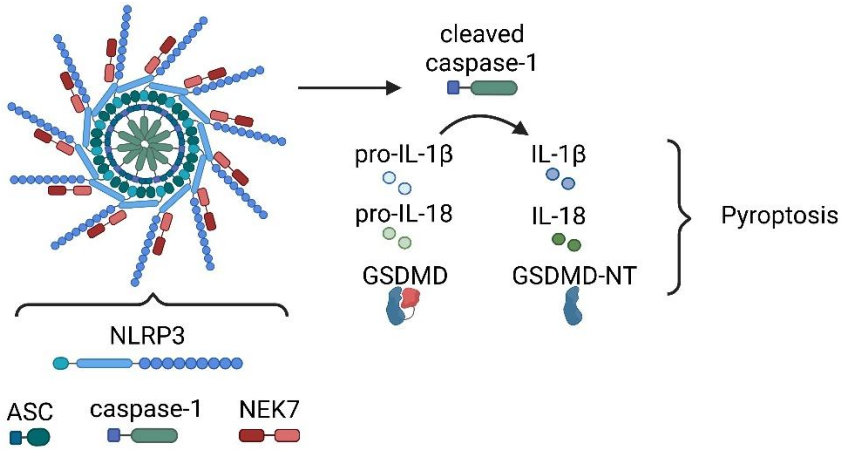

Figure 4: NLRP3 inflammasome. The inflammasome consists of NLRP3, ASC, caspase-1 and NEK7. Activated by self-cleavage, caspase-1 processes interleukins and GSDMD to their active forms, leading to pyroptosis. Created with BioRender.com.

1.3.1 Canonical pathway

The activation of the NLRP3 inflammasome results from different processes within the cell. Describing the canonical NLRP3 pathway, there are two different essential signals

for the oligomerization of the complex. The priming signals lead to the transcription of the components and the activation signals lead to the complex formation (figure 5).

Briefly, pathogens and other damages cause pathogen- and damage-associated molecular patterns (PAMP/DAMP) which are recognized by toll-like receptors (TLR) on the cell membrane. Downstream of the TLR, nuclear factor 'kappa-light-chain-enhancer' of activated B-cells (Nf-κB) is stimulated and initiates the transcriptional upregulation of NLRP3 and pathway components. NLRP3 can be post-translational modified by phosphorylation, sumoylation or ubiquitination and thereby changes its characteristics (Kelley et al., 2019; Swanson et al., 2019). Subsequently, different activation signals can lead to the oligomerization of the complex components. Mitochondrial dysfunction, reactive oxygen species (ROS), potassium (K^+) efflux, chloride (Cl^-) efflux, calcium (Ca^{2+}) signaling and lysosomal destabilization promote the protein interaction of NLRP3, NEK7, ASC and caspase-1. Upon oligomerization, the NLRP3 inflammasome becomes active and exerts its effector function via caspase-1 activation and leads to pyroptosis as described in the NLRP3 section (figure 5) (McKee and Coll, 2020; O'Brien et al., 2020; Paget et al., 2022; He et al., 2023).

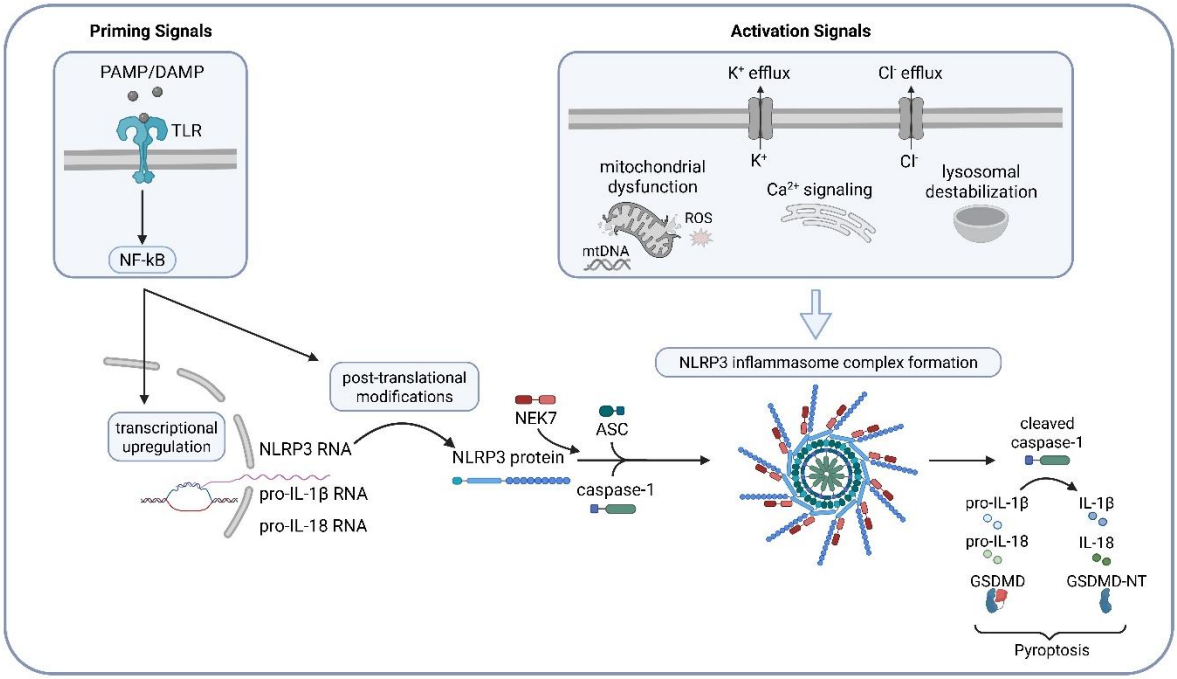

Figure 5: Canonical pathway of NLRP3 activation. Priming signals lead to the transcriptional upregulation of the NLRP3 pathway components. NLRP3 can undergo post-translational modifications before NLRP3 inflammasome complex formation through activation signals. Inflammasome activation leads to cleavage of interleukins and GSDMD and thereby to pyroptosis. Created with BioRender.com.

1.3.2 Non-canonical pathway

The non-canonical pathway is stimulated by gram-negative bacteria and lipopolysaccharide (LPS) in contrast to the canonical pathway, which reacts to stimuli of gram-positive bacteria (Falck et al., 2017; Kelley et al., 2019). TLR4 may support the upregulation of caspase-11 transcription (Falck et al., 2017; Downs et al., 2020; Paget et al., 2022; Skrzypczak-Wiercioch and Sałat, 2022; He et al., 2023). Subsequently, caspase-11 interacts with the PYD and LRR domains of NLRP3, leading to the formation of the NLRP3 inflammasome complex and subsequent caspase-11 activation (Accogli et al., 2023). Consequently, cleaved caspase-11 cleaves GSDMD into its subunits and GSDMD-NT forms pores in the membrane, which together with the interleukins resulting from the NLRP3 inflammasome activation, induces pyroptosis (figure 6) (Downs et al., 2020; Paget et al., 2022; He et al., 2023).

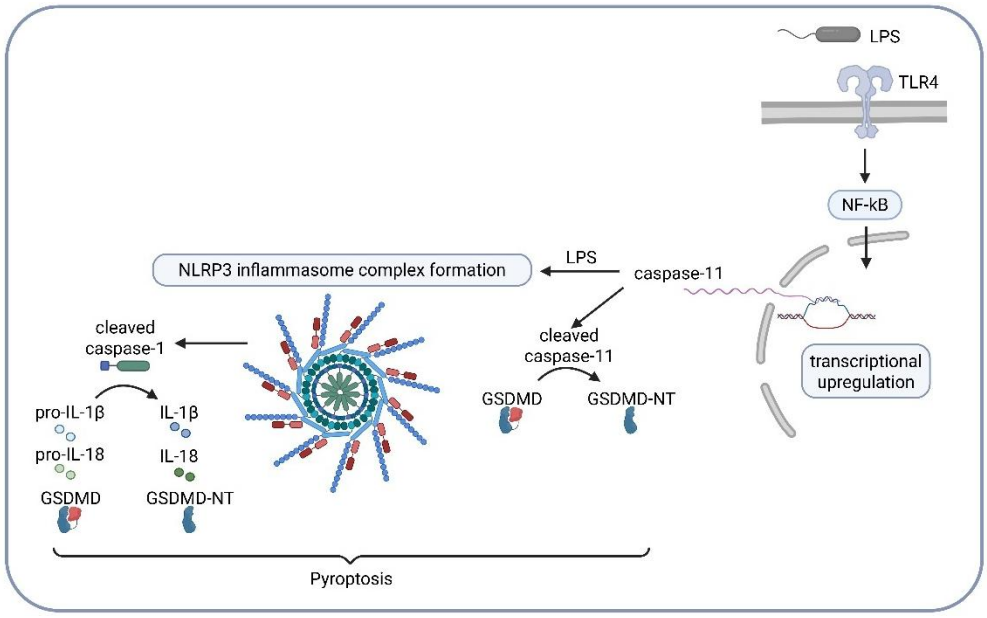

Figure 6: Non-canonical pathway of NLRP3 activation. LPS and gram-negative bacteria trigger the transcriptional upregulation of caspase-11. The NLRP3 inflammasome complex formation is induced by interaction with activated caspase-11. Interleukins and GSDMD are cleaved and lead to pyroptosis. Created with BioRender.com.

1.3.3 Posttranslational modifications

During the priming step of the NLRP3 inflammasome pathway, NLRP3 can undergo different post-translational modifications. NLRP3 can be phosphorylated, sumoylated or ubiquitinated. These modifications can promote the activity of NLRP3 and the formation

of the inflammasome complex or negatively regulate it (Mangan et al., 2018; Kelley et al., 2019; Swanson et al., 2019; Yang et al., 2019; McKee and Coll, 2020). Figure 7 shows some examples of positive- and negative-regulatory modifications. Song et al. could show that c-Jun N-terminal kinase (JNK1)-mediated NLRP3 phosphorylation represents an essential modification for the following inflammasome activation (Song and Li, 2018).

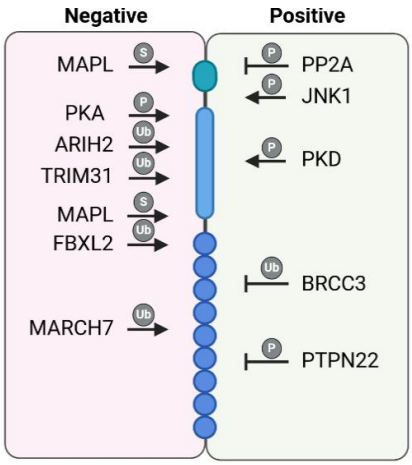

Figure 7: Posttranslational modifications of NLRP3. Negative modification regarding the NLRP3 inflammasome activity are presented on the left side, positive modifications on the right side. Phosporylation (P), sumoylation (S) and ubiquitination (Ub) are indicated with circles above the arrows. Inhibitory arrows indicate dephosporylation and deubiquitination. Modified after Kelley et al. and Swanson et al. (Kelley et al., 2019; Swanson et al., 2019). Created with BioRender.com.

1.3.4 NLRP3 and diseases

The activation of the NLRP3 inflammasome promotes inflammatory processes in the brain. Neuroinflammation can lead to Aβ accumulation, synapse loss and neurodegeneration, leading to the progress of Alzheimer's disease (Yang et al., 2020b). Inflammatory processes are involved in many pathologies, possibly supported by the excessive activation of the NLRP3 inflammasome complex. Connections could be uncovered between NLRP3 and traumatic brain injury (TBI), stroke, Parkinson's disease and inflammatory bowel disease (Mangan et al., 2018; Yang et al., 2020b; Das et al., 2021; Wang et al., 2022a; He et al., 2023; Zhang et al., 2023). A gain-of-function mutation in NLRP3 causes the cryopyrin-associated periodic syndrome (CAPS, e.g. Muckle-Wells-syndrome). CAPS is an autoinflammatory disorder described by systemic inflammation (Mangan et al., 2018; Booshehri and Hoffman, 2019).

1.3.5 NLRP3 and HIE

After HI the NLRP3 inflammasome is stimulated. HI leads to processes in the cells which trigger the oligomerization and activation of the inflammasome complex. In rat models of HIE, it was shown that the protein NLRP3, as well as the NLRP3 pathway proteins and effectors of pyroptosis, are upregulated after HI (Ystgaard et al., 2015; Lv et al., 2020; Li et al., 2021; Chen et al., 2023a).

One of the cell types responsible for NLRP3 upregulation are microglia. Isolated microglia following inflammation-sensitized HI brain injury in a neonatal rat HIE model showed increased NLRP3 protein levels at 24 hours after the insult (Serdar et al., 2020). In another neonatal HI animal model, NLRP3 and pathway components were shown to be upregulated at the gene expression level in isolated microglia, particularly at 24 and 48 hours after the hypoxic event (Bernis et al., 2022). Lv et al. presented results indicating that the NLRP3 pathway is essential for microglia pyroptosis and activation after neonatal HIE (Lv et al., 2020).

1.3.6 NLRP3 Inhibitors

Activation of the NLRP3 inflammasome complex leads to pyroptosis and thereby increased inflammatory processes in the brain. To prevent further damage due to excessive NLRP3 activation in pathologies, inhibitors are tested. To inhibit pyroptosis downstream of the NLRP3 inflammasome, there are many pathway components to target (figure 8) (Yang et al., 2019; Das et al., 2021; Blevins et al., 2022; Zhang et al., 2023).

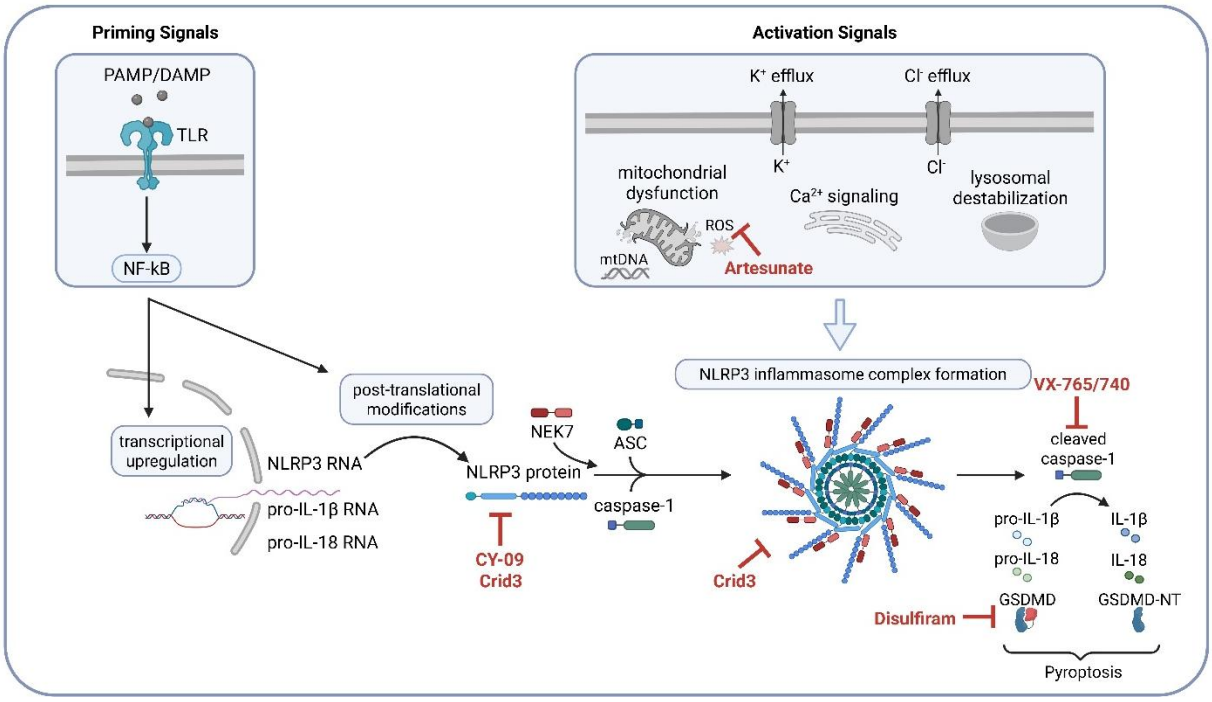

Figure 8: Schematic overview of exemplary NLRP3 inhibitors. The NLRP3 is targeted by inhibitors at different pathway components (red arrows). CY-09 binds to the ATP-binding motif in the NACHT domain and thereby blocks the ATPase activity and inflammasome formation (Jiang et al., 2017; Mangan et al., 2018; Wang et al., 2022b). Crid3 inhibits the ATPase-activity of NLRP3 NACHT domain and thereby inflammasome activation (Coll et al., 2019). Artesunate blocks the ROS-induced inflammasome formation (Liu et al., 2018; Wang et al., 2023b; Xie et al., 2023). VX-765 and VX-740 are caspase-1 inhibitors that covalently bind to the catalytic cysteine residue of caspase-1, thereby blocking its activity (Boxer et al., 2010; MacKenzie et al., 2010). Disulfiram covalently modifies cysteine residues in GSDMD, leading to inhibition of pore formation and pyroptosis (Hu et al., 2020; Blevins et al., 2022; Zhang et al., 2023). Created with BioRender.com.

1.3.6.1 Crid3

Crid3 (cytokine release inhibitory drug 3), also called MCC950, is a specific NLRP3 inhibitor (Coll et al., 2015; Coll et al., 2019). It directly binds to the NLRP3 NACHT domain, resulting in the inhibition of its ATPase-activity (Coll et al., 2019). Briefly, using cryo-electron microscopy, it was shown that Crid3 binds into a cleft between the NACHT domains and thereby stabilizes the NACHT and LRR domains, preventing them to transform into the active state of the inflammasome (Hochheiser et al., 2022). The specificity of this inhibition arises from the Crid3 central sulfonylurea group binding to the Walker A motif of the NLRP3 NACHT domain (Hochheiser et al., 2022).

The treatment with Crid3 leads to a reduced expression of NLRP3 pathway proteins. This was presented in mouse models of ischemic stroke (Bellut et al., 2021), cardiopulmonary resuscitation (Jiang et al., 2020b), spinal cord injury (Jiao et al., 2020) and middle cerebral artery occlusion (MCAO) (Wu et al., 2023a). Crid3 had a positive effect on the well-being of the animals. Treated animals showed less infarct volume, a higher survival rate, improved motor functions and less neurological deficits (Jiang et al., 2020b; Jiao et al., 2020; Bellut et al., 2021). In the rat model of cardiac arrest (Chang et al., 2020) and neonatal hypoxic ischemic brain damage (Lv et al., 2020), similar effects were observed. NLRP3 pathway proteins were downregulated and brain injury was reduced (Chang et al., 2020; Lv et al., 2020). Crid3 decreases microglia activation and inflammatory processes (Dempsey et al., 2017; Lv et al., 2020; Liu et al., 2022b; Hou et al., 2024). Thereby it can be used to study the influence of the NLRP3 inflammasome in different pathology models. As clinical tryouts with Crid3 resulted in liver toxicity when using high concentrations, the use of this inhibitor for now is only serving mechanistic studies (Li et al., 2022).

1.4 Aim of the thesis

This project is designed to comprehend the mechanism of the NLRP3 inflammasome activation in the context of neonatal HIE. As the number of current treatment options for HIE is low and the efficacy of those treatments is limited, the need for new treatment approaches is of global interest. Inflammation in the brain can be one of the reasons why there is not always a response to therapies as effective as therapeutic hypothermia. To address this potential source of therapeutic failure, this project focuses on the NLRP3 inflammasome, a central mediator of inflammation in the brain.

Based on previous experiments from our group demonstrating NLRP3 upregulation in microglia following HIE, this project was designed to focus specifically on microglial NLRP3. NLRP3 is closely linked to the pathophysiology of HIE; however, the precise mechanisms underlying its involvement remain unclear. In this project, I aimed to elucidate the role of NLRP3 inflammasome pathway activation in our neonatal HIE model and to characterize microglial engagement in NLRP3 signaling and inhibition. By defining NLRP3 activation, particularly within microglia, this work brings us one step closer to identifying effective therapies for HIE by providing a cell-specific target for therapeutic intervention.

2 Material and methods

2.1 Material

2.1.1 Equipment

Table 1: Equipment.

Equipment	**Product / Company**
Balances	Explorer E01140, OHAUS Science Education Precision Balance, VWR
Centrifuges	Labnet™ CENTRIFUGE 8X1,5ML PRISM MINI, Fisher Scientific Multifuge X3R, ThermoFisher Scientific Centrifuge 5415 R, Eppendorf
Concentrator	Concentrator Plus, eppendorf
Flasks	Simax
Freezer	Ultra Low Temperature Freezer, Sanyo / Liebherr
Gel electrophoresis chambers	XCell SureLock Mini-Cell, Invitrogen Mini-PROTEAN Tetra Vertical Electrophoresis Cell, Bio-Rad
Gel electrophoresis power supplies	Power Source 300V, VWR PowerPac™ Basic Power Supply, Bio-Rad
Heating blocks	ThermoMixer F1.5/ThermoMixer C, Eppendorf
Hypoxia chamber cell culture	Invivo$_2$ 400, Baker Ruskinn
Ice machine	Manitowoc
Imager for Western Blot membranes	Licor Odyssey iBright 1500, Invitrogen Thermo Fisher Scientific Fusion FX edge, Vilber
Incubator	ICO 240, memmert Incubator INE 400, memmert
Laminar flow hood	Scanlaf Mars Pro, Labogene
MACS Multistand	MACS® MultiStand, 130-042-303, Miltenyi Biotech
MACS Octo Separator	OctoMACS™ Separator, 130-042-109, Miltenyi Biotech
MACS Quadro Separator	QuadroMACS™ Separator, 130-091-051, Miltenyi Biotech
Microplate reader	FLUOstar Omega, BMG Labtech
Microscope	OZL 445, Kern Optics Primovert, Zeiss LSM800, Zeiss ZOE Fluorescent Cell Imager, Bio-Rad
Microtome	Leica RM 2255, Leica
Modular Tissue Embedding Center	Leica EG1150, Leica

Nanodrop	DeNovix DS-11, DeNovix
Neubauer counting chamber	Neubauer improved, Brand
Orbitrap Exploris 480 mass spectrometer	Thermo Fisher Scientific
pH Meter	Accumet AE150, Fisher Scientific
Paraffin pastilles	VWR (Merck Millipore)
PCR cycler	QuantStudio™ 3 Real-Time PCR System, Thermo Fisher Scientific
Pipettes	Gilson / eppendorf / Multipipette E3, eppendorf / Integra Pipetboy 2, Integra
Plate shaker	Corning® LSE™ Low Speed Orbital Shaker, Corning
Surgical instruments	Dumont
Thermocycler	T3000, Biometra
Tissue Processor	TP1020 Automatic Benchtop Tissue Processor, Leica
Vanquish Neo UHPLC	Thermo Fisher Scientific
Vortex shaker	Mini Vortexer, Heathrow Scientific
Waterbath	memmert
Water pad	Water pad - cover, Hico

2.1.2 Consumables

Table 2: Consumables.

Consumables	**Company**
Adhesive microscope slides Superfrost® Plus	Menzel
Amicon® Ultra Centrifugal Filter, 3 kDa MWCO	Millipore
Amicon® Ultra Centrifugal Filter, 10 kDa MWCO	Millipore
Cassettes (1.5 mm)	life technologies
Cell culture microplate, 96-well, flat-bottom	greiner bio-one
Cell scraper	TPP Techno Plastic Products AG
Cell strainer, 40 µm	Fisher Scientific
Cell strainer, 70 µm	Sarstedt
Centrifuge tubes (15 ml/50 ml)	nerbe plus
CombiTips Advanced®	eppendorf
Cover slips, 12 mm	epredia
Culture flasks (T75)	greiner bio-one /Sarstedt
Culture plates (6-well/ 24-well)	greiner bio-one / Thermo Fisher Scientific
Empore™ SDB-RPS Extraction Disks	CDS

Gelloader Pipette Tips	Sarstedt
Gloves	Kimtech
LS columns (130-042-401)	Miltenyi Biotech
MicroAmp™ EnduraPlate™ Optical 96-well Fast Clear Reaction Plates	Thermo Fisher Scientific
Microplate BCA™ Protein-Assay-Kit	Thermo Fisher Scientific
Microscope Cover Glasses	Glasswarenfabrik Karl Hecht GmbH
Microscope slides	avantor by VWR
MS columns (130-042-401)	Miltenyi Biotech
Multiply®-µStrip Pro 8-strip	Sarstedt
Needle 25Gx	Terumo
Petri dishes	Corning / Sigma Aldrich
Pipette tips (epT.I.P.S.® Reloads)	eppendorf
SafeSeal tube (1.5 ml/2 ml)	Sarstedt
Scalpel	Disposable Scalpels, Sterile, Swann Morton
Serological pipettes (5 ml/ 10 ml/ 25 ml)	Cellstar®, greiner bio-one
Syringe Omnifix-F Luer Solo 1ml	Braun
Transfer Membrane (Immobilon®-FL)	Merck

2.1.3 Chemicals

Table 3: Chemicals.

Chemicals	**Catalog number**	**Company**
Acrylamide - Solution (40 %)	A0385,0500	PanReac AppliChem
AHA	HAA9280	Iris Biotech
APS	20241.06	Bernd Kraft
ascorbic acid	A92902	Sigma-Aldrich
β-Mercaptoethanol	63689	Sigma-Aldrich
Bis-Tris	9140.2	Roth
BSA	A3294	Sigma-Aldrich
Bromphenol blue	B0126	Sigma-Aldrich
Bupresol	1204	cp pharma
CD11b/c (Microglia) MicroBeads, rat	130-105-634	Miltenyi Biotech
Chameleon® Duo Pre-stained Protein Ladder	928-60000	LI-COR
CHAPS	220201	Sigma-Aldrich
Chloralhydrate	K318.3	Carl Roth
Chloroform	1.02445.1000	Merck Millipore

cOmplete™, Mini, EDTA-free Protease Inhibitor Cocktail	11836170001	Roche
Crid3	5479	Tocris
Crid3 (for animal experiments)	5.3812	Sigma-Aldrich
Dimethyl Sulfoxide for cell culture	A3672,0250	PanReac AppliChem
DMEM medium	P04-05540	Pan Biotech
DMEM medium, no methionine	21013024	gibco
DMEM medium, without glucose	11966025	gibco
DMEM medium, without phenolred	P04-01161	Pan Biotech
ECL chemicals: SuperSignal West Pico Plus Chemiluminescent Substrate	34577	Thermo Fisher Scientific
EDTA	AM9261	Invitrogen
Ethanol	39556.02	Serva
Fetal bovine serum	P30-3306	Pan Biotech
Fluoromount-G™ Mounting Medium, with DAPI	00-4959-52	Invitrogen
formic acid	5330020050	Merck
Glycerol	G9012	Sigma-Aldrich
Glycine	3908.2	Carl Roth
Goat serum	31873	Thermo Fisher Scientific
guanidinium chloride	G3272	Merck
HBSS, sterile	P04-50500	Pan Biotech
HBSS 10x, calcium, magnesium, no phenolred	14065056	gibco
HEPES	15630080	Thermo Fisher Scientific
High Capacity cDNA Reverse Transcription Kit	4368814	Thermo Fisher Scientific
Horse serum	P30-0702	Pan Biotech
λ-Carrageenan	22049	Sigma-Aldrich
LC-MS-grade acetonitrile	A955-4	Thermo Fisher Scientific
Lipopolysaccharides from Escherichia coli	L6529	Sigma-Aldrich
MEM Non-Essential Amino Acids Solution	11140050	gibco
MES SDS Running Buffer (20x)	NP0002	Invitrogen
Methanol	AE71.1	Carl Roth
Milk powder	42590.01	Serva
MOPS SDS Running Buffer (20x)	NP0001	Invitrogen
Myelin Removal Beads II, human, mouse, rat	130-096-733	Miltenyi Biotech
NH_3 (25 %)	6774	Carl Roth
N,N,N'N'-Tetramethylethylenediamide	T9281	Sigma
Neuropan Basal Medium	P04-00904	Pan Biotech

Neurobasal™-A Medium without phenolred	12349015	gibco
PBS	18912-014	gibco
Penicillin/Streptomycin	P06-07100	Pan Biotech
PFA	1.00496.5000	Sigma-Aldrich
Poly-L-lysine, succinylated	P3513	Sigma-Aldrich
Ponceau S Solution	P7170	Sigma-Aldrich
Propidium Iodide	CN74.1	Roth
Pierce Protease and Phosphatase Inhibitor Mini Tablets,EDTA-free	A32961	Thermo Fisher Scientific
Recombinant Rat beta-NGF Protein	556-NG	R&D Systems
Recombinant Rat GM-CSF Protein	518-GM	R&D Systems
RIPA lysis buffer	20-188	Merck Millipore
RNAse-free water	10977035	Thermo Fisher Scientific
RPMI medium	11835030	gibco
Saline (NaCl 0.9 %)	2350756	Braun
SDS pellets	CN30.2	Carl Roth
Sodium Chloride	2350756	Braun
Sodium Chloride	27788.297	VWR
Sodium pyruvate	11360070	gibco
TaqMan™ Universal Mastermix	4352042	Thermo Fisher Scientific
Tris base	sc-3715	Santa Cruz
Tris-HCl	H5123	Promega
Tris-HCl	15568025	Thermo Fisher Scientific
TritonX-100	10-188	Sigma-Aldrich
Trizma base	T1503	Sigma-Aldrich
Trizol	15596018	Life Technologies
Trypan Blue Stain (0.4 %)	15250-061	gibco
Trypsin-EDTA (0.05 %)	25300-054	gibco
Trypsin-EDTA (0.25 %)	25200056	gibco
Trypsin/Lys-C Mix	V5073	Promega
Tween-20	P1379	Sigma-Aldrich

2.1.4 Solutions

Table 4: Solutions.

Solution/Buffer	**Content**
FACS buffer	PBS 1x + 0.5 % BSA + 0.2 mM EDTA

Guanidinium chloride (GdmCl) lysis buffer	6 M GdmCl 200 mM HEPES pH 8.0 4% CHAPS 0.5 M NaCl
Laemmli Loading Buffer (5x) (50 ml)	25 ml glycerol 10 ml 1.5 M Tris-HCL 5 g SDS pellets 2.5 ml 1 % bromphenol blue 12.5 ml β-mercaptoethanol
Separating Gel 4 % (10 ml)	2.86 ml Bis-Tris 1.250 ml Acrylamid 50 µl APS 10 µl TEMED 5.830 ml ddH2O
Separating Gel 10 % (10 ml)	2.38 ml Bis-Tris 2.5 ml Acrylamid 25 µl APS 5 µl TEMED 5.090 ml ddH2O
Separating Gel 15 % (10 ml)	2.97 ml Bis-Tris 3.75 ml Acrylamid 25 µl APS 5 µl TEMED 3.25 ml ddH2O
Western Blot Transfer Buffer (1 L)	3.03 g Trizma base 14.4 g Glycin 100 ml Methanol in ddH2O
Western Blot Wash Buffer (TBS) (1 L)	2.4 g Tris Base 8.8 g NaCl in ddH2O pH 7.4
Western Blot Wash Buffer with Tween (TBS-T) (1 L)	2.4 g Tris Base 8.8 g NaCl 500 µl Tween-20 in ddH2O pH 7.4

2.1.5 Kits

Table 5: Kits.

Kits	**Catalog number**	**Company**
BCA Protein Assay Kits	23225	Thermo Scientific™
DCFDA/Cellular ROS Assay Kit	ab113861	abcam
ELISA Kit for IL-1β	KE20021	Proteintech
ELISA Kit for IL-18	KRC2341	Invitrogen
MTT Kit	ab211091	abcam

2.1.6 Antibodies

Table 6: Antibodies.

Antigen	React.	Isotype	Clonality	Conjugate	Catalog no.	Company
ASC	Rat	IgG Rabbit	polyclonal	unconjugated	NBP1-78977	Novus Biologicals
β-Actin	Rat	IgG Mouse	monoclonal	unconjugated	A1978	Sigma-Aldrich
BAX	Rat	IgG Rabbit	polyclonal	unconjugated	ab32503	abcam
BCL-2	Rat	IgG Rabbit	polyclonal	unconjugated	ab196495	abcam
Caspase-1	Rat	IgG Rabbit	polyclonal	unconjugated	AF5418	AffinityBiosciences
Caspase-9	Rat	IgG Rabbit	polyclonal	unconjugated	10380-1-AP	ProteinTech
CD11b/c	Rat	IgG2a Mouse	monoclonal	PE	201807	BioLegend
CD32	Rat	IgG1 Mouse	monoclonal	unconjugated	550270	BD Biosciences
CD45	Rat	IgG1 Mouse	monoclonal	BV711	740725	BD Biosciences
Cleaved Caspase-1	Rat	IgG Rabbit	monoclonal	unconjugated	89332	Cell Signaling
GFAP	Rat	IgG Mouse	monoclonal	unconjugated	3670	Cell Signaling
Goat Anti-Rabbit	Rat	IgG (H+L)	polyclonal	Horseradish Peroxidase	111-035-003	Jackson ImmunoResearch
Goat anti-mouse 594	Rat	goat	polyclonal	Alexa Fluor 594	11005	Invitrogen
Goat anti-rabbit 488	Rat	goat	polyclonal	Alexa Fluor 488	11008	Invitrogen
GSDMD	Rat	IgG Rabbit	monoclonal	unconjugated	ab219800	abcam
Iba-1	Rat	IgG Rabbit	polyclonal	unconjugated	019-19741	Wako
IL-1β	Rat	IgG Rabbit	polyclonal	unconjugated	ab9787	abcam
IL-18	Rat	IgG Rabbit	polyclonal	unconjugated	ab191860	abcam
IRDye® 680RD Goat Anti-Mouse	Rat	Mouse IgG	polyclonal	IRDye 680RD	926-68070	LI-COR
IRDye® 800CW Goat anti-Rabbit	Rat	Rabbit IgG	polyclonal	IRDye 800CW	926-32211	LI-COR
NeuN	Rat	IgG Mouse	monoclonal	unconjugated	MAB377	Millipore
NLRP3	Rat	IgG Rabbit	monoclonal	unconjugated	ab263899	abcam
Zombie	Rat		monoclonal	UV	77474	BioLegend

2.1.7 Primer

Table 7: Primer.

Target	Assay ID	Company
ASC	Rn00597229_g1	Thermo Fisher
β-Actin	Rn00667869_m1	Thermo Fisher
Caspase-1	Rn00562724m1	Thermo Fisher
GSDMD	Rn06429108_s1	Thermo Fisher
IL-1β	Rn00580432m1	Thermo Fisher
NLRP3	Rn04244620m1	Thermo Fisher

2.1.8 Software

Table 8: Software.

Software	Company
Catwalk XT 10.6	Noldus Information Technology, Wageningen, The Netherlands
EthoVision XT 17.5	Noldus Information Technology, Wageningen, The Netherlands
DIA-NN 2.2.0	APTILA
Fiji (ImageJ)	Open source scientific analysis program
FlowJo	BD
GraphPad Prism 10	GraphPad
R 4.5.1	R Foundation
RStudio 2025.05.1	Posit PBC
Tune v4.2.362.26	Thermo Fisher Scientific
Xcalibur v4.7.69.37	Thermo Fisher Scientific
Zen blue	Zeiss

2.2 Methods

2.2.1 In vivo model of hypoxia-ischemia

2.2.1.1 Animal research facility

All experiments were performed according to the ARRIVE guidelines and the North Rhine-Westphalia State Office for Consumer Protection and Nutrition (LAVE) guidelines, Germany. Wistar Rats were purchased from Janvier Labs (Le Genest-Saint-Isle, France) and kept in the animal facility of the Deutsches Zentrum für Neurodegenerative Erkrankungen (DZNE) Bonn, Germany with the conditions of a 12:12 light/dark cycle, an environmental temperature of 21 °C and food and water ad libitum.

2.2.1.2 Rice-Vannucci model

The *in vivo* model of HI was performed as described by Rice and Vannucci (Rice et al., 1981). Briefly, 7-day old (P7) Wistar rats were randomized across litter, sex and weight. A total of 249 animals were used for analysis (table 9; supplementary table 1 additionally shows gender distribution and death rate due to experiments).

Table 9: Overview of animal experiments. Listed details about experiments and animal number. FACS = fluorescence-activated cell sorting, HI/NT = hypoxia-ischemia/ normothermia, MACS = magnetic cell sorting, MRI = magnetic resonance imaging, NOR = novel object recognition, RT-PCR = real-time polymerase-chain reaction, WB = Western Blot. * Animals not sacrificed, but further kept for other analyses.

Experiment	Groups	Time points	Analysis	Animal amount
Hypoxia-ischemia/ Time point analysis	Sham vs HI/NT	4 h	WB	18
		12 h	WB	17
		24 h	WB	18
		36 h	WB	17
		48 h	WB	16
Hypoxia-ischemia/ Inhibitor treatment	Sham vs HI/Vehicle vs HI/Crid3	24 h	WB	37
		24 h	MACS/FACS/RT-PCR	30
		48 h	WB	67
		P 14	MRI	29*
		P 46-48	Catwalk	29*
		P 74-76	NOR	29*
		P 81	MRI	29*

The animals were subcutaneously (s.c.) injected with 0.05 mg/kg buprenorphine. After 30 min, anaesthesia was induced with 5 % isoflurane. The left common carotid artery was exposed and ligated. After ligation, the animals returned to their dams for 30 min before they underwent hypoxia in a hypoxic chamber set to 8 % O_2 for 90 min. The temperature was controlled with a cooling mat set to a rectal temperature (T_{rec}) of 36 °C of a probe animal which was injected with buprenorphine but did not undergo the ligation. The rectal probe (IT-21, Physitemp Instruments, Clifton, NJ, USA) was connected to a servo-controlled cooling machine which was connected to the cooling mat (water pad, Hico). After hypoxia, the animals underwent 5 h normothermia (NT) treatment with T_{rec} of 37 °C. The Sham animals were exposed to isoflurane for 5 min and served as control. After the experiment ended, the pups returned to their dams until they were sacrificed (figure 9).

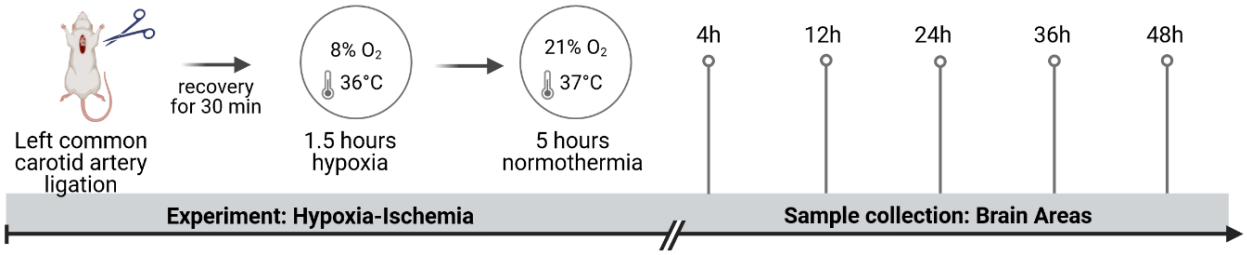

Figure 9: Experimental setup for Hypoxia-Ischemia treatment. P7 Wistar Rats underwent left common carotid artery ligation, recovered for 30 min and underwent 1.5 h hypoxia before 5 h of normothermia treatment. Animals were sacrificed at different time points after the experiment. Created with BioRender.com.

2.2.1.3 Treatment with inhibitor

To inhibit NLRP3 *in vivo*, the cytokine release inhibitory drug 3 (Crid3; 5.38120, Sigma-Aldrich) was used. Several experiments were performed to define the injection conditions affecting the activation of the NLRP3 pathway *in vivo*. After the first pilot experiments not showing an effective inhibition (supplementary table 2), a new experimental plan was designed to compare three different doses and two injection schemes (table 10). After testing different concentration of Crid3 and different injection time points, the setup of a two-time injection at 30 min before and 24 h after HI with 5 mg/kg Crid3 was established (figure 10). Crid3 and the vehicle solution (NaCl 0.9 %; 2350756, Braun) were injected intraperitoneally (i.p.) with a volume of 0.1 ml/10 g body weight.

Table 10: Overview of experiments with injections of NLRP3 inhibitor Crid3. Listed details about concentration and injection time points of Crid3.

experiments	**concentration**	**injection time points**		
		before HI	**after HI**	
1st experiment	5 mg/kg	30 min		24 h
	10 mg/kg	30 min		24 h
	20 mg/kg	30 min		24 h
2nd experiment	5 mg/kg		1h	24 h
	10 mg/kg		1h	24 h
	20 mg/kg		1h	24 h

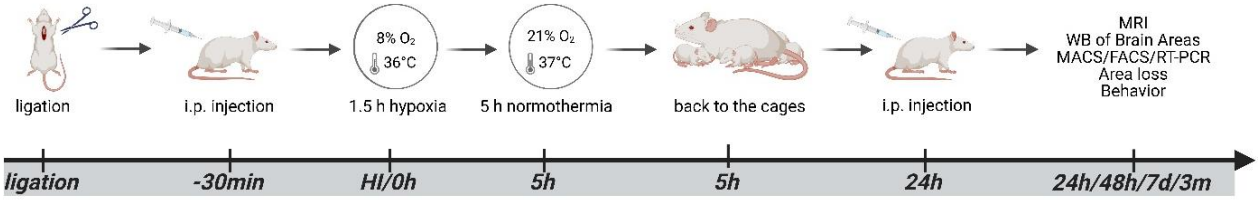

Figure 10: Experimental setup for treatment with NLRP3 inhibitor. P7 Wistar Rats underwent hypoxia-ischemia with a ligation of their left common carotid artery, followed by hypoxia for 1.5 h at 8 % oxygen. The NLRP3 inhibitor Crid3 was i.p. injected at 30 min before HI and 24 h after HI at a dose of 5 µg/kg. After HI, the animals underwent normothermia treatment for 5 h before being returned to their dams until sacrifice and further analysis at different time points. Created with BioRender.com.

2.2.1.4 Brain areas collection

Analyzing how different brain regions react to HI, the brain areas cortex, hippocampus and thalamus were collected at different time points after HI (figure 11). Animals were sacrificed at 4 h, 12 h, 24 h, 36 h and 48 h after the insult and the brains were removed. The cerebellum as well as the bulbus olfactorius were cut and excluded. The ipsilateral side was separated from the contralateral side and the areas were isolated from each other (figure 11). After transferring them into tubes, they were shock frozen in liquid nitrogen and transferred in -80 °C until further processing via Western Blot. All steps were performed on ice.

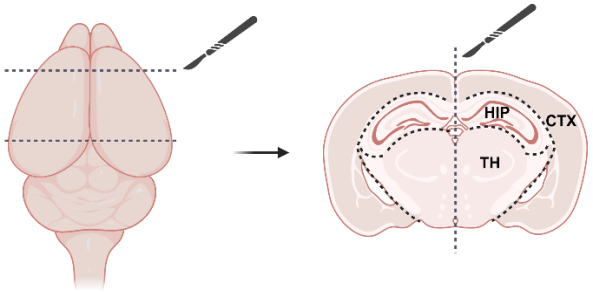

Figure 11: Brain areas collection. The brains were cut along the dashed lines outlined in the figure. Cortex (CTX), hippocampus (HIP) and thalamus (TH) were separated from each other. Created with BioRender.com

2.2.1.5 Magnetic resonance imaging

2.2.1.5.1 Acquisition of images

Magnetic resonance imaging (MRI) was performed to examine the level of brain damage of the different treatments. At postnatal days 14 and 81, the animals were anaesthetized with 5 % isoflurane and their brains were scanned with an 11.7 T horizontal small-bore magnet (Biospec 117/16; Bruker, Billerica, MA) and a rat brain receive only proton (1H) coil (Bruker Biospin). The acquisition of the images was conducted with a rapid acquisition relaxation enhancement T2-weighted sequence with an echo time of 25 ms, a repetition time of 2.9 s and an in-plane resolution of 0.156 × 0.156 mm^2. The images were taken from anterior to posterior in sagittal direction with a focus on Bregma region 0.2 to -7 mm.

2.2.1.5.2 Analysis of images

The edema area was measured on the Bregma region -0.88 mm with ImageJ and the percentage of area loss was calculated via the following formula.

$$\%\ (area\ loss) = \left(1 - \left(\frac{area\ ipsilateral - edema\ ipsilateral}{area\ contralateral}\right)\right) x\ 100$$

2.2.1.6 Behavioral experiments

2.2.1.6.1 Catwalk

The long-term effect of NLRP3 inhibition on motor function was assessed with Catwalk XT between postnatal days 46-48. During two days of training, the animals were habituated to walk through the catwalk setup in maximum 5 s. At the third day, the animals

performed three runs, with each a maximum of 5 s duration. The pass consisted of a glass plate, illuminated with red light. During the runs, the walking behavior was filmed with a camera from below. Using the Catwalk XT 10.6 software (Noldus Information Technology, Wageningen, The Netherlands), the average of the three runs was analyzed. The presented parameters to investigate the motor function of the animals were run duration (s), average speed (cm/s), step cycle (time (s) from when an initial paw contacts the glass to the next time the paw meets the glass) and paw stand (s).

2.2.1.6.2 Novel object recognition

The long-term effect of NLRP3 inhibition on cognitive function was assessed with novel object recognition (NOR) between postnatal days 74-76. Using 48 x 48 cm boxes with white walls and a black floor, the animals were recorded from above for 5 min when they were exposed to different objects. During two training days, the animals were habituated for 5 min in the box with two identical objects placed in two opposite corners. On the third day, the 5 min run was repeated, followed by a 1 h break. After the break, the animals were placed back into the box with one object being replaced by a new one and they were being recorded for 5 min. Analyzing the novel object recognition, the EthoVision XT 17.5 analysis system (Noldus Information Technology, Wageningen, The Netherlands) was used. The presented parameters to investigate the cognitive function of the animals were the frequency and the cumulative time the animal spent in the new object's area normalized to the areas of the new and old object together.

2.2.1.7 Transcardiac perfusion

To conservate the brain for further analyses, animals were sacrificed by transcardiac perfusion and fixation with 4 % paraformaldehyde (PFA). PFA was used to preserve tissue and cell structure. Briefly, the animals were sedated with 5 % chloral hydrate and their thorax was opened to expose the heart. The heart was flushed with PBS until the blood leaving the body was clear. Subsequently, the heart was flushed with 4 % PFA. The brains were removed and kept in PFA at least 24 h at 4 °C. They were cut into 3 mm coronal sections, processed (TP1020 Automatic Benchtop Tissue Processor, Semi-Enclosed, Leica) and embedded in paraffin (Paraffin pastilles, VWR).

2.2.2 In vitro model of hypoxia-ischemia

2.2.2.1 Cell culture of primary microglia

Wistar Rats (from Janvier Labs, Le Genest-Saint-Isle, France) were kept in the animal facility of the Deutsches Zentrum für Neurodegenerative Erkrankungen (DZNE) Bonn, Germany with conditions of a 12:12 light/dark cycle, a temperature of 21 °C and food and water ad libitum. Rat breeding and husbandry was approved by the veterinary office (Bonn, Germany) according to the German animal welfare act. The brains of neonatal rats (P1-P3) were used for microglia isolation. The meninges were removed from the brains in ice-cold 1x HBSS (PanBiotech) and the brain tissue was dissected with a scalpel. A 5 min incubation step in 0.25 % Trypsin/EDTA (gibco) at 37 °C for the enzymatic digestion was stopped by adding the double volume of DMEM medium (supplemented with 10 % FBS and 1 % Pen/Strep). After mechanically breaking up the cells, the cell suspension was dissociated through a 40 µm cell strainer. Following a centrifugation step at 300 g for 5 min, the cells were resuspended in DMEM (10 % FBS/1 % Pen/Strep) and plated on poly-L-lysine coated T75 culture flasks (two brains per flask). One to three days later (cultured at 37 °C, 5 % CO_2), the medium was changed to DMEM (10 % FBS/1 % Pen/Strep) supplemented with the recombinant rat GM-CSF protein (20 ng/ml, R&D Systems, 518-GM) as a growth factor. After approximately 5-7 days in culture, the microglia were shaken off the astrocyte layer and plated on coated 6- and 24-well plates with a density of 0.3 x 10^6 cells/ml in DMEM (10 % FBS/1 % Pen/Strep/20 ng/ml CSF). The subculture step was repeated two times per flask every two days. One day after plating the pure microglia (purity was tested by Iba-1/GFAP staining (see section 2.2.5 for protocol), threshold of 90 %), the cells were used for the oxygen-glucose deprivation (OGD) experiment (figure 12).

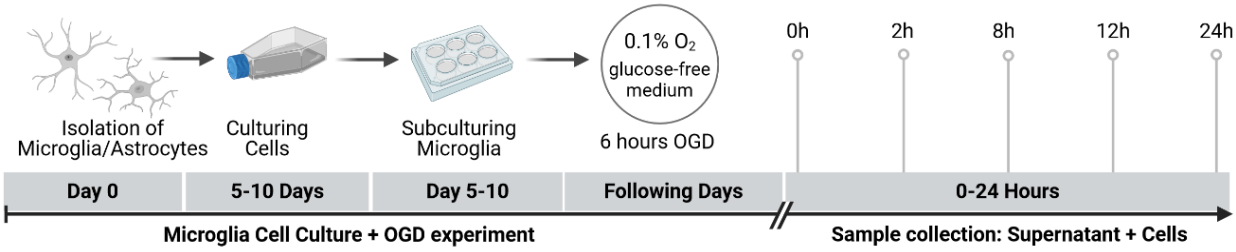

Figure 12: Setup for microglia cell culture and OGD experiment. Microglia were isolated and cocultured with astrocytes until they were shaken off and subcultured. The microglia underwent OGD with 0.1 % O_2 and glucose-free medium for 6 h. Cells and supernatant were collected at different time points thereafter. Created with BioRender.com

2.2.2.1.1 Oxygen-Glucose-Deprivation

The OGD experiment was performed with a hypoxic chamber (InvivoO_2 400, Baker Ruskinn). To establish the conditions for the OGD setup, different O_2 concentrations and durations of OGD were tested. Propidium iodide (PI) stainings were performed after OGD to analyze mortality of the cells. Cell were incubated with 1 µM PI for 10 min at 37 °C before washing them with PBS and imaging them in a fluorescence microscope (ZOE Fluorescent Cell Imager, Bio-Rad; cell death should not exceed 30 %).

Following, suitable OGD conditions for NLRP3 activation were described. Briefly, the cells undergoing OGD were washed with PBS and incubated with glucose-free DMEM medium (10 % FBS/1 % Pen/Strep/20 ng/ml CSF) for the duration of OGD at 0.1 % O_2 at 37 °C. The medium was adjusted to the hypoxic condition at least one hour before the experiment started. The control cells underwent a medium change and stayed for the same duration in normoxic conditions. After the 6 h of OGD, the medium was changed to culture medium and the cells were incubated at normoxic conditions for reoxygenation until sample collection. The positive control was performed by incubating the cells with 100 ng/ml LPS (L6529, Sigma-Aldrich) for 6 hours. Glucose-deprivation (GD) was conducted with cells in normoxic conditions and glucose-free medium. Oxygen-deprivation (OD) was conducted with cells in hypoxic conditions and culture medium containing glucose.

2.2.2.1.2 Treatment with inhibitor

For the treatment with the NLRP3 inhibitor, the cells were incubated with 1 µM Crid3 (5479, Tocris) 30 min before and during the OGD experiment.

2.2.2.1.3 Sample collection

After the OGD experiment, the cells and the supernatant were collected at different time points (0-24 h after OGD, see figure 12). The supernatant was kept at -20 °C until further use. The cells were collected differently depending on their further analysis.

2.2.2.1.3.1 Sample preparation for Western Blot

For analyzing the cells via Western Blot, the wells were washed in cold PBS and lysated with a buffer mix of 1x RIPA (Radioimmunoprecipitation Assay, Merck Millipore) and 1x

protease/phosphatase inhibitors (Thermo Fisher Scientific, diluted in ddH_2O). 100 µl buffer mix were added to the wells and after 5 min of incubation on ice, the cells were scraped of the plate and transferred to a tube. To mechanically break up the cells, a 25 G needle was used to carefully pipette them up and down. After an incubation for 15 min on ice, the lysates were centrifuged at 13,000 rpm for 15 min at 4 °C, transferred to a new tube and kept at -80 °C. The protein quantification for the lysates and further steps to analyze the samples via Western Blot were performed as described in 2.2.3 “Western Blot”.

2.2.2.1.3.2 Sample collection for RT-PCR

For RT-PCR analysis, the cells were collected as described in the section 2.2.4 “RT-PCR”.

2.2.2.1.4 Cell viability assay

To perform the cell viability assay, microglia were plated in two 24-well plates. One plate underwent the OGD experiment, the other was the control plate with normoxic conditions. The MTT (3-(4,5-dimethylthiazol-2-yl)-2,5-diphenyltetrazolium bromide) assay kit (abcam, ab211091) was used to determine the amount of viable cells in different treatment conditions. MTT is a reagent, which can be converted into formazan by viable cells. Formazan is measurable with an absorbance at 590 nm. The experiment was performed in duplicates and two wells per plate were included without plated cells for background subtraction. After the OGD experiment, the medium was changed to 200 µl serum- and phenolred-free DMEM medium and 20 µl MTT reagent was added. Subsequent to a 4 h incubation at 37 °C in the dark, 400 µl DMSO were added and carefully mixed with the medium to dissolve the forming crystals. The absorbance was measured in a plate reader (FLUOstar Omega, BMG Labtech) at 590 nm.

2.2.2.1.5 Proteomic analysis of microglia supernatant

2.2.2.1.5.1 Supernatant labelling

The protein synthesis of differently treated microglia was analyzed via liquid chromatography-mass spectrometry/mass spectrometry (LC-MS/MS). Microglia underwent either control conditions or an OGD experiment for 6 h with and without NLRP3 inhibition via Crid3 as already described. The culture of microglia was performed as described in 2.2.1 with the change in reducing the serum to 5 %. The serum reduction

was essential for the MS analysis to reduce background signals. Reducing the serum did not show any change in cell viability.

After the different treatments, cells were depleted of methionine for 30 min by washing the cells twice with PBS and changing the medium to DMEM without methionine (supplemented with 5 % FBS and 1 % Pen/Strep). Thereby, the protein synthesis was interrupted. To retrace the protein synthesis within a time span of 24 h, newly synthesized proteins were labelled with l-azidohomoalanine (AHA). Therefore, the medium was changed to methionine-free DMEM containing 2 mM AHA (Iris Biotech). AHA was an analog of methionine and was incorporated into newly synthesized proteins and thereby labelled the proteins synthesized in that specific time span. After 24 h labelling, the supernatant was collected. Cells were removed by a centrifugation step and the supernatant was frozen at -80 °C until further processing by AG Meissner (Institute of Innate Immunity, University Hospital Bonn, Biomedical Center (BMZ 2), 53127 Bonn, Germany).

2.2.2.1.5.2 Supernatant processing

Supernatant samples were thawed and filtered with the kit Amicon® Ultra Centrifugal Filter (UFC200324, Millipore), thereby reducing the volume from 1.5 ml to 100 µl. The samples were sonicated on ice with 1 ml of guanidinium chloride lysis buffer, supplemented with protease inhibitor cocktail before use (3 cycles, 5 s on/5 s off, 30 % amplitude). Subsequently, protein concentration was measured with BCA assay. All lysates were normalized to equal protein input for downstream copper-catalyzed azide-alkyne cycloaddition (CuAAC) enrichment.

2.2.2.1.5.3 Click-chemistry enrichment and peptide cleanup

Following the protocol of Bortecen and colleagues (Borteçen et al., 2023), epoxy-activated magnetic agarose beads (Cube Biotech) were functionalized. Subsequently, the click-chemistry enrichment was carried out using the functionalized beads and following the magnetic sorting, protein digestion was performed by adding 100 µl digestion buffer (100 mM Tris-HCl pH 8.0, supplemented with Trypsin/Lys-C Mix at 1 µl per reaction).

Peptides were acidified (1 % formic acid) and up to 40 µg peptides were loaded on two with CDS Empore™ SDB-RPS Extraction Disks (SPE-Disks-Bio-RPS-M-47.20)

assembled SDB-RPS StageTips by centrifugation. Peptide elution was carried out using 60 µl freshly prepared basic elution buffer (80 % acetonitrile, 5 % ammonium hydroxide solution; 25 % NH_3), followed by drying the samples and resuspending in 12 µl Buffer R (2 % acetonitrile, 0.1 % formic acid). 300 ng peptide (quantified with NanoDrop OneC (Thermo Scientific)) was subsequently injected for LC-MS/MS.

2.2.2.1.5.4 LC-MS/MS and quantification

Peptide analysis was performed on a Thermo Scientific Orbitrap Exploris 480 mass spectrometer coupled to a Thermo Scientific Vanquish Neo UHPLC operated in trap-and-elute mode. Xcalibur v4.7.69.37 and Tune v4.2.362.26 were used for instrument control. MS1 scans were acquired in the Orbitrap from m/z 300-1650 at 120,000 resolution with a maximum injection time of 60 ms and an AGC target of 300 %.

DIA raw data was analyzed with used DIA-NN (version 2.2.0). A spectral library was predicted from the FASTA database (Rattus norvegicus, UniProt SwissProt, downloaded May 2023). Parameters for mass accuracy were set to 30 ppm for MS2 and 15 ppm for MS1, with run-specific individual mass-accuracy calibration (`--individual-mass-acc`) and window inference (`--individual-windows`). DIA-NN was run with RT-dependent cross-run normalization, robust LC quantification, smart profiling library generation, and the single-pass neural network classifier. Analysis control was set to 1 % precursor- and protein-group FDR (false discovery rate) using DIA-NN's built-in q-value estimation.

2.2.2.1.5.5 Data processing

Processing of DIA-NN output files was carried out in R (v4.5.1) via RStudio (v2025.05.1) using MSstats (v4.16.1) and limma (v3.64.1). DIA-NN tables were converted using DIANNtoMSstatsFormat (`useUniquePeptide=TRUE`, `useZeroIntensity =FALSE`,`summary Method="TMP"`, `removeProtein_with1Feature=TRUE`, `equalFeatureVariance=TRUE`), followed by log2 transformation. Differential protein abundance was assessed with limma, fitting linear models with empirical Bayes moderation and correcting p-values using the Benjamini-Hochberg FDR (<0.05).

2.2.2.1.5. Analysis

Normalized values per condition were used for analysis. Genes were sorted after their log^2 fold change (log2FC) to analyze the effect of NLRP3 activation and inhibition. For the comparison OGD vs. CTR and OGD vs. OC, only genes with a minimum log2FC of 2 were included, and for the comparison OC vs. CTR, genes were included with a maximum log2FC of 1.5 to exclude genes, not specifically regulated by NLRP3. Subsequently, the included genes were analyzed with the STRING database (string-db.org).

2.2.2.2 Cell culture of neuronal cell line PC-12

The neuronal cell line PC-12 was received by AG Di Monte (DZNE, Bonn, Germany). The cells were plated on poly-L-lysine coated T75 culture flasks and cultured in RPMI medium (supplemented with 10 % HS, 5 % FBS and 1 % Pen/Strep). To obtain neuronal cells with developed dendrites, the cell line had to be differentiated. Therefore, the adherent cells were harvested from the flasks with 0.05 % trypsin and plated on 6-well plates for Western Blot analysis (150,000 cells/well) or on 24-well plates for cell viability assay (40,000/well). The RPMI growth medium was supplemented with non-essential amino acids and sodium pyruvate and with the Recombinant Rat beta-NGF Protein (100 ng/ml, R&D Systems, 556-NG) for differentiation (RPMI (10 % HS/5 % FBS/1 % Pen/Strep/1 % MEM-NEAA/1 % Pyruvate/100 ng/ml NGF)). After 2-3 days, the medium was changed to the differentiation medium without NGF. Two days later, the cells were used for an experiment.

2.2.2.2.1 Treating neurons with conditioned microglia supernatant

For testing the influence of NLRP3-activated and NLRP3-inhibited microglia on neuronal cells, neurons were incubated with supernatant of differently treated microglia for 24 h. Briefly, supernatant of microglia was collected at 24 h after an OGD experiment. The ratio 1:1 was used for microglia supernatant to culture medium of neurons (10 % HS/5 % FBS/1 % Pen/Strep/1 % MEM-NEAA/1 % Pyruvate). As control conditions, microglia medium (1:1 Ratio) and neuron culture medium were used. The treatments of microglia included the control group (CTR SN), control group with NLRP3 inhibitor Crid3 (CC SN), OGD group (OGD SN), OGD group with NLRP3 inhibitor Crid3 (OC SN) and the LPS group (LPS SN).

2.2.2.2.2 Sample collection and preparation for Western Blot

After the experiment, the cells were collected for Western Blot analysis. All steps were performed on ice to prevent protein degradation. Briefly, the cells were carefully washed with PBS and 200 µl buffer mix of 1 x RIPA buffer and 1 x protease/phosphatase inhibitors was added to each well. After 5 min incubation, the cells were scraped of the plates and transferred to 1.5 ml tubes. The cell suspension was broken up with a syringe and incubated on ice for 15 min. The lysates were obtained with a centrifugation step at 13,000 rpm for 15 min at 4 °C. They were transferred in a new tube and kept at -80 °C until further use. The next steps ("protein quantification" and "protein separation, transfer and detection") are described in the section 2.2.3 "Western Blot".

2.2.2.2.3 Cell viability assay

The cell viability assay was performed as described in "Cell viability assay" in the microglia section 2.2.2.1.4. Briefly, after undergoing the treatment with conditioned microglia supernatant, the neuronal cells were stained with 20 µl MTT reagent in 200 µl serum-free RPMI (1 % Pen/Strep/1 % MEM-NEAA/1 % Pyruvate) per well. Duplicates were carried out and wells without cells were included to perform background subtraction. The incubation lasted for 4 h at 37 °C in the dark, followed by adding 400 µl DMSO to each well. The medium was carefully mixed with the DMSO to dissolve crystals and directly thereafter, the plate was read out in a plate reader (FLUOstar Omega, BMG Labtech) with an absorbance at 590 nm.

2.2.3 Western Blot

2.2.3.1 Sample preparation and lysis

To lysate the brain tissue, a buffer mix of 1 x RIPA (Radioimmunoprecipitation Assay, Merck Millipore) and 1 x protease/phosphatase inhibitors (Thermo Fisher Scientific, diluted in ddH_2O) was used. 5 µl buffer per 1 mg of brain tissue were added, carefully pipetted up and down and incubated on ice for 15 min. Once again, the cell lysate was carefully pipetted up and down through a smaller pipette tip to dissociate the tissue and incubated on ice for 10 min followed by a centrifugation step at 13,000 rpm for 15 min at 4 °C. Receiving the lysate, the supernatant was kept at -80 °C.

2.2.3.2 Protein quantification

For measuring the protein amount of the samples, a BCA Assay (bicinchoninic acid assay, Pierce™ BCA Protein Assay Kits, Thermo Scientific™) was performed. The alkaline medium of the Kit supports the reduction of Cu^{2+} to Cu^{1+} and thereby offers the opportunity for BCA reacting with Cu^{1+} to produce a colored reaction product, which is quantifiable at an absorbance of 562 nm.

The lysates were diluted in ddH_2O depending on the expected amount of protein (1:5 for cells, 1:100 for brain tissue). The diluted lysates, double-distilled water for the background subtraction and the standard series of the kit were pipetted in a 96-well plate in duplicates with a volume of 15 µl each. 150 µl of the BCA reagents were added per well and the plate was incubated at 37 °C for 30 min. The absorbance was measured in a plate reader at 562 nm (FLUOstar Omega, BMG Labtech).

2.2.3.3 Protein separation, transfer and detection

According to the protein amount, a mastermix containing the end concentration of 50 µg protein of brain tissue samples or 20 µg for cell culture samples, 1x loading/Laemmli buffer and ddH_2O was prepared. After a 10 min incubation at 95 °C for denaturation, the samples were loaded on a SDS-PAGE (Sodium Dodecyl Sulfate-PolyAcrylamid Gel Electrophoresis, either 10 % + 4 % or 15 % + 4 %). Additional, a ladder (Chameleon® Duo Pre-stained Protein Ladder, LI-COR) was applied for the recognition of the protein size. The mini-cell electrophoresis system (XCell SureLock™ Mini-Cell, Invitrogen) was connected to 90 V for 10 min, followed by 110 V for approximately 50 min (Power Source 300V, VWR). The system was filled with either 1 x MES (2-Morpholinoethanesulphonic acid, Invitrogen) or 1 x MOPS (3-(N-morpholino)propanesulfonic acid, 4-Morpholino Propanesulfonic Acid, Invitrogen) buffer to provide the optimal separation of the analyzed proteins. The gel containing the separated proteins and the ladder was transferred to a polyvinylidene difluoride membrane (Immobilon®-FL, Merck) in transfer buffer for 90 min at 30 V (XCell SureLock™ Mini-Cell, Invitrogen and Power Source 300V, VWR) or 110 V (Mini-PROTEAN Tetra Vertical Electrophoresis Cell and PowerPac™ Basic Power Supply, Bio-Rad) depending on the system used. After the transfer, the protein bands were visualized by incubating the membrane in Ponceau solution (Sigma Aldrich) to control the transfer. Following a washing step in Tris-buffered saline with Tween20 (TBS-T), the

membrane was blocked in 5 % milk (Serva, diluted in TBS-T) for 1 h at room temperature (RT). The primary antibody (see table 11, diluted in 1 % milk) was incubated over night at 4 °C. The membrane was washed three times with TBS-T, followed by the incubation with the secondary antibody (see table 11, diluted in 1 % milk). The detection was performed with either fluorescence or enhanced chemiluminescence (ECL). The secondary antibodies were incubated for 1 h at RT. After washing the membrane again, the proteins were imaged with an Odyssey infrared imaging system (LI-COR Biosciences) or with the iBright 1500 (Invitrogen). The membranes stained with the ECL secondary antibody had to be supplemented with SuperSignal West Pico Plus Chemiluminescent Substrate (Thermo Fisher Scientific) to detect the protein bands. The analysis was performed with ImageJ and normalization was set to β-actin as a loading control.

Table 11: List of antibodies used for Western Blot.

Primary antibody	**Company**	**Catalogue number**	**Dilution**
ASC	Novus Biologicals	NBP1-78977	1:250
β-Actin	Sigma-Aldrich	A1978	1:3000
BAX	abcam	ab32503	1:1000
BCL-2	abcam	ab196495	1:1000
Caspase-1	Affinity Biosciences	AF5418	1:1000
Caspase-9	ProteinTech	10380-1-AP	1:500
Cleaved Caspase-1	Cell Signaling	89332	1:250
GSDMD	abcam	ab219800	1:500
IL-1β	abcam	ab9787	1:200
IL-18	abcam	ab191860	1:250
NLRP3	abcam	ab263899	1:500
Secondary antibody	**Company**	**Catalogue number**	**Dilution**
Goat Anti-Rabbit	Jackson ImmunoResearch	111-035-003	1:10,000
IRDye 680RD Goat Anti-Mouse	LI-COR	926-68070	1:3000
IRDye 800CW Goat anti-Rabbit	LI-COR	926-32211	1:5000

2.2.4 RT-PCR

2.2.4.1 Sample preparation and RNA

For analyzing microglia via RT-PCR, the cells were collected after the OGD experiment. Briefly, the cells were washed in cold PBS and then scraped in a volume of 1 ml Trizol (Life Technologies) and transferred to 1.5 ml tubes. After a 5 min incubation step on ice, the cell suspension was centrifuged at 8000 rpm for 5 min at 4 °C. The supernatant was

transferred to a new tube and supplemented with 200 µl chloroform (Merck Millipore). The mixture was thoroughly vortexed, followed by a centrifugation step at 13,000 rpm for 15 min at 4 °C. Three phases were visible afterwards, the upper aqueous phase which contained the RNA, the interphase with the DNA and the organic phase which contained trizol and other debris. The upper aqueous phase was complemented with the double volume of 100 % ethanol and kept at -20 °C over night for precipitation.

The precipitate was received by a centrifugation at 13,000 rpm for 20 min at 4 °C. Subsequently, the RNA of the microglia was purified by washing the precipitate with 1 ml 70 % ethanol at 13,000 rpm for 5 min at 4 °C. After the last wash, the resolving pellet was dried (vacuumizer, 40 min, RT). Adding 25 µl RNAse-free water to the dry pellet and incubating for 30 min at 4 °C produced the RNA for further analysis. Consequently, the RNA concentration and purity was measured with a nanodrop (DeNovix).

2.2.4.2 cDNA synthesis

To synthetize the cDNA from the RNA, the following mastermix was used: 2 µl RT buffer (10x), 0.8 µl dNTP mix (25x), 2 µl RT Random Primers (10x), 1 µl Reverse Transcriptase, 4.2 µl RNAse-free water (all chemicals provided from Thermo Fisher Scientific) with a total volume of 10 µl. 10 µl of RNA and 10 µl of mastermix were added to PCR strip tubes. For the cDNA synthesis the samples underwent the following cycler program (T3000, Biometra).

Step 1: 25 °C	10 min
Step 2: 37 °C	120 min
Step 3: 85 °C	5 min
Step 4: 4 °C	hold

2.2.4.3 RT-PCR

The RT-PCR was performed with the QuantStudio™ 3 Real-Time PCR System (Thermo Fisher Scientific). 2 µl of 1:2 diluted cDNA was added to the 96-well reaction plate (Thermo Fisher Scientific). For the negative control RNAse-free water was used. 8 µl of the primer mastermix (5 µl master mix (Thermo Fisher Scientific), 0.5 µl primer (see table 12) and

2.5 µl RNAse-free water) was added. Technical duplicates were performed. The following cycler program was used to achieve the transcript results.

Step 1: 95 °C 20 s
Step 2: 95 °C 1 s
Step 3: 60 °C 20 s
Plate read
Go to step 2: 40x repeat

Table 12: Overview of primers used for RT-PCR.

Primer target	Assay ID	Company
ASC	Rn00597229_g1	Thermo Fisher
β-Actin	Rn00667869_m1	Thermo Fisher
Caspase-1	Rn00562724m1	Thermo Fisher
GSDMD	Rn06429108_s1	Thermo Fisher
IL-1β	Rn00580432m1	Thermo Fisher
NLRP3	Rn04244620m1	Thermo Fisher

2.2.4.4 Analysis

The raw data of the cycle describing the exponential phase of amplification was normalized to actin and to the control values to receive the relative fold gene expression of the protein ($2^{-\Delta\Delta Ct}$).

2.2.5 Immunofluorescence staining

To stain primary microglia cells, they were plated on glass coverslips in 24-well plates. At different time points after the experiment, the cells were washed with PBS before they were fixated by incubating them for 10 min in cold methanol 100 % at 4 °C. After the fixation, the coverslips were stored at -20 °C until further processing.
Coverslips were blocked with 20 % goat serum (Thermo Fisher Scientific, diluted in PBS) for 30 min at RT. The primary antibody (table 13, diluted in 0.7 % Carrageen solution) was incubated overnight at 4 °C followed by the incubation with the secondary antibody for 1 h at RT in the dark (table 13). DAPI (4,6-diamidino-2-phenylindole) was counterstained via Fluoromount G™ Mounting Medium (Invitrogen). The coverslips were scanned with a

confocal microscope (LSM800, Zeiss) and analyzed with ZEN Blue 3.1 (Carl Zeiss Microscopy GmbH) and ImageJ (Fiji).

Table 13: List of antibodies used for immunohistochemistry.

Primary antibody	**Company**	**Catalogue number**	**Dilution**
GFAP	Cell Signaling	3670	1:50
Iba-1	Wako	019-19741	1:400
Secondary antibody	**Company**	**Catalogue number**	**Dilution**
Goat anti-mouse 594	Invitrogen	11005	1:250
Goat anti-rabbit 488	Invitrogen	11008	1:500

2.2.6 ELISA

The collected supernatant of microglia was analyzed via enzyme-linked immunosorbent assay (ELISA) to detect IL-1β. The procedure was carried out as described in the protocol of the kit. Previous to the ELISA assay, an enrichment of the protein in the supernatant was conducted to achieve a detectable amount of protein.

2.2.6.1 Enrichment of protein in supernatant samples

The kit Amicon® Ultra Centrifugal Filter (UFC201024, Millipore) was used to increase the protein concentration in the supernatant samples. Briefly, 1 ml of sample was added to the centrifugal filter device and centrifuged for 15-30 min at 2000 g at 4 °C. The centrifugation time was adjusted to achieve a sample volume of 200-250 µl. The flow-through was discarded and the resolving sample of 200-250 µl was centrifuged out of the device to a collection tube (2000 g, 5 min, 4 °C). The collected sample was directly used for ELISA assays.

2.2.6.2 IL-1β

The ELISA IL-1β kit was purchased from Proteintech (KE20021). 100 µl of each standard and sample and the blank were added in duplicates to the wells of the 96-well plate and incubated over night at 4 °C on an orbital shaker. The next day, the content of the wells was discarded and the wells were washed four times with 1x wash solution. The wells were incubated with 100 µl of 1x biotinylated antibody for 1 h at 37 °C. All incubation steps

were performed on an orbital shaker. After washing the wells, 100 µl of Streptavidin solution was added and incubated for 40 min at 37 °C. The washing steps were repeated, followed by adding 100 µl of TMB (3,3',5,5'-tetramethylbenzidine) One-Step Substrate Reagent into each well and an incubation for 20 min in the dark. 100 µl of stop solution was supplemented and directly thereafter, the absorbance was measured at 450 nm. The blank values were used for background subtraction.

2.2.7 Microglia isolation with beads

To perform a microglia isolation with magnetic-activated cell sorting (MACS), the brains of the animals to analyze were removed and dissected into brain areas. All steps were performed on ice and centrifugation steps were conducted at 4 °C. The ipsilateral cortex was collected in HBSS (supplemented with calcium/magnesium). It was homogenized by carefully pipetting the tissue up and down a few times and by taking through a 40 µm cell strainer. The suspension was centrifuged at 300 g for 10 min and the cell pellet was resuspended in myelin removal beads (Myelin Removal Beads II, human, mouse, rat, 130-096-733, Miltenyi Biotech), diluted in FACS buffer (D-PBS 1x + 0.5 % BSA + 0.2 mM EDTA; 20 µl beads in 180 µl buffer per sample). After an incubation step of 15 min, 10 ml FACS buffer were added and the mix was centrifuged at 300 g for 10 min. For the magnetic sorting, the MACS MultiStand (MACS® MultiStand, 130-042-303, Miltenyi Biotech) and the QuadroMACS separator (QuadroMACS™ Separator, 130-091-051, Miltenyi Biotech) were used for the LS columns (LS columns, 130-042-401, Miltenyi Biotech). The LS columns were washed with FACS buffer before usage. The cell pellet was resuspended in 1.5 ml FACS buffer, passed through the columns and collected in a tube. After washing the columns twice with 1 ml each, the cell suspension was centrifuged at 300 g for 10 min. The cell pellet was resuspended in CD11b/c beads (CD11b/c (Microglia) MicroBeads, rat, 130-105-634, Miltenyi Biotech), diluted in FACS buffer (20 µl beads in 500 µl buffer). After an incubation step of 15 min, 5 ml FACS buffer were added and the mix was centrifuged at 300 g for 5 min. The LS columns and the quadro MACS separator were replaced by MS columns (MS columns, 130-042-401, Miltenyi Biotech) and OctoMACS separator (OctoMACS™ Separator, 130-042-109, Miltenyi Biotech) for the next separation step. Before usage, the columns were washed with FACS buffer. After resuspending the cell pellet in 500 µl FACS buffer, the mix was applied to the columns.

The columns were washed twice with 1 ml FACS buffer and the flow through was discarded. To collect the sorted cells, the columns were flushed with the plunger with 1 ml FACS buffer into a collection tube.

2.2.7.1 Analysis via RT-PCR

To isolate the RNA of the sorted microglia, the cell suspension was centrifuged at 8000 rpm for 5 min at 4 °C and the cell pellet was resuspended in 1 ml of trizol. The isolation of RNA and the performance of RT-PCR was conducted with the same protocol as described in section 2.2.4.

2.2.7.2 Analysis via fluorescence-activated cell sorting (FACS)

The FACS analysis was used to provide confirmation about the purity of the isolated microglia. The sorted cells were counted and 1.9 x 10^4 cells were pipetted into a 96-well plate. After a centrifugation step at 1000 rpm for 5 min, the supernatant was discarded and 150 µl of a mixture of blocking and antibody solution (see table 14, diluted in PBS) were added to the wells. The mix was incubated for 30 min. All steps were performed on ice and centrifugation steps were conducted at 1000 rpm for 5 min. After incubation, the cell suspension was centrifuged and the cells were washed by adding 200 µl PBS, followed by a centrifugation. The washed cell pellet was resuspended in 200 µl PBS and transferred to a FACS tube (Sarstedt) to perform measurements with the FACS machine (BD FACS Symphony™ A5). The samples were gated for Ultraviolet (UV), Brilliant Violet 711 (BV711) and Phycoerythrin (PE) to detect stained cells for Zombie (dead cells), CD45 (leucocyte common antigen, microglia marker) and CD11b/c (microglia marker). The software FlowJo (BD) was used for analysis.

Table 14: List of antibodies used for FACS.

Antibody	**Company**	**Cat. No.**	**Dilution**
PE anti-rat CD11b/c Antibody	BioLegend	201807	1:100
BD Pharmingen™ Purified Mouse Anti-Rat CD32	BD Biosciences	550270	1:100
BD OptiBuild™ BV711 Mouse Anti-Rat CD45	BD Biosciences	740725	1:100
Zombie UV™ Dye	BioLegend	77474	1:1000

2.2.8 Statistical analysis

The data plots and the statistical analysis were performed with GraphPad Prism 10 (GraphPad Software, USA). The Kruskal-Wallis-test was used for multiple comparisons and the Mann-Whitney-U-test was used to pairwise compare the groups with each other. Asterisks indicate the statistical significance, which was set to $p \leq 0.05$ (* $p \leq 0.05$; ** $p \leq 0.01$; *** $p \leq 0.001$; **** $p \leq 0.0001$). Data are presented as median with interquartile range. A minimum of 3 biological replicates (*in vivo* experiments representing animals, *in vitro* experiments representing different cultures of cells) and 3 technical replicates were used for the experiments (no significant variability between technical replicates).

3. Results

3.1 NLRP3 pathway activation in vivo

3.1.1 NLRP3 pathway proteins were time-dependently regulated following neonatal HIE

To analyze the activation and relevance of the NLRP3 inflammasome in the neonatal animal model of hypoxic-ischemic encephalopathy, protein levels of different pathway components were analyzed: NLRP3, caspase-1, ASC, IL-1β, IL-18 and GSDMD. At five different time points after HI, the brain regions cortex and hippocampus of animals which underwent HI/NT treatment were compared to Sham animals. In previous experiments, those brain regions were shown to be the most affected by HI. The time points were chosen to cover the early inflammatory response after the HI insult.

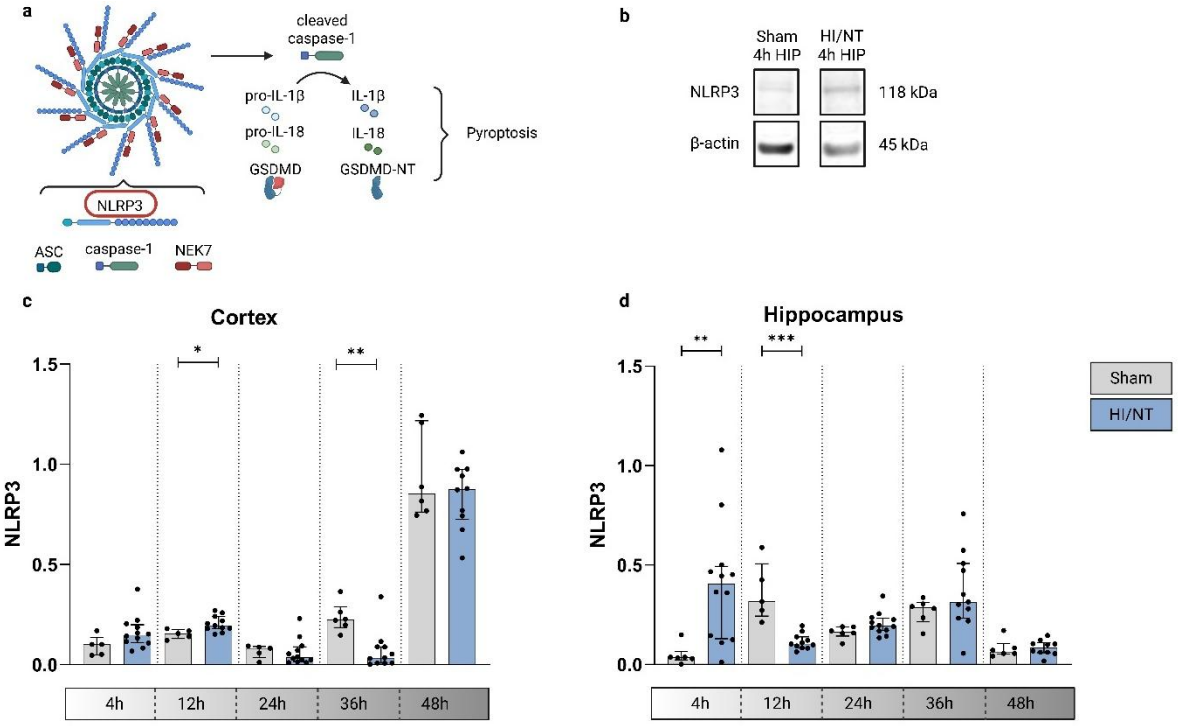

Figure 13: Protein expression of NLRP3 in neonatal HIE. P7 Wistar rats underwent left common carotid artery ligation and subsequently hypoxia treatment for 90 min. Animals were sacrificed and brain areas were taken at five different time point after hypoxia (x-axis). **a** Overview of the NLRP3 pathway with highlighted protein NLRP3. Created with BioRender.com. **b** Exemplary Western Blot bands of NLRP3 and β-actin comparing the two treatment groups Sham and HI/NT. **c-d** Western Blot analysis of control animals (Sham, grey bars) vs hypoxia-ischemia/normothermia treated animals (HI/NT, blue bars) of cortex (**c**) and hippocampus (**d**) in the ipsilateral side of the brain. Bars display the median and the interquartile range. N (Sham) = 5-6; N (HI/NT) = 10-12. Statistics: Mann-Whitney-U-test (* $p \leq 0.05$; ** $p \leq 0.01$; *** $p \leq 0.001$).

Visualized in figure 13, the NLRP3 protein was significantly upregulated at early time points after HI. Cortically, there was a significant increase compared to Sham control at 12 h after HI and a significant decrease at 36 h. In the hippocampus, NLRP3 increased significantly at 4 h after HI and at the next time point analyzed, the level decreased again significantly, followed by time points showing no difference between HI/NT and Sham (figure 13).

The protein levels of cleaved caspase-1 decreased in both, hippocampus and cortex, at 12 h after HI. Thereafter, there was an elevation in protein expression, reaching a significant difference between HI/NT and Sham at 36 h in hippocampus (figure 14).
When calculating the ratio of cleaved caspase-1 to its uncleaved inactive form, the trend of a late increase in active caspase-1 was verified. In cortex, upon 36 h after HI, cleaved caspase-1 increased relative to full caspase-1 with a significant difference to Sham at 48 h, demonstrating the dominating active form of the protein. The hippocampus already showed the increasing trend upon 24 h with significant elevations at 24 and 36 h after HI. Especially in the cortex, the switch from an inactive form to the cleavage and activation of caspase-1 was discovered by comparing the different time points after HI. Early time points showed less cleaved caspase-1 in HI/NT compared to Sham, whereas this trend changed with time (figure 14).

The protein ASC can be present as monomer, dimer or oligomer. When activated, it forms oligomers and builds ASC specks (Dick et al., 2016; Guo et al., 2021). Studying the expression of ASC, the focus laid on one monomeric and one oligomeric form of the protein to study its activation state (figure 15).
The expression of ASC differed strongly during the five time points analyzed. This dynamic pattern started with an early significant upregulation of monomeric ASC in the hippocampus at 4 h after HI. At 12 h, ASC oligomers and monomers were elevated in HI/NT compared to Sham. Following a decrease in ASC expression at 24 h, the late time points presented an upregulation of monomers and oligomers compared to Sham in the cortex and hippocampus, except the ASC monomer at 48 h in the hippocampus and at 36 h in the cortex. Comparing monomer and oligomer expression, there was an early increase in monomers and a late increase in oligomers, representing the switch from an inactive to an active form of the protein (figure 15).

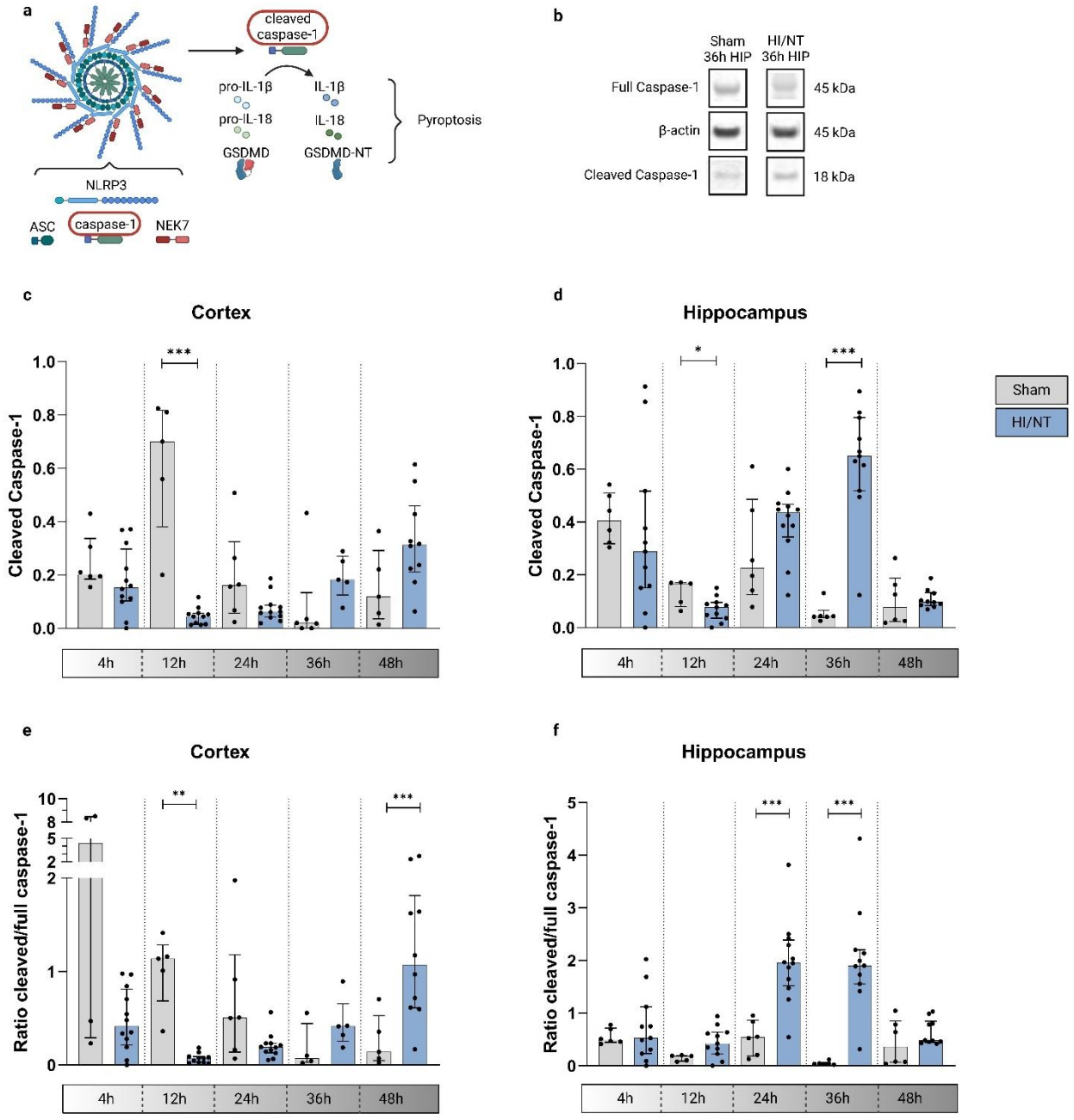

Figure 14: Protein expression of caspase-1 in neonatal HIE. P7 Wistar rats underwent left common carotid artery ligation and subsequently hypoxia treatment for 90 min. Animals were sacrificed and brain areas were taken at five different time point after hypoxia (x-axis). **a** Overview of the NLRP3 pathway with highlighted proteins caspase-1 and cleaved caspase-1. Created with BioRender.com. **b** Exemplary Western Blot bands of caspase-1, cleaved caspase-1 and β-actin comparing the two treatment groups Sham and HI/NT. **c-f** Western Blot analysis of control animals (Sham, grey bars) vs hypoxia-ischemia/normothermia treated animals (HI/NT, blue bars) of cortex (**c**, **e**) and hippocampus (**d**, **f**) in the ipsilateral side of the brain. Bars display the median and the interquartile range. N (Sham) = 5-6; N (HI/NT) = 10-12. Statistics: Mann-Whitney-U-test (* $p \leq 0.05$; ** $p \leq 0.01$; *** $p \leq 0.001$).

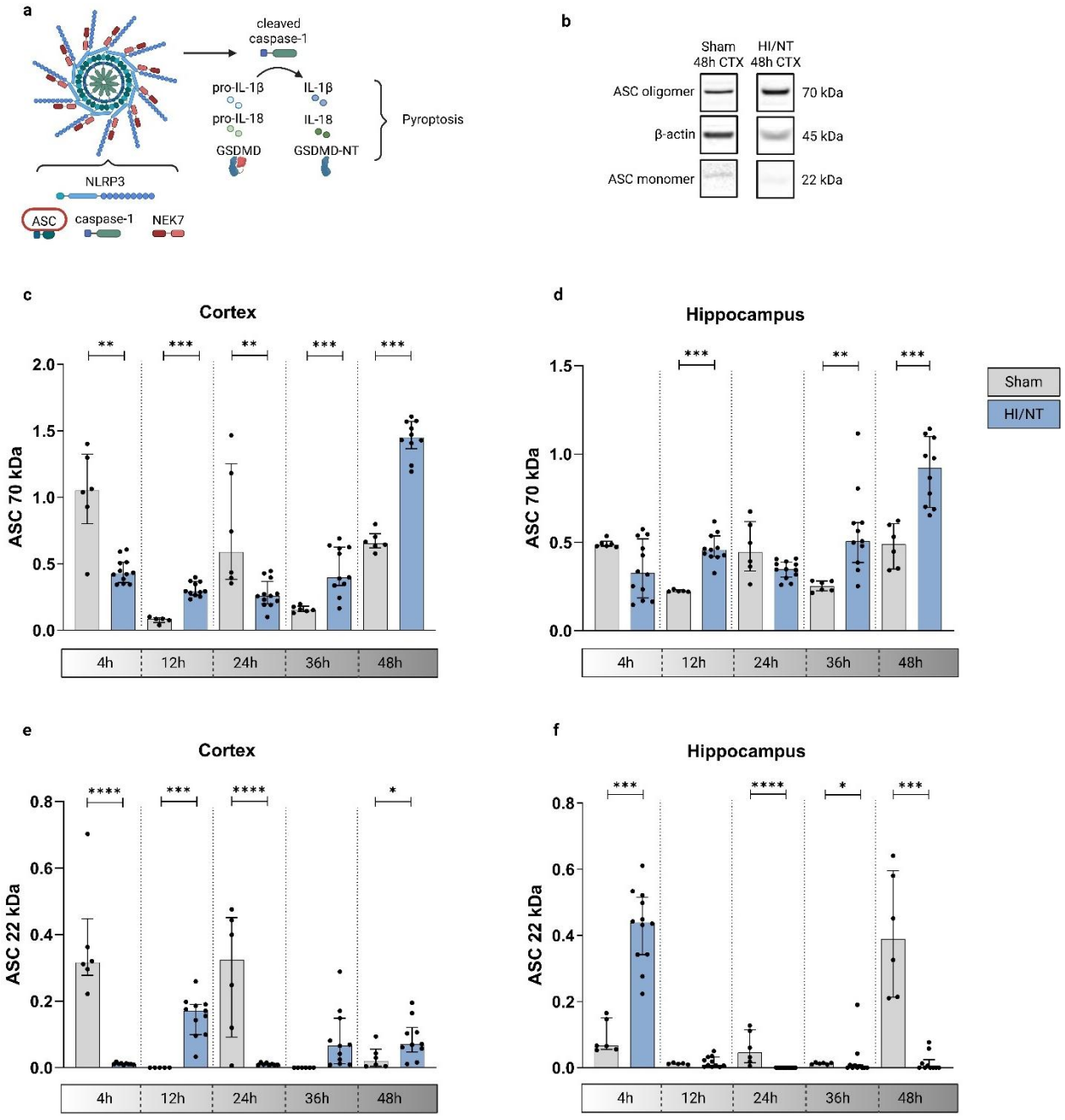

Figure 15: Protein expression of ASC in neonatal HIE. P7 Wistar rats underwent left common carotid artery ligation and subsequently hypoxia treatment for 90 min. Animals were sacrificed and brain areas were taken at five different time point after hypoxia (x-axis). **a** Overview of the NLRP3 pathway with highlighted ASC protein. Created with BioRender.com. **b** Exemplary Western Blot bands of ASC oligomer (70 kDa), ASC monomer (22 kDa) and β-actin comparing the two treatment groups Sham and HI/NT. **c-f** Western Blot analysis of control animals (Sham, grey bars) vs hypoxia-ischemia/ normothermia treated animals (HI/NT, blue bars) of cortex (**c**, **e**) and hippocampus (**d**, **f**) in the ipsilateral side of the brain. Bars display the median and the interquartile range. N (Sham) = 5-6; N (HI/NT) = 10-12. Statistics: Mann-Whitney-U-test (* $p \leq 0.05$; ** $p \leq 0.01$; *** $p \leq 0.001$; **** $p \leq 0.0001$).

To study the activation of the NLRP3 inflammasome pathway, the expression of the downstream targets IL-1β and IL-18 was investigated. As the cleavage of those interleukins represented the last step of the pathway, the analysis focused on the cleaved proteins (figure 16). In the cortex, cleaved IL-1β was significantly decreased at 36 h after HI and significantly upregulated at 48 h. Cleaved IL-18 did not show any significant changes in expression between HI/NT and Sham, although an increase was observed at 12 h. In the hippocampus, cleaved IL-1β only showed decreasing trends when comparing the animal model of HIE to the control. However, cleaved IL-18 did present a significant increase in HI/NT from 12 h to 36 h after HI with the highest elevation at 24 h (figure 16). Taken together, an increase was observed for the interleukin IL-1β in the cortex at 48 h after HI. Whereas in the hippocampus, the highest increase was shown by IL-18 at 24 h after HI.

Another downstream target of the pathway is GSDMD. Cleaved by caspase-1, GSDMD is separated in the C- and N-terminal parts with the N-terminal part being the active one leading to pyroptosis (Liu et al., 2016). The analysis of full GSDMD demonstrated a fluctuating expression pattern in both brain areas (figure 17c-d). The N-terminal part of GSDMD could only be detected at late time points in HI/NT. Representing the pyroptosis-inducing protein, GSDMD-NT was significantly elevated at 24 and 36 h after HI in cortex and at 36 and 48 h after HI in hippocampus (figure 17e-f).

Summarizing the data of the NLRP3 pathway components, a time-dependent change in expression of up- and downstream pathway proteins was uncovered. Upstream proteins (NLRP3, ASC monomer, caspase-1, GSDMD) were upregulated at earlier time points after HI and downstream pathway proteins (cleaved caspase-1, ASC oligomer, cleaved IL-1β, cleaved IL-18, GSDMD-NT) were elevated at later time points.

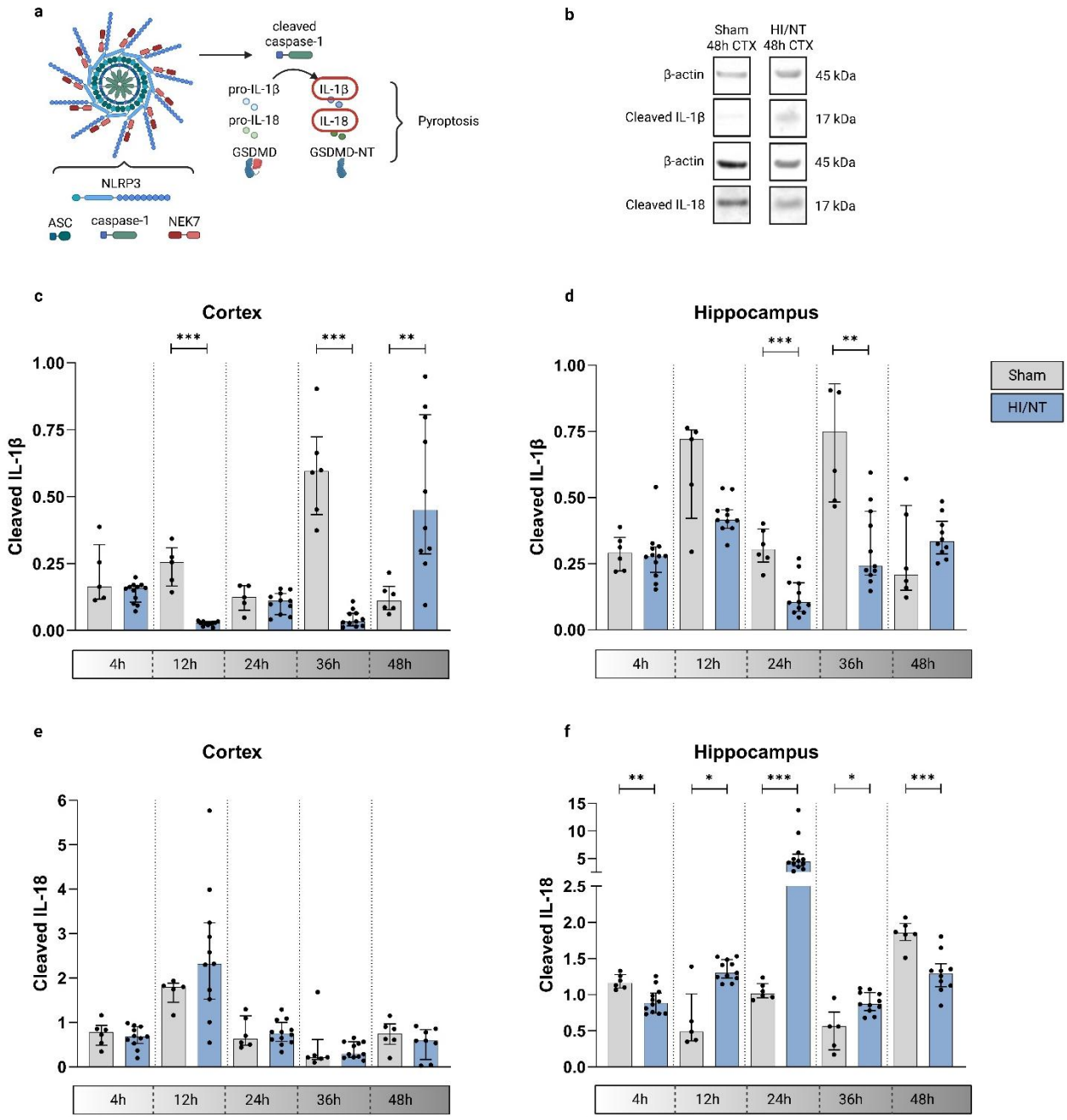

Figure 16: Protein expression of cleaved IL-1β and IL-18 in neonatal HIE. P7 Wistar rats underwent left common carotid artery ligation and subsequently hypoxia treatment for 90 min. Animals were sacrificed and brain areas were taken at five different time point after hypoxia (x-axis). **a** Overview of the NLRP3 pathway with highlighted proteins cleaved IL-1β and IL-18. Created with BioRender.com. **b** Exemplary Western Blot bands of cleaved IL-1β, cleaved IL-18 and β-actin comparing the two treatment groups Sham and HI/NT. **c-f** Western Blot analysis of control animals (Sham, grey bars) vs hypoxia-ischemia/ normothermia treated animals (HI/NT, blue bars) of cortex (**c**, **e**) and hippocampus (**d**, **f**) in the ipsilateral side of the brain. Bars display the median and the interquartile range. N (Sham) = 5-6; N (HI/NT) = 10-12. Statistics: Mann-Whitney-U-test (*p ≤ 0.05; ** p ≤ 0.01; *** p ≤ 0.001).

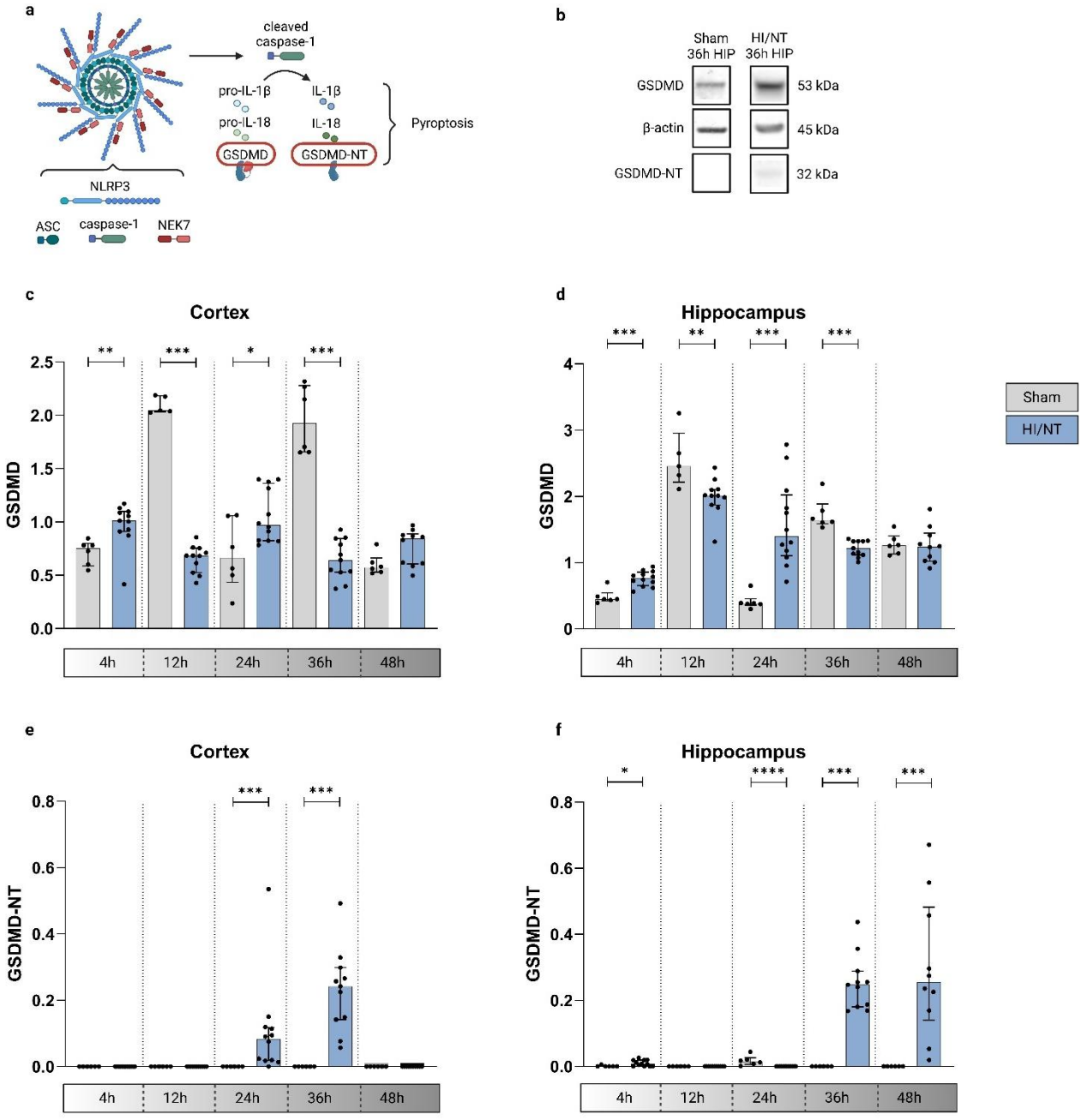

Figure 17: Protein expression of GSDMD in neonatal HIE. P7 Wistar rats underwent left common carotid artery ligation and subsequently hypoxia treatment for 90 min. Animals were sacrificed and brain areas were taken at five different time point after hypoxia (x-axis). **a** Overview of the NLRP3 pathway with highlighted GSDMD and GSDMD-NT. Created with BioRender.com. **b** Exemplary Western Blot bands of GSDMD, GSDMD-NT and β-actin comparing the two treatment groups Sham and HI/NT. **c**-**f** Western Blot analysis of control animals (Sham, grey bars) vs hypoxia-ischemia/normothermia treated animals (HI/NT, blue bars) of cortex (**c**, **e**) and hippocampus (**d**, **f**) in the ipsilateral side of the brain. Bars display the median and the interquartile range. N (Sham) = 5-6; N (HI/NT) = 10-12. Statistics: Mann-Whitney-U-test (* $p \leq 0.05$; ** $p \leq 0.01$; *** $p \leq 0.001$; **** $p \leq 0.0001$).

3.1.2 NLRP3 pathway activation at 24 h after neonatal HIE

Focusing on the 24 h time point after HI with upregulated NLRP3 pathway proteins in cortex and hippocampus (3.1.1), proteins were additionally analyzed in the thalamus to obtain a complete analysis of the brain. To compare the three brain areas, Shams were combined (figure 18). The proteins of the NLRP3 pathway were upregulated in particular in the hippocampus. Hippocampal NLRP3, GSDMD, cleaved caspase-1 and IL-18 were elevated 24 h after HI (figure 18). The cortex merely showed increased levels of GSDMD and GSDMD-NT. In the thalamus, there was no significant difference between HI/NT and Sham, except GSDMD, which was increased in HI/NT. Taken together, at 24 h after HI, the hippocampus appeared to be the most activated brain region regarding NLRP3.

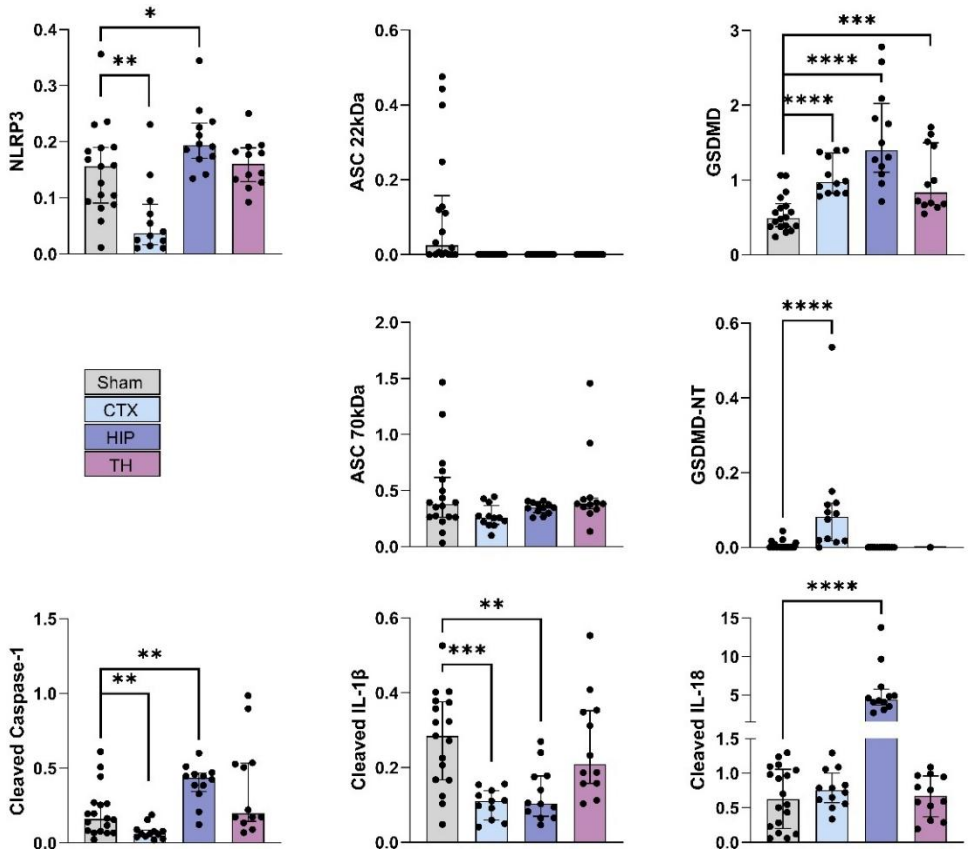

Figure 18: Protein expression of NLRP3 pathway proteins at 24 h after HI. P7 Wistar rats underwent left common carotid artery ligation and subsequently hypoxia treatment for 90 min. Brain areas were taken at 24 h after hypoxia. Western Blot analysis of control animals (Sham, grey bars, ipsilateral hemisphere) vs hypoxia-ischemia/normothermia treated animals, separated in ipsilateral cortex (CTX, light blue bars), hippocampus (HIP, dark blue bars) and thalamus (TH, violet bars). Bars display the median and the interquartile range. N (Sham) = 17-18; N (CTX/HIP/TH) = 12. Statistics: Kruskal-Wallis-test (* $p \leq 0.05$; ** $p \leq 0.01$; *** $p \leq 0.001$; **** $p \leq 0.0001$).

3.1.3 NLRP3 pathway activation at 48 h after neonatal HIE

At 48 h after HI, NLRP3 pathway proteins were upregulated in cortex and hippocampus. The comparison to thalamus was amended to complete the analysis of the ipsilateral hemisphere. To compare the three brain areas, Shams were combined (figure 19).
NLRP3 and cleaved caspase-1 were significantly upregulated in the cortex, GSDMD and GSDMD-NT were significantly increased in the hippocampus. The oligomeric ASC and cleaved IL-1β showed significant elevations in both areas. Thalamus on the other hand, presented a significant increase in cleaved caspase-1 (figure 19). In summary, 48 h after HI appeared to be a time point with increased expression of NLRP3 pathway proteins. The most NLRP3 pathway activation was detected in cortex and hippocampus.

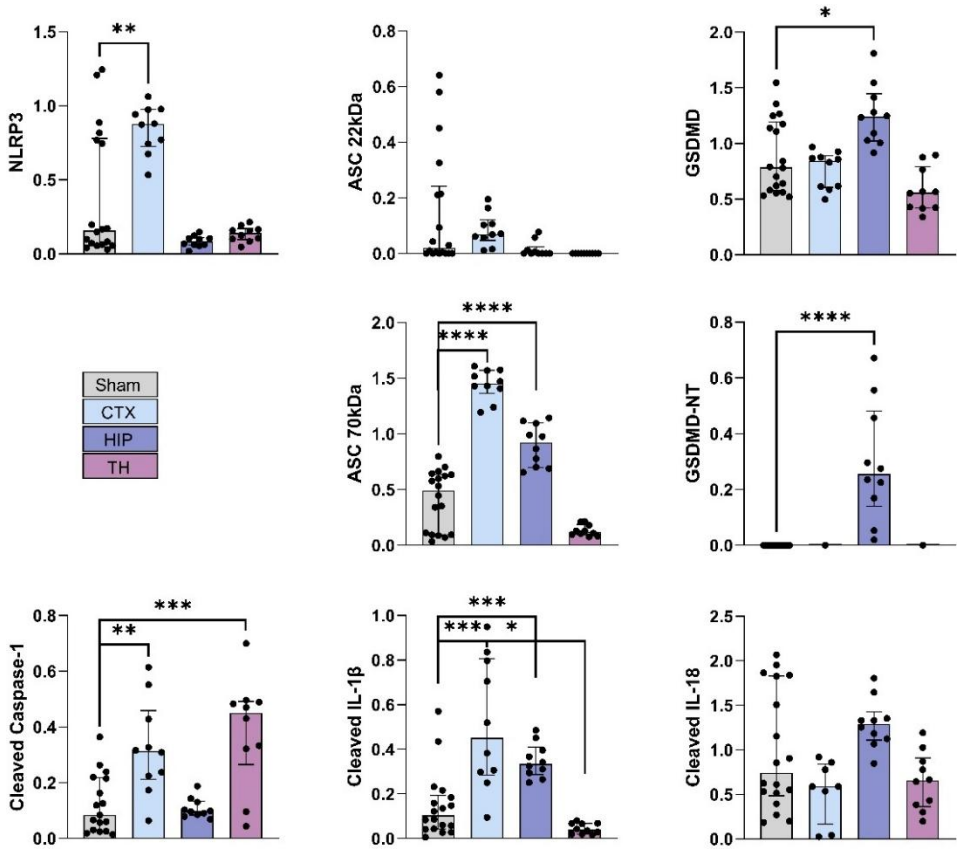

Figure 19: Protein expression of NLRP3 pathway proteins at 48 h after HI. P7 Wistar rats underwent left common carotid artery ligation and subsequently hypoxia treatment for 90 min. Brain areas were taken at 48 h after hypoxia. Western Blot analysis of control animals (Sham, grey bars, ipsilateral hemisphere) vs hypoxia-ischemia/normothermia treated animals, separated in ipsilateral cortex (CTX, light blue bars), hippocampus (HIP, dark blue bars) and thalamus (TH, violet bars). Bars display the median and the interquartile range. N (Sham) = 17-18; N (CTX/HIP/TH) = 10. Statistics: Kruskal-Wallis-test (* $p \leq 0.05$; ** $p \leq 0.01$; *** $p \leq 0.001$; **** $p \leq 0.0001$).

3.2 NLRP3 pathway activation in vitro

3.2.1 Establishment of OGD model in primary microglia

The aim of the first *in vitro* experiments consisted of establishing an OGD model for primary microglial cells. Cells were stressed due to oxygen and glucose deprivation, nonetheless not too stressed to reach a mortality over 30 % (tested with PI staining). Following pilot experiments with different durations and oxygen concentrations of OGD (listed in table 15), suitable conditions were defined.

Table 15: Tested OGD conditions during establishment. Tested oxygen concentration and duration of OGD experiment are listed. Primary rat microglial cells were deprived of glucose and oxygen for a certain amount of time with the aim to induce cellular stress.

O_2 concentration	1 %	0.5 %	0.1 %							
Duration	4 h	4 h	4 h	5 h	6 h	8 h	12 h	15 h	18 h	24 h

After 6 h of OGD in 0.1 % O_2, microglia showed a reduced cell viability (figure 20, blue blot). The combined stimulus of oxygen and glucose deprivation significantly reduced cell viability compared to oxygen or glucose deprivation alone (figure 20, brown blots). LPS treatment alone did not cause a significant change in cell survival. Nevertheless, LPS in combination with OGD resulted in a 40 % reduction of cell viability (figure 20).

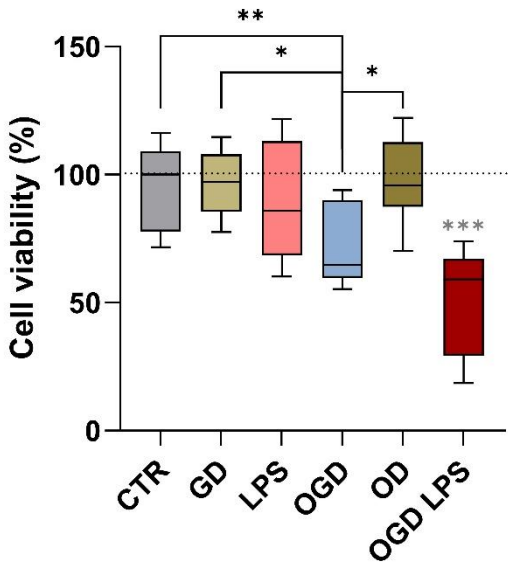

Figure 20: Cell viability of microglia after OGD. Primary microglial cells underwent different treatments (oxygen- and/or glucose-deprivation (0.1 % O_2 for 6 h) and/or LPS treatment (100 ng/ml for 6 h)) and were tested for cell viability via MTT assay. Results of three individual MTT assays with 8 technical replicates in total are represented in boxplots. The values are normalized to the median of the control condition (CTR). The data is identifying OGD and OGD + LPS as conditions with significantly reduced cell viability. CTR = control, GD = glucose-deprivation, OD = oxygen-deprivation. Statistics: Kruskal-Wallis-test (* $p \leq 0.05$; ** $p \leq 0.01$; *** $p \leq 0.001$). Grey asterisks represent the significance compared to the CTR group.

Furthermore, microglia reacted to OGD by changing their morphology. Visualized with the microglia marker Iba-1 in figure 21, microglia showed a ramified phenotype in control conditions, whereas after OGD, they shaped into an amoeboid form representing their active state. OGD effectively activated microglia.

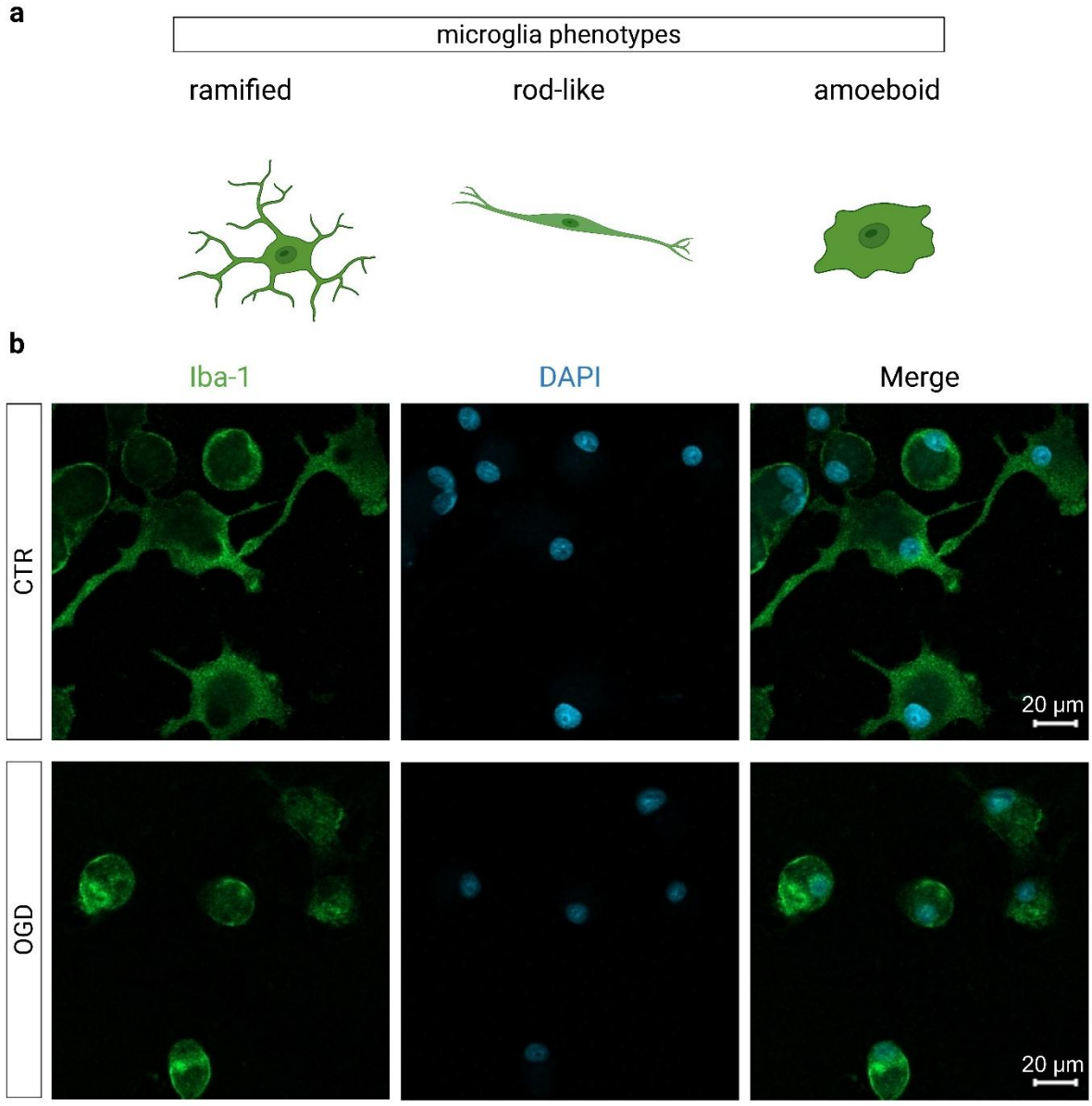

Figure 21: Phenotype of microglia after OGD experiment. **a** Overview of relevant microglia phenotypes. Created with BioRender.com. **b** Exemplary image of microglia exposed to OGD. Microglia were exposed to 6 h of glucose- and oxygen-deprivation (0.1 % O_2) and were fixed directly thereafter. Cells were stained with Iba-1 (green) and DAPI (blue) to represent the morphology comparing the control group (CTR) to the experiment group (OGD). Scale: 20 µm.

3.2.2 Establishment of time point analysis after OGD

Connecting the NLRP3 inflammasome with the microglia activation due to OGD, three key proteins of the NLRP3 pathway, NLRP3, caspase-1 and IL-1β, were analyzed at five different time points. Their transcription levels were assessed with RT-PCR. This overview provided insight into the time-dependent activation of NLRP3 in microglia after OGD (figure 22). NLRP3 showed a significant increase at 2 h, followed by a significant decrease at 8 h (figure 22b). Caspase-1 and IL-1β transcripts were upregulated at 12 h after OGD, indicating the activated downstream pathway of NLRP3 (figure 22c-d). Decreased levels of caspase-1 were presented at 8 h, decreased IL-1β levels at 0 h after OGD.

Based on these findings, a time-dependent activation of the NLRP3 inflammasome pathway was hypothesized. The data presented an upregulation of NLRP3 at 2 h and of caspase-1 and IL-1β at 12 h after OGD. Following experiments were conducted with these time points to further analyze the activation of NLRP3 in microglia.

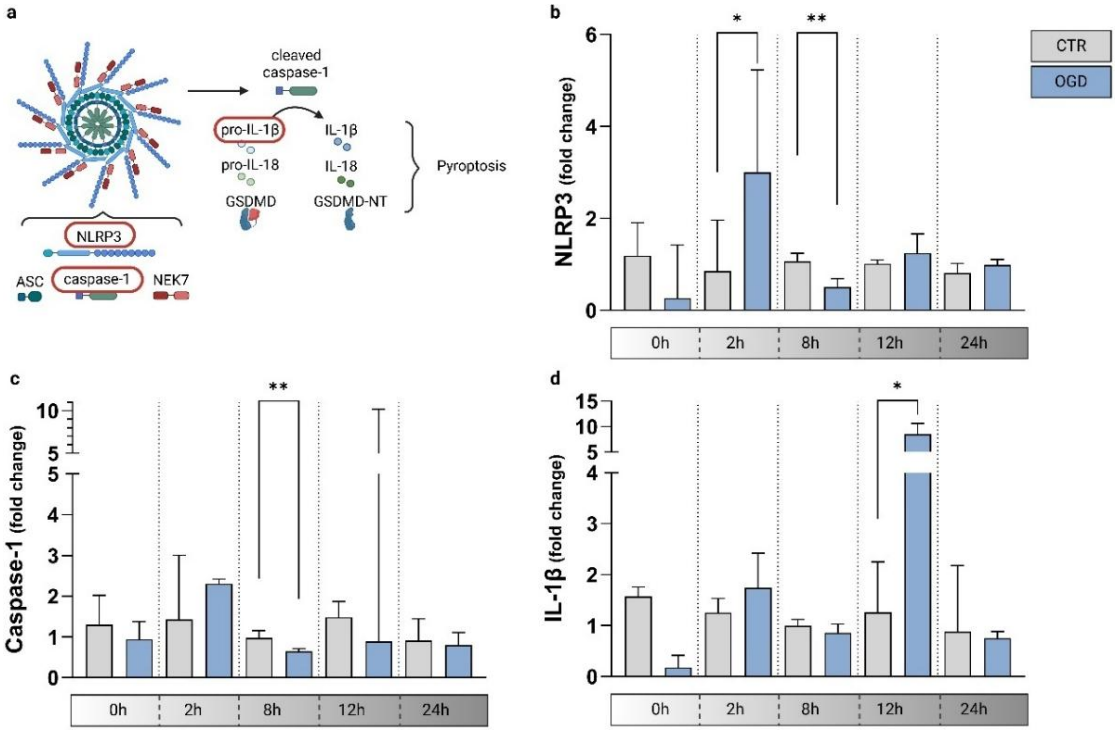

Figure 22: Time point establishment in OGD treated primary microglia. **a** Overview of the NLRP3 pathway with highlighted proteins NLRP3, caspase-1 and IL 1β. Created with BioRender.com. **b-d** RT-PCR analysis of primary microglia exposed to OGD (blue) vs. control cells (grey). The RNA expression of NLRP3 (**b**), caspase-1 (**c**) and IL-1β (**d**) is presented. Five analyzed time points are represented on the x-axis, separated with dotted lines. Bars display the median and the interquartile range of fold changes ($2^{-\Delta\Delta Ct}$). N = 3-6 technical replicates. Statistics: Mann-Whitney-U-test (* $p \leq 0.05$; ** $p \leq 0.01$).

3.2.3 Upstream NLRP3 pathway proteins at 2 h after OGD

Focusing on the 2 h time point after OGD, the transcript levels of four NLRP3 pathway proteins were investigated. The NLRP3 protein presented a significant increase in OGD treated cells compared to control microglia (figure 23). A significant transcriptional increase due to OGD was visible with ASC, the protein, which can be present as monomer, dimer or oligomer depending on its activation (Dick et al., 2016; Guo et al., 2021). Transcripts of caspase-1 and IL-1β did not show any difference between control and OGD. Concluding, figure 23 is presenting upregulated transcripts of upstream pathway proteins.

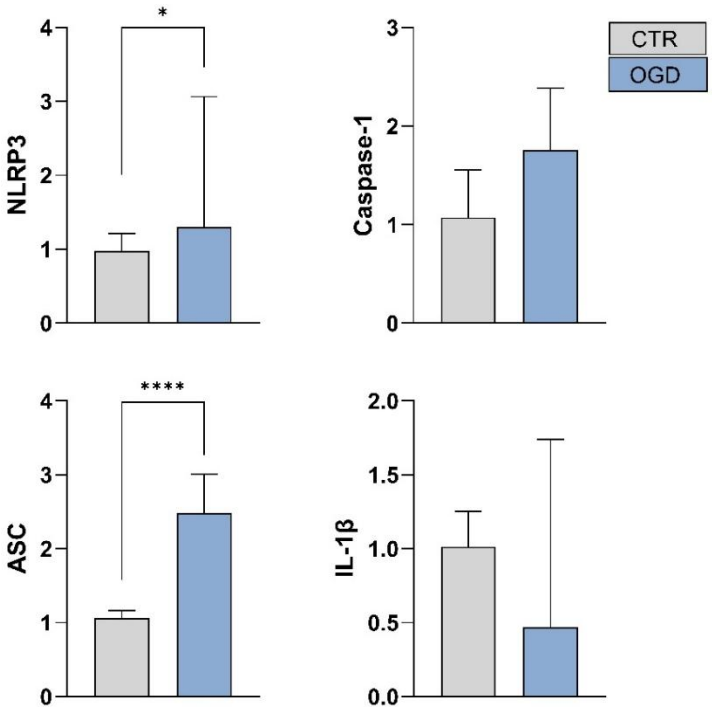

Figure 23: Early transcriptional regulation of NLRP3 pathway proteins in microglia at 2 h after OGD. RT-PCR analysis of primary microglia cells exposed to OGD (blue bars) compared to control cells (grey bars). The RNA expression of NLRP3, caspase-1, ASC and IL-1β is presented. Bars display the median and the interquartile range of fold changes ($2^{-\Delta\Delta Ct}$). N = 8-19 technical replicates. Statistics: Mann-Whitney-U-test (* $p \leq 0.05$; ** $p \leq 0.01$; *** $p \leq 0.001$; **** $p \leq 0.0001$).

3.2.4 Downstream NLRP3 pathway proteins at 12 h after OGD

Transcriptional levels of NLRP3, caspase-1, ASC, IL-1β and GSDMD were examined at 12 h after OGD in primary microglia to focus on downstream pathway proteins. Comparing OGD treated cells to cells in control condition, figure 24 presents three of the five analyzed proteins with increasing trends. The other two protein transcripts not upregulated 12 h after OGD represented NLRP3 and caspase-1, upstream inflammasome pathway proteins. Transcripts of ASC, IL-1β and GSDMD were significantly upregulated due to OGD (figure 24). To summarize, OGD induced an increase in transcriptional levels of downstream pathway proteins at 12 h thereafter.

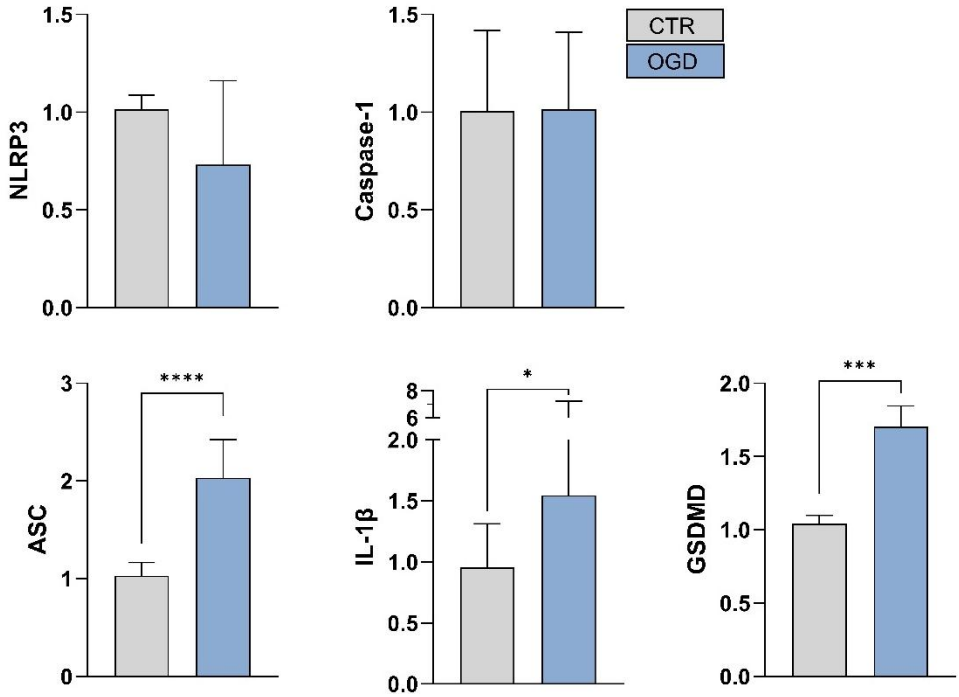

Figure 24: Late transcriptional regulation of NLRP3 pathway proteins in microglia at 12 h after OGD. RT-PCR analysis of primary microglia cells exposed to OGD (blue bars) compared to control cells (grey bars). The RNA expression of NLRP3, caspase-1, ASC, IL-1β and GSDMD is presented. Bars display the median and the interquartile range of fold changes ($2^{-\Delta\Delta Ct}$). N = 9-26 technical replicates. Statistics: Mann-Whitney-U-test (* $p \leq 0.05$; ** $p \leq 0.01$; *** $p \leq 0.001$; **** $p \leq 0.0001$).

3.3 NLRP3 inhibition in vitro

3.3.1 NLRP3 inhibition rescued microglia cell viability and phenotype after OGD

To evaluate the influence of NLRP3 inflammasome activation in the OGD model of microglia, NLRP3 inhibition was conducted using the specific inhibitor Crid3 (Hochheiser et al., 2022). Inhibiting NLRP3 inflammasome formation and activation, no change in cell viability was observed under control conditions (figure 25b, “CC”). The OGD-induced reduction in cell viability (figure 25b, “OGD”) was rescued with NLRP3 inhibition by Crid3 (figure 25b, “OC”). This result emphasized the importance of NLRP3 inflammasome activation in cell viability.

Inhibiting NLRP3 activation under control conditions, the morphology of treated microglia changed by a lower number of branches of their ramified phenotype (figure 25a, “CC”). The number of processes per cell decreased from a median of 2 to 1 and the median process length decreased from 98 µm to 43 µm (figure 25c-d). Compared to the control condition, microglia with inhibited NLRP3 (“CC”) were more activated by expressing more cells with an amoeboid phenotype. Under OGD conditions, the NLRP3 inhibition did partially rescue the amoeboid phenotype due to OGD. Microglia expressed branches, representing their resting state (figure 25a, “OC”). While the median process length and number decreased significantly in OGD conditions compared to control, this morphology change was partially rescued when NLRP3 was inhibited (figure 25c-d). NLRP3 inhibition did affect the phenotype of microglia in the tested OGD model by switching their morphology towards a resting state (figure 25).

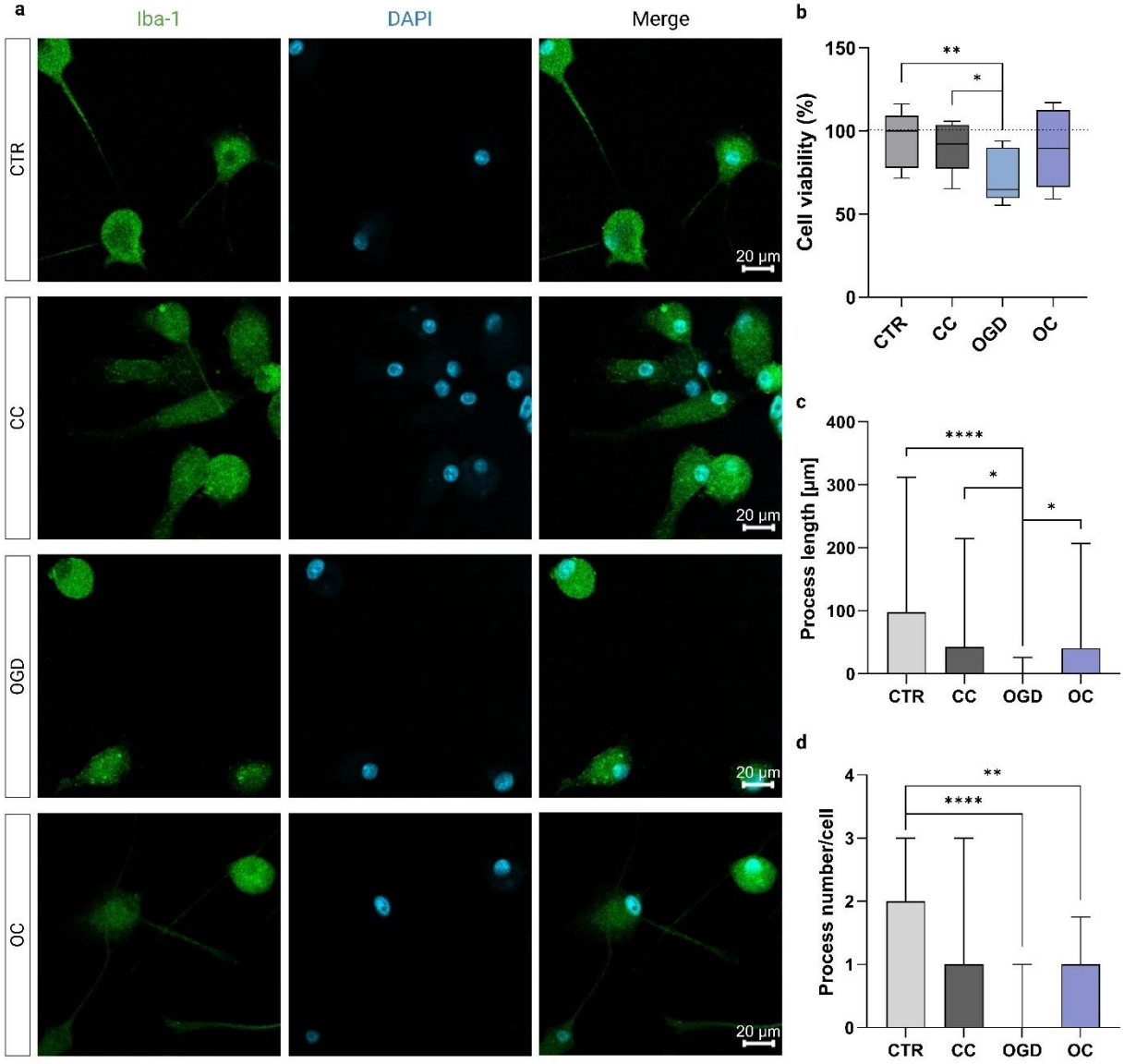

Figure 25: NLRP3 inhibition in primary microglia exposed to OGD. Microglia underwent 6 h of oxygen- and glucose-deprivation (OGD, 0.1 % O_2). 30 min before, cells were treated with 1 µM Crid3 to inhibit NLRP3. Treatment conditions: control (CTR), control with inhibited NLRP3 (CC), OGD, OGD with inhibited NLRP3 (OC). **a** Exemplary images of microglia after OGD when inhibiting NLRP3. After the experiment, the cells were fixed and stained with Iba 1 (green) and DAPI (blue) to show the morphology of the differently treated cells. Scale: 20 µm. **b** Cell viability assay showing the results of three individual MTT assays with 8 technical replicates in total in boxplots. The values are normalized to the control median (CTR). **c-d** Analysis of microglia processes after OGD. Cells were fixed and stained with Iba-1. Analysis of process length and process number per cell were performed with ImageJ. 20 cells were analyzed for each condition. Statistics: Kruskal-Wallis-test (* $p \leq 0.05$; ** $p \leq 0.01$; *** $p \leq 0.001$; **** $p \leq 0.0001$).

3.3.2 Inhibition of transcriptional upregulation of upstream pathway proteins

RT-PCR experiments analyzing the transcriptional regulation of NLRP3 pathway proteins at 2 h after OGD were repeated to validate the data presented in figure 23. New conditions were additionally included in the experiments. NLRP3 inhibition using Crid3 was added to confirm NLRP3-dependent regulation of the transcripts and LPS treatment served as a positive control, displaying the range of transcript levels in activated microglia (figure 26).

Inhibiting NLRP3 led to reduced transcript levels of NLRP3 protein under control (CC) as well as under OGD conditions (OC). The activation with LPS induced a higher increase in transcript level than OGD did. Caspase-1 levels were decreased when NLRP3 inhibition was conducted. The treatment groups CC and OC had a median below 1. The LPS treatment induced the highest increase in caspase-1 transcription. The transcription levels of ASC under CC and OC conditions increased compared to control levels. All treatments did induce a higher ASC transcription compared to control with the highest increase in the OGD group, followed by CC and LPS. The transcription analysis of IL-1β presented decreased values with inhibited NLRP3 and an increase in the positive control LPS compared to the other conditions.

Taken together, except for the analysis of ASC, the other protein analyses presented LPS with the highest values and when inhibiting NLRP3, CC and OC showed decreased values compared to OGD and control (figure 26).

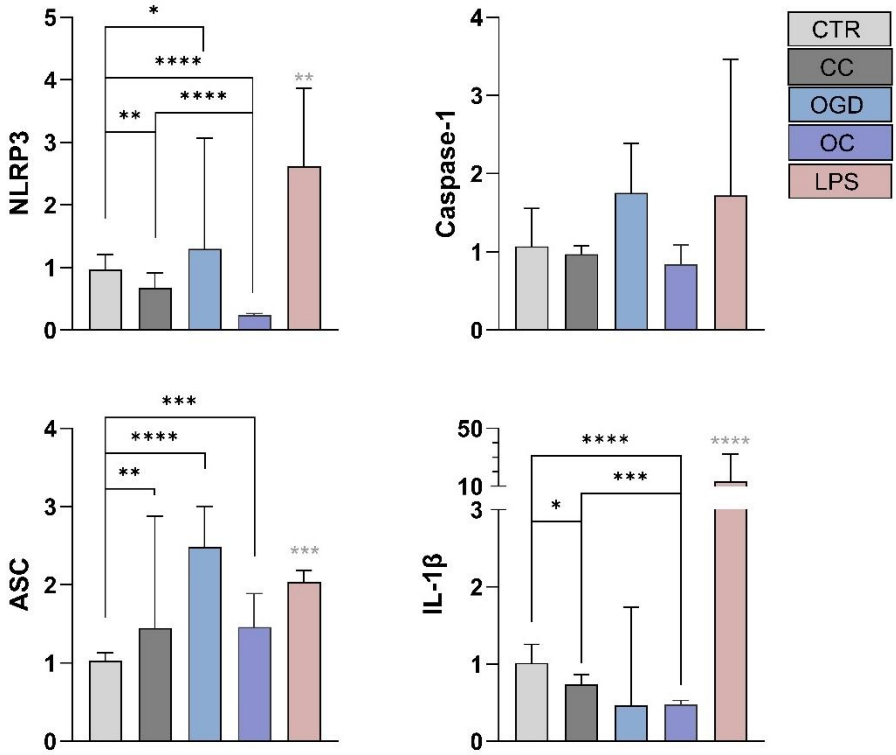

Figure 26: Inhibition of NLRP3 influences transcriptional regulation of NLRP3 pathway proteins in microglia at 2 h after OGD. RT-PCR analysis of primary microglia cells exposed to OGD (OGD, blue bars) and inhibition of NLRP3 with 1 µM Crid3 (OC, dark blue bars) compared to control cells (CTR, grey bars) and inhibition of NLRP3 with 1 µM Crid3 (CC, dark grey bars). The LPS group (LPS, red bars) represents a positive control (6 h treatment with 100 ng/ml LPS). The RNA expression of NLRP3, caspase-1, ASC and IL-1β is presented. Bars display the median and the interquartile range of fold changes ($2^{-\Delta\Delta Ct}$). N = 5-19 technical replicates. Statistics: Kruskal-Wallis-test (* $p \leq 0.05$; ** $p \leq 0.01$; *** $p \leq 0.001$; **** $p \leq 0.0001$). Grey asterisks represent the significance compared to the CTR group.

3.3.3 Inhibition of transcriptional upregulation of downstream pathway proteins

To validate the data presented in figure 24, RT-PCR experiments were conducted at 12 h after OGD including new conditions with NLRP3 inhibition using Crid3 and a LPS treatment as positive control (figure 27). The NLRP3 inhibition prevented the OGD-induced increase in transcript levels of NLRP3 pathway proteins (figure 27).

NLRP3 transcription was not induced due to OGD at this time point. The only increase was shown in the positive control LPS. The transcription of caspase-1 was similarly increased in LPS and in OGD, declaring OGD as a suitable stimulus to cause caspase-1 upregulation. Likewise, OGD stimulated ASC transcription at the same level as the

positive control LPS. IL-1β transcription was significantly upregulated in OGD compared to control. GSDMD showed a similar transcriptional increase in OGD and OC, which suggested the inefficacy of NLRP3 inhibition at the transcriptional, not functional level of GSDMD (figure 27).

Based on these results, the inhibition of NLRP3 demonstrated the NLRP3-dependent transcriptional upregulation of NLRP3 pathway components after OGD. The activation state of the proteins could not be analyzed via RT-PCR, nonetheless the downstream pathway proteins indicated NLRP3 inflammasome activation.

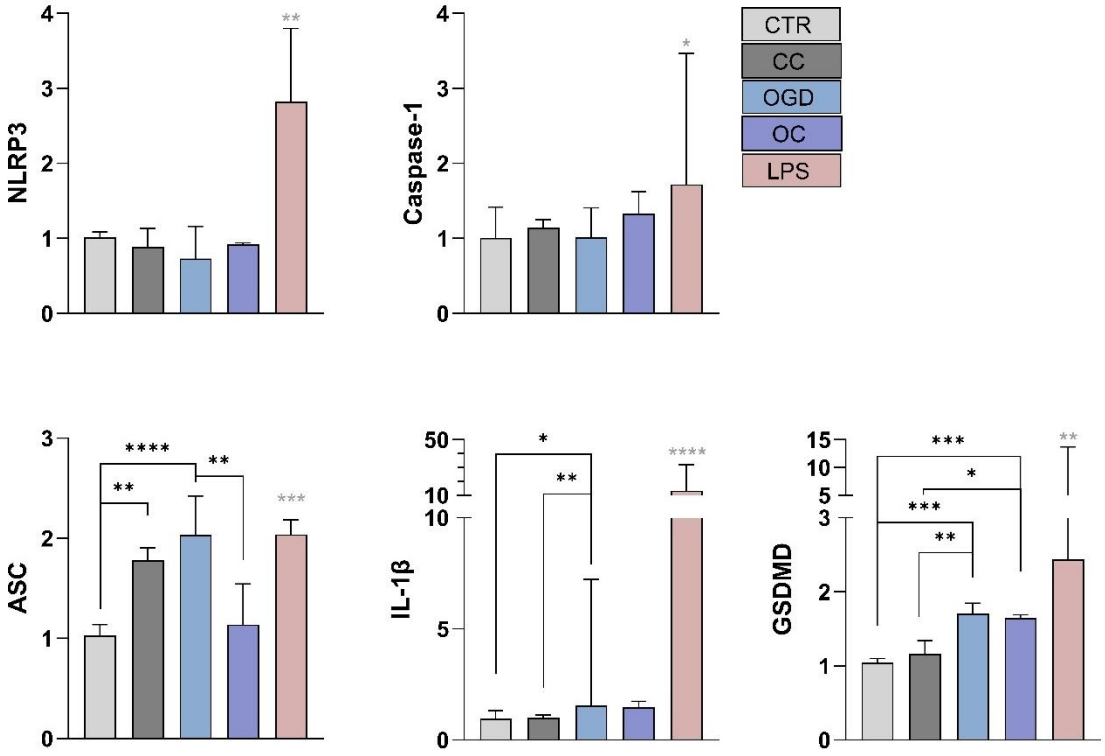

Figure 27: Inhibition of NLRP3 influences transcriptional regulation of NLRP3 pathway proteins in microglia at 12 h after OGD. RT-PCR analysis of primary microglia cells exposed to OGD (OGD, blue bars) and inhibition of NLRP3 with 1 µM Crid3 (OC, dark blue bars) compared to control cells (CTR, grey bars) and inhibition of NLRP3 with 1 µM Crid3 (CC, dark grey bars). The LPS group (LPS, red bars) represents a positive control (6 h treatment with 100 ng/ml LPS). The RNA expression of NLRP3, caspase-1, ASC, IL-1β and GSDMD is presented. Bars display the median and the interquartile range of fold changes ($2^{-\Delta\Delta Ct}$). N = 5-26 technical replicates. Statistics: Kruskal-Wallis-test (* $p \leq 0.05$; ** $p \leq 0.01$; *** $p \leq 0.001$; **** $p \leq 0.0001$). Grey asterisks represent the significance compared to the CTR group.

3.3.4 Influence of activated microglia on neurons

3.3.4.1 Supernatant of activated microglia induced cell stress in neurons

To verify the NLRP3 inflammasome activation in microglia after OGD and to research its influence on other cells, the next experiment was performed by incubating neuronal cells with activated microglia supernatant. The hypothesis that activated microglia release inflammatory factors and thereby lead to inflammatory reactions in other cell types, was investigated by measuring the protein expression of apoptotic and inflammatory markers in neuronal cells and by estimating their cell viability (figure 28).

After 24 h incubation with microglia supernatant, the results presented OGD-activated microglia inducing inflammation and apoptosis in neurons. The OGD supernatant did increase protein expression of the apoptosis marker BAX/BCL-2 ratio and cleaved caspase-9, as well as the inflammatory marker IL-1β (figure 28, “OGD SN” compared to “CTR SN”). The BAX/BCL-2 ratio did not show a decrease due to NLRP3 inhibition (figure 28b). However, the downstream marker for apoptosis cleaved caspase-9 showed a significant reduction in the OC SN group compared to OGD SN (figure 28c). Furthermore, the inflammation marker IL-1β presented a reduction in increasing protein expression due to OGD when inhibiting NLRP3, highlighting the effect on neuronal cells when microglial NLRP3 was inhibited (figure 28d).

The control groups “PC12 m” and “microglia m” for testing the isolated effect of different cell culture medium on neuronal cell fate did not show any upregulation in protein expression of the three tested proteins. The positive control with supernatant from LPS treated microglia led to the highest protein expression in BAX/BCL-2 ratio and cleaved IL-1β. In cleaved caspase-9 however, there was no increase detectable.

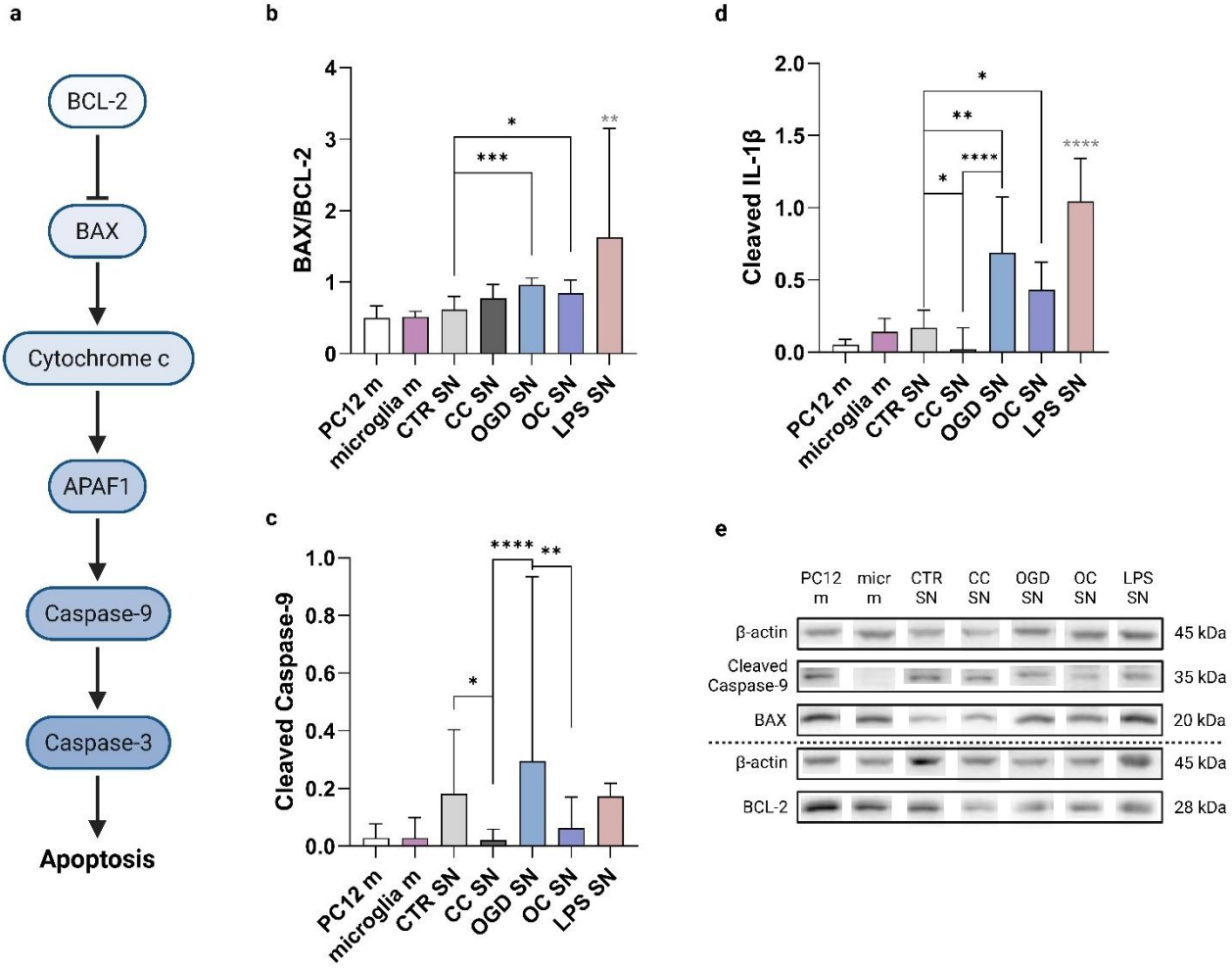

Figure 28: Protein analysis of apoptosis and inflammation markers in PC12 neurons treated with conditioned microglia supernatant. **a** Overview of the apoptosis pathway via BCL-2, BAX and caspase-9. Created with BioRender.com. **b-d** Western Blot analysis of PC12 neurons treated with different conditions. PC12 m = culture medium of PC12 cells, microglia m = culture medium of microglia in 1:1 ratio to neuronal culture medium, CTR/CC/OGD/OC SN = supernatant of differently treated microglia at 24 h after conducted OGD experiment in 1:1 ratio to neuronal culture medium, LPS SN = supernatant of microglia undergoing 6 h treatment with 100 ng/ml LPS in 1:1 ratio to neuronal culture medium. Bars display the median and the interquartile range. Technical replicates in total of 3 biological replicates: N (LPS SN) = 6; N (PC12 m/microglia m/CC SN/OC SN) = 10; N (CTR SN/OGD SN) = 16. Statistics: Kruskal-Wallis-test (* $p \leq 0.05$; ** $p \leq 0.01$; *** $p \leq 0.001$; **** $p \leq 0.0001$). Grey asterisks represent the significance compared to the CTR group. **e** Exemplary Western Blot bands of cleaved caspase-9, BAX, BCL-2 and β-actin comparing the treatment groups.

In addition, the effect of activated microglia supernatant on neuronal cells was determined by cell viability. Supernatant from OGD treated microglia induced a reduction in cell viability (figure 29). The inhibition of NLRP3 led to a comparable median, nonetheless, the

individual values of the “OC SN” condition showed a higher variability with half of the values being over 100 %, whereas the “OGD SN” values dominantly were below 100 %. The positive control “LPS SN” presented the lowest median with 69 % (figure 29). Taken together, the supernatant of activated microglia induced apoptotic and inflammatory pathways in neurons in a NLRP3-dependent matter.

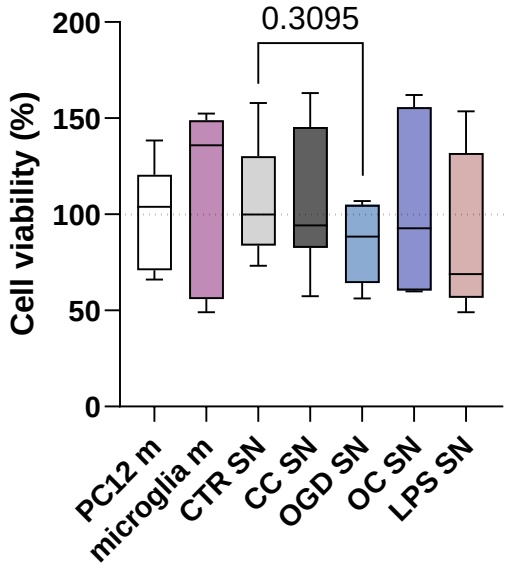

Figure 29: Cell viability of neurons after treatment with conditioned microglia supernatant. PC12 neuronal cells underwent 24 h incubation with supernatant of microglia 24 h after exposed to different treatments and were tested for cell viability via MTT assays. Results of six samples per condition are represented in boxplots. The values are normalized to the median of the control supernatant condition (CTR SN). The results do not show significant differences between the conditions (Kruskal-Wallis-test (p-values of ≤ 0.05)). PC12 m = culture medium of PC12 cells, microglia m = culture medium of microglia in 1:1 ratio to neuronal culture medium, CTR/CC/OGD/OC SN = supernatant of differently treated microglia at 24 h after conducted OGD experiment in 1:1 ratio to neuronal culture medium, LPS SN = supernatant of microglia undergoing 6 h treatment with 100 ng/ml LPS in 1:1 ratio to neuronal culture medium.

3.3.4.2 Protein analysis of activated microglia indicated NLRP3 involvement

The processes within microglia, which resulted in supernatants effecting neuronal cells, were investigated for the involvement of NLRP3 inflammasome activation. Therefore, the active forms of the effector protein caspase-1 and the target protein IL-1β were analyzed on their protein level in microglia at 24 h after OGD (figure 30).

OGD induced an increase in cleaved caspase-1 and IL-1β. Crid3 treatment partially reduced this increase, decreasing the protein level close to control (“OC”, figure 30). In cleaved caspase-1, OGD showed comparable values as the positive control LPS, suggesting OGD being a suitable stimulus to activate caspase-1. In cleaved IL-1β, LPS presented a median almost five times as high as OGD, underlining IL-1β being activated through many pathways, different from the ones triggered through OGD.

At protein level, there was no significant increase in NLRP3-activated proteins due to OGD. Nonetheless, the inhibition with Crid3 reduced the elevation, proving the increase of proteins being NLRP3-dependent.

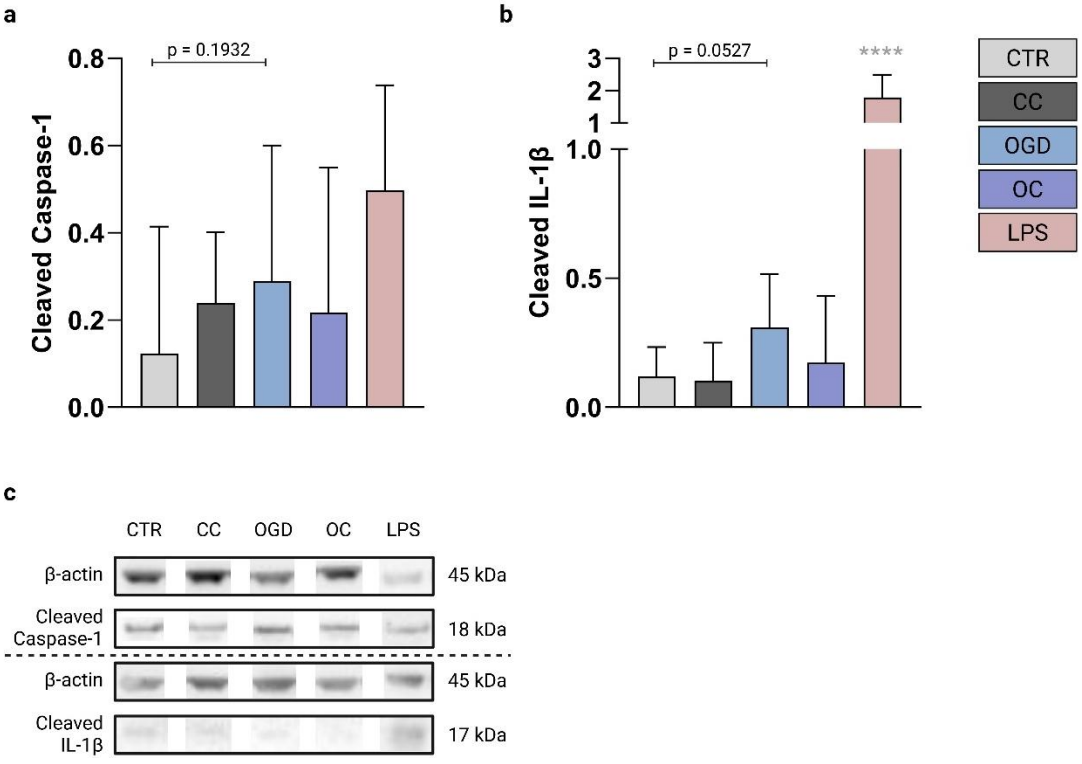

Figure 30: Protein analysis of cleaved caspase-1 and IL-1β in microglia. 24 h after OGD, microglia were analyzed via Western Blot. **a**-**b** Graphs represent the conditions CTR = control, CC = control + Crid3, OGD, OC = OGD + Crid3 and LPS as positive control (6 h treatment with 100 ng/ml LPS). Bars display the median and the interquartile range. Technical replicates in total of 3 biological replicates: N (CTR/OGD) = 11/15; N (CC/OC) = 10; N (LPS) = 6. Statistics: Kruskal-Wallis-test (**** $p \leq 0.0001$). Grey asterisks represent the significance compared to the CTR group. **c** Exemplary Western Blot bands of cleaved caspase-1, cleaved IL-β and β-actin comparing the treatment groups.

3.3.4.3 Analysis of microglia supernatant

To comprehend the cause of the effect the microglia supernatant is having on neurons, the supernatant was analyzed. With ELISA, the level of released IL-1β was studied. IL-1β represented one of the downstream targets of NLRP3 inflammasome activation, turning it into a suitable marker for inflammasome activation. To test the release of IL-1β specifically due to NLRP3, NLRP3 inhibition was conducted.

Showed by figure 31, the OGD treatment did induce a non-significant increase in IL-1β release. Compared to the control groups CTR and CC, which presented similar values of the replicates, the groups OGD, OC and LPS showed a high range in IQR. Inhibiting NLRP3, the elevated IL-1β release by OGD, was reduced. LPS demonstrated the highest median, significantly elevated compared to control (figure 31).

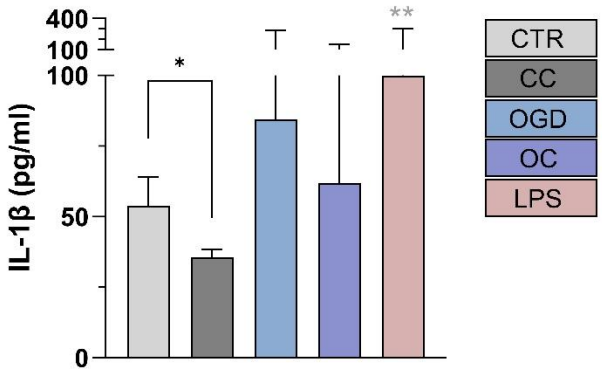

Figure 31: Supernatant analysis of microglia via IL-1β ELISA. Supernatant was collected from primary microglia cells 24 h after 6 h OGD treatment. LPS represents a positive control, the cells did undergo 6 h of LPS treatment (100 ng/ml). CC = control + Crid3, OC = OGD + Crid3. Bars display the median and the interquartile range. N = 5. Statistics: Kruskal-Wallis-test (* $p \leq 0.05$; ** $p \leq 0.01$). Grey asterisks represent the significance compared to the CTR group.

3.3.5 Impact of NLRP3 activation on metabolic activity of microglia

An additional experiment analyzing the microglia supernatant was provided with mass spectrometry. Using AHA-labelled protein detection in the supernatant, synthesized proteins in a time range of 24 h following OGD were quantified, enabling the analysis of metabolic activity of microglia. Different treatment conditions were compared to analyze the effect of NLRP3 activation after HI (figure 32).

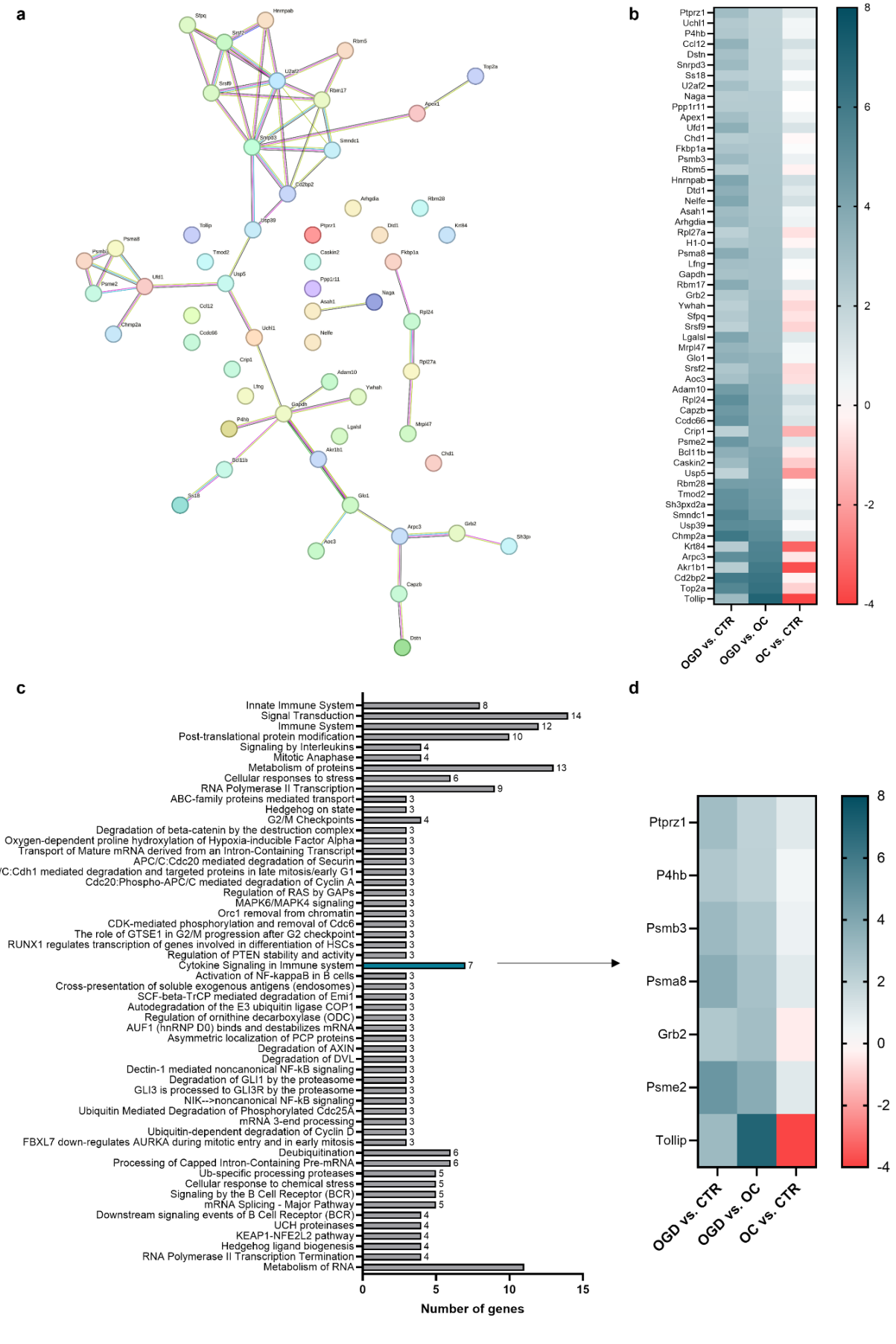
a
b
c
d
Innate Immune System
Signal Transduction
Immune System
Post-translational protein modification
Signaling by Interleukins
Mitotic Anaphase
Metabolism of proteins
Cellular responses to stress
RNA Polymerase II Transcription
ABC-family proteins mediated transport
Hedgehog on state
G2/M Checkpoints
Degradation of beta-catenin by the destruction complex
Oxygen-dependent proline hydroxylation of Hypoxia-inducible Factor Alpha
Transport of Mature mRNA derived from an Intron-Containing Transcript
APC/C:Cdc20 mediated degradation of Securin
APC/C:Cdh1 mediated degradation and targeted proteins in late mitosis/early G1
Cdc20:Phospho-APC/C mediated degradation of Cyclin A
Regulation of RAS by GAPs
MAPK6/MAPK4 signaling
Orc1 removal from chromatin
CDK-mediated phosphorylation and removal of Cdc6
The role of GTSE1 in G2/M progression after G2 checkpoint
RUNX1 regulates transcription of genes involved in differentiation of HSCs
Regulation of PTEN stability and activity
Cytokine Signaling in Immune system
Activation of NF-kappaB in B cells
Cross-presentation of soluble exogenous antigens (endosomes)
SCF-beta-TrCP mediated degradation of Emi1
Autodegradation of the E3 ubiquitin ligase COP1
Regulation of ornithine decarboxylase (ODC)
AUF1 (hnRNP D0) binds and destabilizes mRNA
Asymmetric localization of PCP proteins
Degradation of AXIN
Degradation of DVL
Dectin-1 mediated noncanonical NF-kB signaling
Degradation of GLI1 by the proteasome
GLI3 is processed to GLI3R by the proteasome
NIK-->noncanonical NF-kB signaling
Ubiquitin Mediated Degradation of Phosphorylated Cdc25A
mRNA 3-end processing
Ubiquitin-dependent degradation of Cyclin D
FBXL7 down-regulates AURKA during mitotic entry and in early mitosis
Deubiquitination
Processing of Capped Intron-Containing Pre-mRNA
Ub-specific processing proteases
Cellular response to chemical stress
Signaling by the B Cell Receptor (BCR)
mRNA Splicing - Major Pathway
Downstream signaling events of B Cell Receptor (BCR)
UCH proteinases
KEAP1-NFE2L2 pathway
Hedgehog ligand biogenesis
RNA Polymerase II Transcription Termination
Metabolism of RNA
0
5
10
15
Number of genes
OGD vs. CTR
OGD vs. OC
OC vs. CTR
8
6
4
2
0
-2
-4

Figure 32: NLRP3-specific microglial protein synthesis after OGD. Primary microglia were exposed to 6 h of OGD (0.1 % O_2). 30 min before, cells were treated with 1 µM Crid3 to inhibit NLRP3 (OC). During 24 h of reoxygenation, the protein synthesis was labelled with AHA. Supernatant was processed for MS analysis with 4 biological replicates. **a** STRING network of genes specific for NLRP3 activation after OGD (string-db.org). **b** Heat map of synthesized genes with displayed log2FC. **c** Reactome pathway analysis, performed with string database (string-db.org). **d** Heat map of synthesized genes, identified for cytokine signaling in immune system with displayed log2FC. Differential protein abundance was assessed with limma, fitting linear models with empirical Bayes moderation and correcting p-values using the Benjamini-Hochberg FDR (p-values of ≤ 0.05).

When analyzing synthesized proteins during 24 h after OGD in microglia supernatant via mass spectrometry, 57 genes of proteins were found specifically increased due to NLRP3 activity in OGD treated microglia (figure 32a-b). They were identified by increased expression after OGD treatment compared to control condition (CTR) and NLRP3 inhibition (OC) and they should not be expressed higher in OC compared to CTR.
The 57 genes were analyzed with the STRING database for their reactome pathways (figure 32c) and gene ontology (supplementary figure 1) to reveal their connection to biological processes, molecular function and cellular components.
Analyzing the reactome pathway “cytokine signaling in immune system”, 7 genes were identified, protein tyrosine phosphatase receptor type Z1 (Ptprz1), prolyl 4-hydroxylase subunit beta (P4hb), the proteasome subunits (Psmb3, Psma8 and Psme2), the growth factor receptor bound protein 2 (Grb2) and the toll interacting protein (Tollip) (figure 32d). Tollip showed the biggest difference in expression comparing OGD to inhibited NLRP3 under OGD conditions (OC) (figure 32d).

3.4 NLRP3 inhibition in vivo

3.4.1 Efficiency of NLRP3 inhibition dependent on different injection conditions

We compared three different concentrations of Crid3 and two different injection schemes to find out the best condition to inhibit NLRP3 *in vivo*. The NLRP3 inhibition efficiency was analyzed at 48 h after HI based on previous experiments indicating this a suitable time point for NLRP3 activation. Diverse effects were observed with the treatments. NLRP3 and cleaved caspase-1 were upregulated in the HI/Vehicle group compared to Sham. The expression of cleaved IL-1β did not increase at this time point. Comparing the two injection

schemes, the data presented the injections at 30 min before and 24 h after HI as the more effective injection scheme for significant NLRP3 inhibition. The dose of 5 mg/kg showed the best inhibition and thereby was validated for further experiments (figure 33).

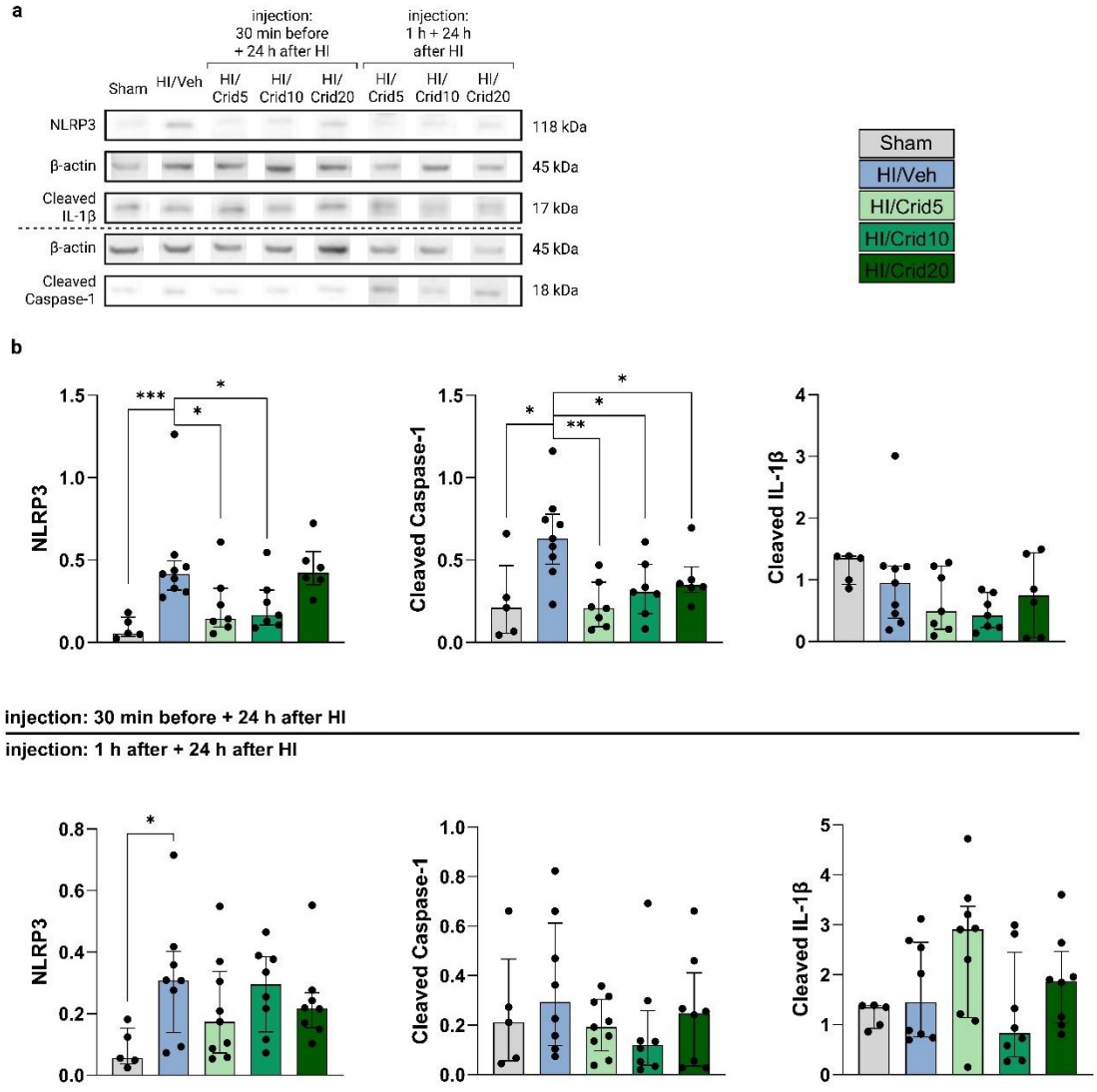

Figure 33: Treatment establishment of NLRP3 inhibitor Crid3 in the animal model of HIE. Comparison of protein expression of NLRP3 pathway proteins at 48 h after HI in the ipsilateral cortex. P7 Wistar rats underwent left common carotid artery ligation and hypoxia for 90 min. Animals were i.p. injected at different time points with different doses of Crid3. **a** Exemplary Western Blot bands of analyzed proteins. **b** Western Blot results comparing control animals (Sham, grey) vs hypoxia-ischemia/normothermia treated animals injected with vehicle (HI/Veh, blue) vs Crid3. Different doses of Crid3 were 5 mg/kg (HI/Crid5, light green) vs 10 mg/kg (HI/Crid10, green) vs 20 mg/kg (HI/Crid20, dark green). The graphs in the upper part of **b** show injections of the doses at 30 min before and 24 h after HI. The graphs in the bottom part of **b** show injections of the doses at 1 h and 24 h after HI. Bars display the median and the interquartile range. N (Sham) = 5; N (HI/Veh) = 8-9; N (HI/Crid5) = 7-9; N (HI/Crid10) = 7-8; N (HI/Crid20) = 6-8. Statistics: Kruskal-Wallis-test (* $p \leq 0.05$; ** $p \leq 0.01$; *** $p \leq 0.001$).

3.4.2 Inhibiting NLRP3 reduced pathway proteins after neonatal HIE

Proteins of the NLRP3 pathway were analyzed at 24 h and 48 h after HI in the ipsilateral cortex and hippocampus. Their expression was compared in Sham, HI/Vehicle (HI/Veh) and HI/5 mg/kg Crid3 (HI/Crid) treated animals (figure 34 and 35).

At 24 h after HI, the proteins NLRP3, cleaved IL-1β and IL-18, GSDMD and GSDMD-NT were upregulated in HI/Vehicle in both brain areas. Caspase-1 and cleaved caspase-1 were only upregulated in the cortical area (figure 34). ASC was analyzed at its monomer and oligomer form. Neither of both protein structures showed an upregulation at this time point. When inhibiting NLRP3, the protein upregulation was efficiently prevented in both areas for caspase-1, cleaved caspase-1, cleaved IL-1β and IL-18 and GSDMD. In hippocampus only, NLRP3 and GSDMD-NT were inhibited to increase due to HI.

At 48 h after HI, HI increased the expression of NLRP3, caspase-1 and cleaved caspase-1, oligomeric ASC, GSDMD and GSDMD-NT in the cortex. Whereas in the hippocampus, NLRP3, monomeric and oligomeric ASC, GSDMD and GSDMD-NT were increased (figure 35). The interleukins were not upregulated due to HI at this time point. Inhibiting NLRP3 reduced the protein increase. NLRP3, caspase-1 and cleaved caspase-1 showed a significant reduction due to Crid3 (figure 35).

Taken together, the increase in protein expression due to HI was reduced with the usage of the NLRP3 inhibitor Crid3. Similar trends were observed in cortex and hippocampus with the cortex expressing a higher amount of the NLRP3 protein, indicating a more essential role for this pathway (figure 35).

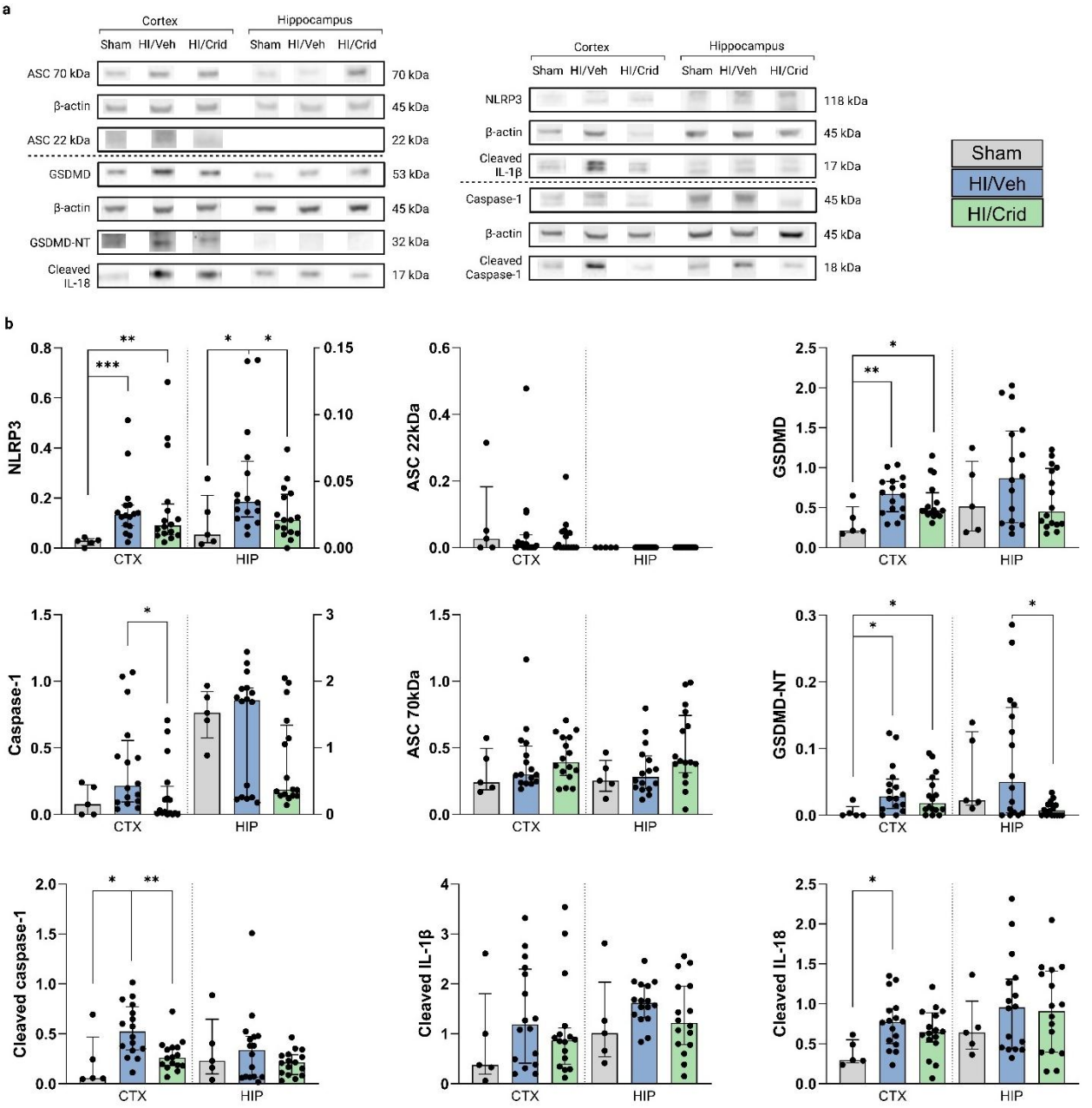

Figure 34: Effect of NLRP3 inhibition on protein expression of NLRP3 pathway proteins at 24 h after HI. P7 Wistar rats underwent left common carotid artery ligation and subsequently hypoxia treatment for 90 min. Animals were either injected with vehicle or 5 mg/kg Crid3 at 30 min before and 24 h after HI. Animals were sacrificed and brain areas were taken at 24 h after hypoxia. **a** Exemplary Western Blot bands of analyzed proteins comparing the treatment groups. **b** Western Blot results comparing control animals (Sham, grey bars) vs hypoxia-ischemia/normothermia treated animals injected with vehicle (HI/Veh, blue bars) vs hypoxia-ischemia/normothermia treated animals injected with 5 mg/kg Crid3 (HI/Crid, light green bars). Dotted lines separate cortex (CTX) and hippocampus (HIP). Bars display the median and the interquartile range. N (Sham) = 5; N (HI/Veh) = 16; N (HI/Crid) = 16. Statistics: Kruskal-Wallis-test (* $p \leq 0.05$; ** $p \leq 0.01$; *** $p \leq 0.001$).

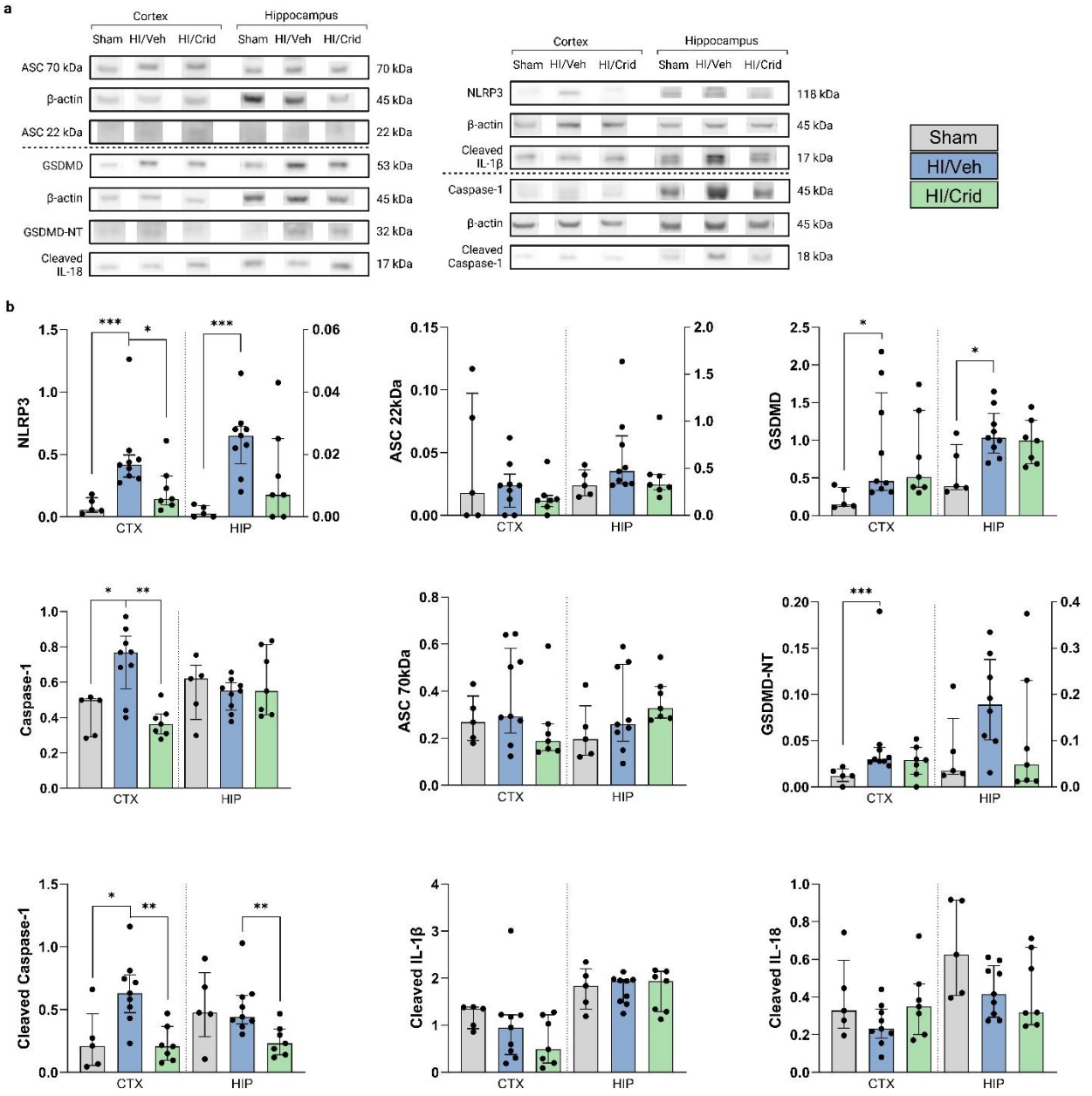

Figure 35: Effect of NLRP3 inhibition on protein expression of NLRP3 pathway proteins at 48 h after HI. P7 Wistar rats underwent left common carotid artery ligation and subsequently hypoxia treatment for 90 min. Animals were either injected with vehicle or 5 mg/kg Crid3 at 30 min before and 24 h after HI. Animals were sacrificed and brain areas were taken at 48 h after hypoxia. **a** Exemplary Western Blot bands of analyzed proteins comparing the treatment groups. **b** Western Blot results comparing control animals (Sham, grey bars) vs hypoxia-ischemia/normothermia treated animals injected with vehicle (HI/Veh, blue bars) vs hypoxia-ischemia/normothermia treated animals injected with 5 mg/kg Crid3 (HI/Crid, light green bars). Dotted lines separate cortex (CTX) and hippocampus (HIP). Bars display the median and the interquartile range. N (Sham) = 5; N (HI/Veh) = 9; N (HI/Crid) = 7. Statistics: Kruskal-Wallis-test (* $p \leq 0.05$; ** $p \leq 0.01$; *** $p \leq 0.001$).

3.4.3 Inhibition of NLRP3 reduced brain area loss after neonatal HIE

At two different time points after HI, the animals' brains were scanned via MRI. The brain damage resulting from the hypoxic-ischemic injury was validated at P14 and P81. Compared to Sham, HI/Vehicle animals presented a significant increase in brain area loss (figure 36). Between the two time points, no significant elevation in brain edema size was detected. Animals treated with the NLRP3 inhibitor Crid3 presented a reduction in brain area loss, significant at P14 (figure 36). Between sexes, no difference was detected. In summary, the results underline the impact of the NLRP3 inflammasome on brain damage development after HI.

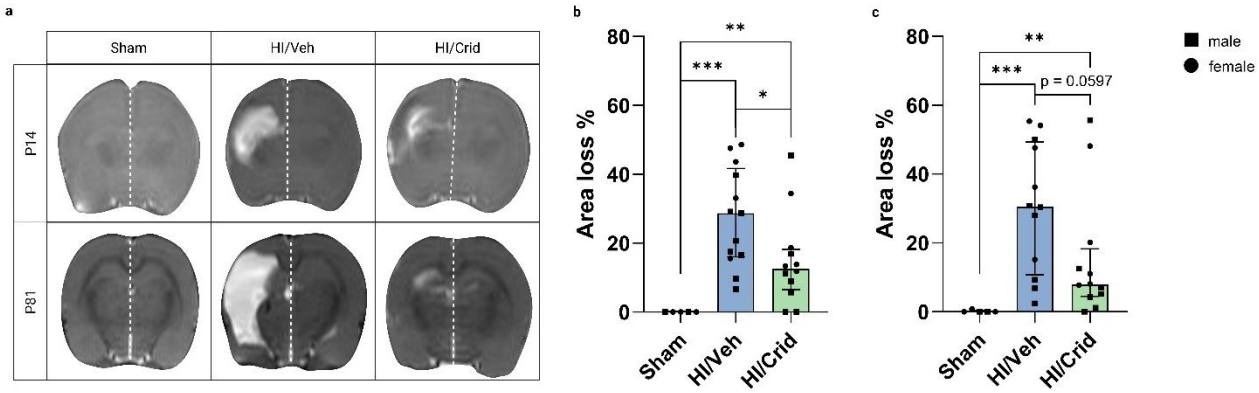

Figure 36: Brain area loss after neonatal HIE reduced by inhibiting NLRP3. P7 Wistar rats underwent left common carotid artery ligation and subsequently hypoxia treatment for 90 min. Treatment groups: Sham, HI/Vehicle and HI/Crid (5 mg/kg Crid3); injections at 30 min before and 24 h after HI. Animals were scanned in MRI at 7 and 74 days after HI and brain area loss was measured using T2-weighted imaging. **a** Exemplary MRI images. Hemispheres are separated with a dotted line. **b-c** Area loss (%) of brains with different treatments at P14 (**b**) and P81 (**c**). Bars represent median values and the interquartile range. Males are indicated with squares; females are indicated with circles. N (Sham) = 5, N (HI/Veh, HI/Crid) = 12. Statistics: Kruskal-Wallis-test (* $p \leq 0.05$; ** $p \leq 0.01$; *** $p \leq 0.001$).

3.4.4 NLRP3 inhibition rescued behavioral impairment after neonatal HIE

Long-term effects of the Crid3 treatment and HI were assessed with behavior tests. On motoric and cognitive level, the results emphasized the effect of the HI insult. Animals undergoing HI/Vehicle treatment showed impaired motoric behavior with a prolonged run duration. The step cycle duration and the paw stand increased and led to a reduced average speed of the run (figure 37a-f). The treatment with the NLRP3 inhibitor Crid3 reduced the impairment by increasing the walking speed of the animals (figure 37a-f). In

NOR, HI/Vehicle animals spent less time discovering the novel object (figure 37g-i). The Sham controls showed 1.5 times as many contacts with the novel objects than HI treated animals (figure 37h). Inhibiting NLRP3 with Crid3 could not rescue the HI-induced impairment (figure 37g-i). Between the sexes, no difference was visible when analyzing the behavior. Taken together, the behavioral impairment due to HI was prevented with the inhibition of NLRP3 on a motoric, but not on a cognitive level. There was no correlation between behavior and brain area loss (supplementary figure 2).

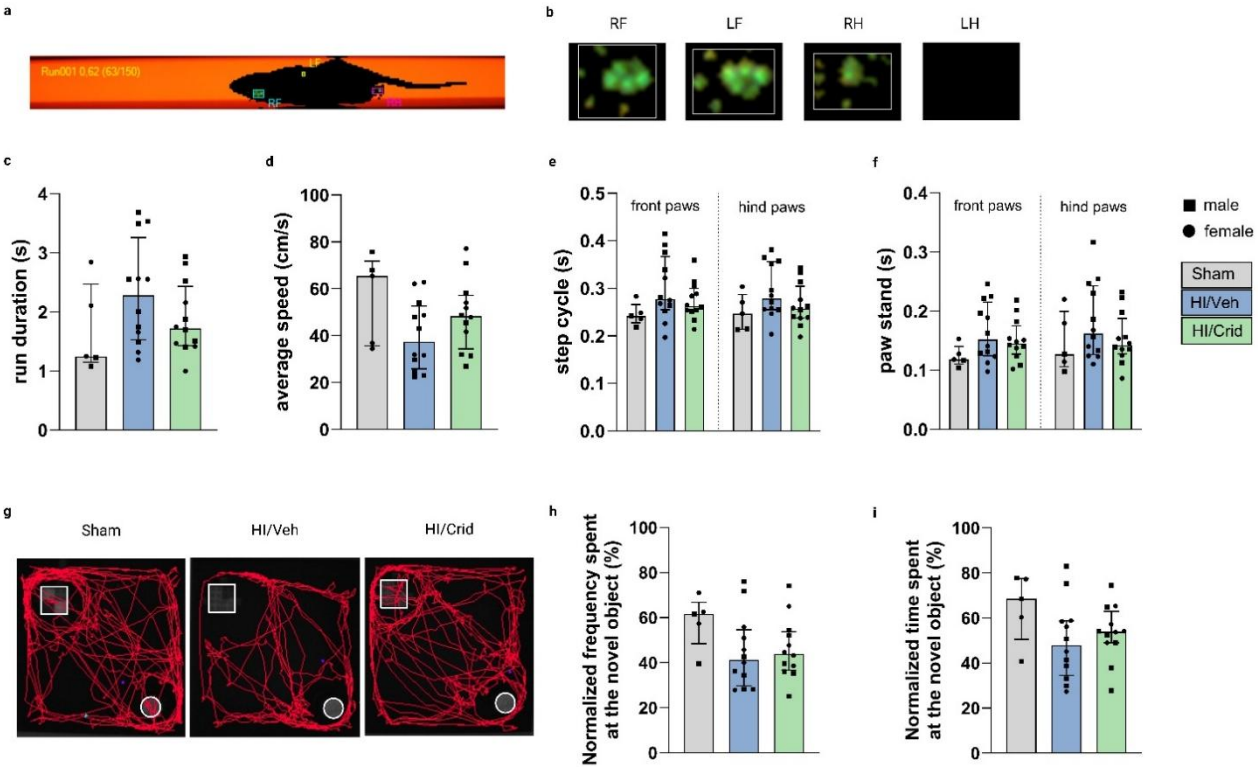

Figure 37: NLRP3 inhibition affects behavioral impairment after neonatal HIE. P7 Wistar rats underwent left common carotid artery ligation and subsequently hypoxia treatment for 90 min. Treatment groups: Sham, HI/Vehicle and HI/Crid (5 mg/kg Crid3); injections at 30 min before and 24 h after HI. **a-f** Motoric impairments were tested with Catwalk test at P48. **a** Exemplary image of rat walking through the CatWalk setup. **b** Exemplary images of right front (RF), left front (LF), right hind (RH) and left hind (LH) paw. **c-f** Analysis of run duration (**c**), average speed (**d**), step cycle (**e**) and paw stand (**f**). Bars represent median values and the interquartile range of the averages of three runs per animal. **g-i** Cognitive impairments were tested with novel object recognition test at P76. **g** Exemplary image of tracked movements of rats in the NOR setup. The white square represents the novel object, the white circle the old object. **h-i** Analysis of frequency (**h**) and time (**i**) discovering the novel object normalized to the total contact with both objects. Bars represent median values and the interquartile range. Males are indicated with squares; females are indicated with circles. N (Sham) = 5, N (HI/Veh; HI/Crid) = 12. Statistics: Kruskal-Wallis-test (p-values of ≤ 0.05).

3.4.5 Cortical microglial transcription altered due to HI and NLRP3 inhibition

To validate the cellular engagement of microglia cells in NLRP3 inhibition *in vivo*, microglia were isolated from the ipsilateral cortex following HI and analyzed for NLRP3 inhibition. Isolated cortical microglia from animals exposed to HI showed an increase in gene expression of caspase-1 and IL-1β. The NLRP3 cortical gene expression was not altered due to the treatments at the time point of 24 h after HI (figure 38). The transcription of the NLRP3 inflammasome effector caspase-1 was significantly elevated due to HI/Veh and HI/Crid treatment. However, the treatment with Crid3 diminished the increase due to HI (figure 38b). The downstream target IL-1β presented the same pattern with Crid3 partially preventing the non-significant increase in gene expression after HI (figure 38b). The purity of the isolated microglia was validated via FACS as shown in figure 38a.

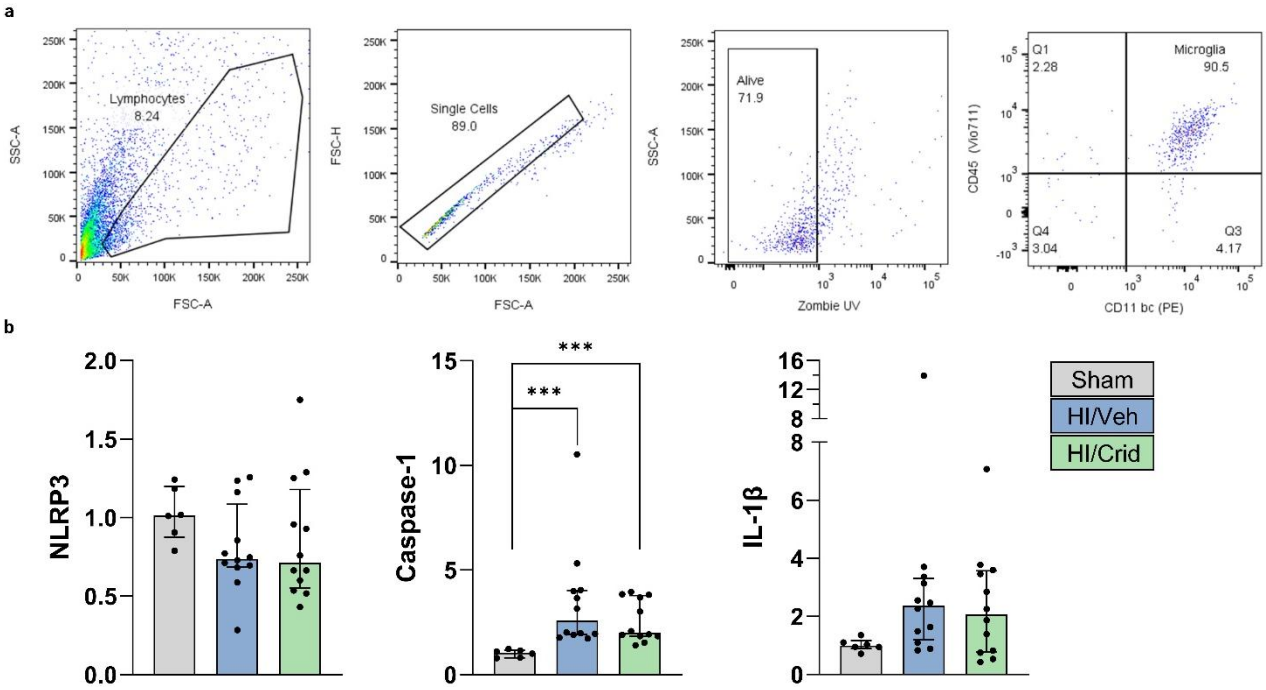

Figure 38: Microglial gene expression of NLRP3 pathway proteins after neonatal HIE. P7 Wistar rats underwent left common carotid artery ligation and subsequently hypoxia treatment for 90 min with one treatment group receiving NLRP3 inhibition via injecting 5 mg/kg Crid3 at 30 min before and 24 h after HI. 24 h after HI, microglia were isolated from the ipsilateral cortex. Treatment groups: Sham, HI/Vehicle and HI/Crid (5 mg/kg Crid3). **a** Flow cytometry gates used to determine microglia CD11b/c^{+}-CD45^{+} cells. **b** Microglia analysis via RT-PCR. Bars represent medians and the interquartile range of fold changes ($2^{-\Delta\Delta Ct}$). N (Sham) = 6, N (HI/Veh) = 12, N (HI/Crid) = 12. Statistics: Kruskal-Wallis-test (*** $p \leq 0.001$).

4. Discussion

This project aimed to characterize the role of the NLRP3 inflammasome in neonatal hypoxic–ischemic encephalopathy (HIE). HIE is a severe neonatal pathology associated with high mortality and long-term neurological disabilities, for which effective therapeutic strategies remain limited. Further investigation is therefore required, particularly to identify interventions targeting neuroinflammatory processes. The NLRP3 inflammasome emerged as a focus of this study due to its established involvement in inflammatory mechanisms following hypoxic–ischemic injury. To investigate NLRP3 activation and inhibition, this project specifically examined microglia in order to delineate their cell-specific contribution. As resident immune cells and key mediators of inflammation in the central nervous system, microglia were hypothesized to play a central role in the regulation of NLRP3 signaling in neonatal hypoxic–ischemic injury.

4.1 Time-dependent activation of NLRP3 after neonatal HIE

The involvement of the NLRP3 inflammasome following neonatal HIE was characterized by analyzing the protein expression of NLRP3 pathway proteins at different time points. Thereby, a time-dependent activation was found. Upstream pathway proteins were upregulated at earlier time points and downstream pathway proteins showed an increased expression at later time points after HI. Upstream pathway proteins were defined by their early role in the NLRP3 inflammasome activation prior to the complex oligomerization. Downstream pathway proteins were expressed after the complex activation and caspase-1 activity.

NLRP3 and pathway components were already shown upregulated at different time points after neonatal HI. In the ipsilateral hemisphere, Li et al. reported the activated NLRP3 inflammasome at the time points of 4 h, 8 h and 24 h after HI when analyzing protein expression (Li et al., 2021). Chen et al. could demonstrate NLRP3 pathway activation at 3 h, 6 h and 12 h post neonatal HI (Chen et al., 2023b). When focusing on specific brain regions, Lv et al. confirmed the cortical protein expression of NLRP3 pathway components at 12 h and 24 h after the insult, whereas Ystgaard et al. compared different brain regions with each other at the time point of 24 h and described the hippocampus with the highest

NLRP3 gene expression (Ystgaard et al., 2015; Lv et al., 2020). These studies proved the activation of the NLRP3 inflammasome after HI. Nonetheless, a clear temporal characterization of the pathway activation is necessary to comprehend the mechanism and to connect the published data describing the analysis of different time points after HI. Recently, a temporal overview of NLRP3 pathway activation was published by Lv et al. They analyzed protein expression at six different time points after neonatal HI in the ipsilateral hemisphere of the brain (3 h, 6 h, 12 h, 24 h, 48 h, 72 h). The results presented the time points of 24 h and 48 h as a peak showing the most upregulated protein expression compared to Sham (Lv et al., 2025). At 72 h after HI, the protein expression decreased again, showing the dominant activation being present before.

Focusing the analysis to the comparison between up- and downstream pathway proteins of NLRP3 inflammasome activation, the results from Lv et al. showed the upstream proteins being dominantly upregulated at 24 h and the downstream proteins demonstrating their highest protein increase at 48 h. This temporal differentiation between up- and downstream pathway proteins was likewise observable in the data presented in the current study. However, the time points showing the upregulated proteins differed, as well as the analyzed brain tissue. Whereas Lv et al. examined protein expression in tissue of the whole ipsilateral hemisphere (Lv et al., 2025), the current study differentiated between cortex, hippocampus and thalamus. This differentiation enhances the specificity of the analysis and consequently its results. Thereby, it was possible to identify the hippocampus and the cortex as brain regions with the most NLRP3 pathway activation.

The time points of 24 h and 48 h showed the most activation of the NLRP3 pathway in the brain regions and thereby confirmed the data by Lv et al. analyzing the brain hemisphere (Lv et al., 2025). The time point of 24 h post HI repeatedly showed NLRP3 upregulation in several publications and this study could validate it as an important time marker regarding NLRP3 pathway activation (Ystgaard et al., 2015; Lv et al., 2020; Li et al., 2021). Both time points, 24 h and 48 h after HI, correlate with the time window of the secondary energy failure following HI (Lorek et al., 1994; Vannucci et al., 2004). Characterized by excitatory, inflammatory and apoptotic mechanisms, the secondary energy failure phase matches the consequences of the NLRP3 inflammasome activation. This further emphasizes the need of NLRP3 regulation to prevent damage in the brain after HI.

The NLRP3 protein level was increased at 4 h, falling in the definition of the latent phase following HI (Lorek et al., 1994). As the general treatment window for HI is defined by 6 hours after onset (Sabir et al., 2012; Jia et al., 2018), this suggests the possible therapeutic intervention and prevention of inflammasome activation prior to the secondary energy failure.

Comparing the three different brain regions cortex, hippocampus and thalamus, it was clearly visible, that cortex and hippocampus presented more NLRP3 activation due to HI than the thalamus region. The thalamus region was previously shown to activate apoptosis-related pathways after HI injury (Northington et al., 2001). However, this study demonstrated that the pathway of NLRP3 inflammasome activation was not dominantly upregulated in this region. Thereby, the thalamus was less affected than cortex and hippocampus when analyzing the effect of NLRP3 activation. Validated later with MRI images showing brain damage occurring primarily in cortical and hippocampal areas, these results confirmed the thalamus as less affected area due to HI.

4.2 NLRP3 regulation in primary microglia after OGD

With the aim to translate the animal model of HI *in vitro*, the OGD experiment was established. Primary microglia were used to study the NLRP3 inflammasome *in vitro*, as they mediate the inflammatory response in the brain (Ni and Aschner, 2010; Stratoulias et al., 2019; Jiang et al., 2020a; Isik et al., 2023). Microglia are a major source of NLRP3 in the CNS (Ystgaard et al., 2015; Gong et al., 2018) and previous studies described the increased expression of microglial NLRP3 due to HI brain injury (Ystgaard et al., 2015; Serdar et al., 2020; Bernis et al., 2022) and inflammation-sensitized HI brain injury (Serdar et al., 2020; Bernis et al., 2022).

OGD affected the microglia by reducing their cell viability and inducing their activation. Further, the NLRP3 pathway activation was caused due to OGD. Analyzing different time points after OGD, a time-dependent induction of pathway protein transcription was found.

Other studies could also demonstrate a NLRP3 activation due to OGD in primary microglia and the microglia cell line BV2 (Gong et al., 2018; Ye et al., 2019; Ge et al., 2023). The reoxygenation time points of 12 h and 24 h after OGD were the most common used for studying NLRP3 protein expression and showing its upregulation (Gong et al., 2018; Ye

et al., 2019; Wu et al., 2023a). The increase at the time point of 12 h after OGD was verified within this study by analyzing the gene expression of NLRP3 pathway proteins.

Describing the importance of microglia when studying NLRP3, Gong et al. analyzed a coculture model of BV2 microglia and PC12 neurons in the OGD setup of 4 h OGD at 0 % O_2. Whereas microglia showed the peak of NLRP3 protein expression at 4 h and decreasing levels over 12 h to 24 h after OGD, neurons showed the opposite tendency with the peak of protein expression at 24 h after OGD (Gong et al., 2018). However, when analyzing neurons alone without microglia coculture, OGD did not induce an increase in NLRP3 expression (Gong et al., 2018), indicating early microglia activation being essential for stimulating the neurons at later time points. This emphasizes the important role of microglia in activating NLRP3 after OGD. Opposite to this publication, Chen et al. found NLRP3 upregulated due to OGD in primary neurons (Chen et al., 2023b), demonstrating NLRP3 being present and activated in neuronal cells as well.

To validate the NLRP3-specific activation in microglia, NLRP3 inhibition was conducted with the inhibitor Crid3. Crid3 intervenes with the activation of the inflammasome by binding to the central NACHT domain of the NLRP3 protein and preventing the transformation to the active state promoting the inflammasome formation (Hochheiser et al., 2022). The increase in gene expression levels due to OGD was prevented with NLRP3 inhibition. The impaired cell viability was rescued and the activity state, quantified by microglia phenotype, was shifted towards the resting state. These results confirmed the NLRP3-dependent activation of microglia and validated the upregulation of gene expression specific to NLRP3 pathway activation.
The beneficial effect of NLRP3 inhibition with Crid3 was previously presented in neurons, endothelial cells and myocytes (Bellut et al., 2021; Ding et al., 2023; Wu et al., 2023a). Crid3 rescued cell viability after OGD (Ding et al., 2023) and reduced the activation of the NLRP3 inflammasome, quantified by decreased expression of pathway components (Bellut et al., 2021; Ding et al., 2023; Wu et al., 2023a). This study validated these findings in primary microglia.

Inhibiting NLRP3 in primary microglia without another stress stimulus changed their activity by shifting the phenotype towards an activated state. Due to the need for a tight

regulation of the NLRP3 inflammasome (Mangan et al., 2018; Swanson et al., 2019; Paget et al., 2022; He et al., 2023), dysregulated immune response can be a consequence of NLRP3 inhibition. Other studies already showed the detrimental effects of NLRP3 deficiency. Following HI, mice lacking NLRP3 presented an increased brain infarct volume and a higher number of activated microglia (Ystgaard et al., 2019). Mice lacking NLRP3 in a cuprizone-induced demyelination and neuroinflammation model showed demyelination, oligodendrocyte loss and delayed neuroinflammation (Jha et al., 2010).
As OGD is activating NLRP3 and thereby potentially leading to its overactivation, NLRP3 inhibition can be beneficial to prevent uncontrolled inflammation. Without OGD, NLRP3 inhibition could lose its benefit and result in unintentional cell activation. This hypothesis was confirmed with the results showing the effect of OGD and control treatment plus NLRP3 inhibitor. Taken together, the presented data could underline the impact NLRP3 is having on microglia activation and their cell fate.

4.3 Activated microglia affect neurons in a NLRP3-dependent manner

To investigate the potential effect of OGD-activated microglial NLRP3 on neuronal cells, neurons were incubated with conditioned medium of microglia supernatant. Microglia release different molecules depending on their state of activation and function (Peferoen et al., 2015; Stratoulias et al., 2019; Isik et al., 2023). They are able to regulate neuronal functions as neurons express receptors on their surface, susceptible for the modulation of those secreted molecules (Bessis et al., 2007; Marinelli et al., 2019; Wang et al., 2023a). No coculturing was performed as the focus of this analysis laid on the effect microglia were having on neurons by secretion without the different cell types interacting with each other. Supernatant of CTR and OGD treated microglia with and without NLRP3 inhibition showed different outcomes on the fate of neurons. While activated microglial NLRP3 initiated inflammation and apoptosis by releasing pro-inflammatory factors, inhibition of NLRP3 could partially rescue these effects.
To validate the involvement of the microglial NLRP3 inflammasome leading to the release of factors influencing neurons, microglia cells and supernatant were analyzed. The upregulated expression of pathway proteins due to OGD and the released IL-1β in the supernatant were prevented by NLRP3 inhibition, confirming this hypothesis.

Microglia influencing the fate of neurons were already described in many articles (Wen et al., 2006; Bessis et al., 2007; Dai et al., 2015; Marinelli et al., 2019; Huang et al., 2022). Microglia were exposed to different treatments stimulating their activity and it was examined which effect their activation was having on molecular processes in neuronal cells.

One approach to activate microglia was treating them with LPS. Described by several publications, LPS-activated microglia supernatant affected neuronal cells by promoting their apoptosis and decreasing their cell viability (Wen et al., 2006; Dai et al., 2015; Huang et al., 2022). This highlighted the relevance of secreted molecules from LPS-activated processes in microglia.

Another approach to activate microglia was the treatment with OGD. Comparable with the present study, Liu et al. and Luan et al. showed the effect of OGD-activated microglia supernatant on neurons. Apoptosis was induced and the cell viability significantly reduced due to the treatment with the conditioned medium (Luan et al., 2020; Liu et al., 2022a). The longer the OGD treatment, the higher was the neuronal apoptotic rate (Luan et al., 2020). Consequently, microglia under OGD treatment released substances, potent to cause neuron damage.

Now, this study complemented the connection of OGD-activated microglia to the NLRP3 inflammasome and the impact of its activation and inhibition. The NLRP3 inflammasome was shown to promote the release of pro-inflammatory molecules in microglia, leading to neuronal cell damage. Inhibiting NLRP3 rescued the detrimental effects on apoptosis-inducing mechanisms in neurons.

Additional, to analyze the impact of NLRP3 activation in microglia on the induced apoptotic processes in the neurons, the supernatant was analyzed via mass spectrometry. Seven proteins, related to cytokine signaling in the immune system, were found increased when NLRP3 was activated. Two of these proteins were already connected to HI in previous studies, Tollip and Grb2.

Tollip was described significantly increased after ischemia/reperfusion experiments *in vivo* and due to OGD experiments *in vitro* (Li et al., 2015). Its knockout prevented brain damage by reducing the infarct size after ischemia and after myocardial infarct (Li et al., 2015; Wan et al., 2015). The beneficial effect of depleting Tollip could be explained by its characteristics of promoting neuronal apoptosis through Akt signaling and inflammatory

processes by inducing NF-κB activity (Li et al., 2015; Wan et al., 2015). Tollip has been shown to be negatively associated with NLRP3 expression. Acting through the transcription factor NF-κB, it suppresses NLRP3 activity (Roy et al., 2021; Zheng et al., 2021; Shen et al., 2025a). Nevertheless, the potential feedback loop of NLRP3 activity impacting Tollip expression remains unclear.

Grb2 was suggested as a diagnostic marker in ischemia as it showed enhanced expression due to ischemic injury (Jin et al., 2001; Zhang et al., 2020; Wang et al., 2024). It was already associated with promoting inflammatory signaling through NF-κB and apoptotic processes through Ras/MAPK (mitogen-activated protein kinase) signaling (Schlaepfer et al., 1994; Zhang et al., 2020; Lv et al., 2022). Grb2 has been shown to indirectly promote NLRP3 expression (Shen et al., 2025b). However, the opposite effect of NLRP3 activity on Grb2 expression has not been tested yet.

Both proteins were synthesized after NLRP3 activation and detected in the supernatant of microglia which induced apoptosis in neuronal cells. Their characteristic of promoting apoptosis and inflammation (Li et al., 2015; Wan et al., 2015; Zhang et al., 2020; Lv et al., 2022) validated the role of the NLRP3 inflammasome in damaging neurons. Taken together, microglial NLRP3 impacted neurons by the synthesis of pro-apoptotic proteins.

In vivo translated, these analyses outlined the potential impact of microglial NLRP3 activation on neuronal loss and brain damage after HI.

4.4 NLRP3 inhibition in the model of neonatal HIE

4.4.1 Efficiency of NLRP3 inhibition is time- and dose-dependent

When establishing the NLRP3 inhibition *in vivo*, different injection doses and schemes were tested. The efficiency of inhibition was analyzed by Western Blot of NLRP3 pathway proteins at 48 h after HI in the cortex, as this time point was previously shown to induce NLRP3 activation. The analysis of Western Blot was chosen to provide insight into biomolecular processes in the cortex and to prove that the inhibitor reached the brain after being i.p. injected. The characteristic of Crid3 crossing the BBB was already confirmed by a previous study (Chen et al., 2017).

The results showed a dose-dependent efficiency of NLRP3 inhibition. Comparing with other published studies describing the NLRP3 inhibition *in vivo* in models of ischemic

stroke, traumatic brain injury, HI-induced cerebral white matter damage or HI brain damage (Lv et al., 2020; Bellut et al., 2021; Ismael et al., 2021; Yang et al., 2023), they often show only one dose and injection scheme, making it difficult to comprehend the temporal action of the substance. One study already described a dose-dependency of Crid3 in a mouse MCAO model (Palomino-Antolin et al., 2022). The dose of 5 mg/kg injected at 30 min before and 24 h after HI, which was found the most effective in the case of the present study, did not correspond with any of the other published injection schemes of Crid3. This emphasizes the necessary differentiation and adjustment of NLRP3 inhibition in different animal models.

With the established injection scheme, the NLRP3 pathway proteins were analyzed at 24 h and 48 h after HI in the cortical and hippocampal ipsilateral areas of the brain. The time point of 24 h did already show NLRP3 pathway proteins upregulated in HI and MCAO models (Ystgaard et al., 2015; Jiang et al., 2020c; Li et al., 2021). 48 h was described by Lv et al. and confirmed by previous results of this study to show pathway activation (Lv et al., 2025). The results presented here did not only show the upregulated expression of NLRP3 pathway components due to HI, but also their inhibition due to the treatment with the specific NLRP3 inhibitor Crid3. Thereby, the present analysis confirmed the results of previous studies in which Crid3 had already been presented as an effective inhibitor of NLRP3 in different animal models (Krishnan et al., 2019; Chang et al., 2020; Jiang et al., 2020b; Lv et al., 2020; Bellut et al., 2021; Yan et al., 2021; Ding et al., 2023; Wu et al., 2023a; Placeres-Uray et al., 2025).

Comparing the two time points, NLRP3 protein levels increased from 24 h to 48 h, implying ongoing inflammation at this time. This trend was already observed in a previous study in isolated microglia after HI/Vehicle treatment (Bernis et al., 2022) and can be explained by ongoing inflammatory processes in the secondary energy failure following HI (Lorek et al., 1994).

There are studies describing NLRP3 expression in the cortex (Chen et al., 2019b; Liu et al., 2022b) and others presenting hippocampal analyses (Placeres-Uray et al., 2025). Nonetheless, only a few reports compare the brain regions with each other regarding NLRP3 expression and activation (Ystgaard et al., 2015). Ystgaard et al. demonstrated the hippocampus as the brain region with the highest gene expression of NLRP3 compared to cortex, thalamus, striatum and the subventricular zone (Ystgaard et al.,

2015). Opposite to this publication, the findings of the present study displayed NLRP3 protein levels being twenty times higher in the cortex compared to the hippocampus, suggesting an important role for the cortical region. As the analysis of protein expression is more reliable than gene expression analysis regarding the function of proteins, this resulted in a key role of the cortex in NLRP3 inflammasome activation in this HI animal model. Confirmed by studies, describing cortical expression of NLRP3 in response to (hypoxic-)ischemic injury (Serdar et al., 2019; Franke et al., 2021), the important role in regulating NLRP3 was emphasized.

4.4.2 Neuroprotective effect of NLRP3 inhibition

To assess the molecular analyses of NLRP3 activation to long-term effects in animals, brain damage was evaluated with MRI scans and behavior experiments were performed. Brain edema induced by HI was significantly rescued by inhibiting NLRP3 at both analyzed time points, P14 and P81. The beneficial effect of inhibiting NLRP3 in reducing brain infarct volume was already described in models of MCAO (Palomino-Antolin et al., 2022; Wu et al., 2023a), ischemic stroke (Bellut et al., 2021) and hypoxic-ischemic brain damage (Lv et al., 2020), where NLRP3 inhibition reduced brain infarct volume by 30-60 % (Lv et al., 2020; Bellut et al., 2021; Palomino-Antolin et al., 2022). Between the time points, there was no change in area loss due to HI, regardless of the brain development between P14 and P81. As the rat brain is still developing until 3 months after birth (Mengler et al., 2014), this study covered the time span of the developmental phase and presented the difference between early and late consequences after a HI insult in terms of edema size. The brain developed and grew during the three months, however, the edema size remained relatively constant. These results support the validity of early scans at P14 in assessing the consequences of HI brain injury regarding relative edema size.

Further, NLRP3 affected the development of motor impairments. HI impaired the motor skills by prolonging the run duration and step cycle in the Catwalk test. These effects were rescued with NLRP3 inhibition, suggesting the NLRP3 inflammasome activation supporting the impairment, described by slower movements during this assay.

Previous studies presented improved neurological functions in the MCAO model and in a spinal cord injury model when NLRP3 was inhibited. A reduction of the brain infarct volume was achieved at 24 h, 72 h and 7 days post injury and motor function was assessed via

forelimb grip strength and hind limb movement and improved when inhibiting NLRP3 (Jiao et al., 2020; Palomino-Antolin et al., 2022; Wu et al., 2023a).

By validating the beneficial effect of NLRP3 inhibition in HI on motor but not cognitive behavior skills, this study also enabled to connect the behavior assay to the biomolecular analyses. NLRP3 pathway proteins were inhibited at 24 h and 48 h after HI in the cortex and the hippocampus. The cortex expressed higher levels of the NLRP3 protein, which indicated a more important role for this area regarding inflammasome regulation.

The cortical brain region regulates movements (Georgopoulos et al., 1986) and the hippocampal region regulates memory foundation (Squire and Zola-Morgan, 1991), making these regions crucial for the performed behavior assays. The early protein expression corresponded to the long-term behavior when focusing on the indicated more relevant brain region cortex. The protein expression and the motor behavior were shifted towards the control and thereby the consequences of HI were reduced.

The long-term results are clearly demonstrating a neuroprotective effect of NLRP3 inhibition in HI brain injury. As one of many inflammasomes, NLRP3 stands out with the noticeable effect its inhibition is presenting on behavior and brain edema size. Its prominence in inflammatory pathways and the consequences in long-term outcomes is emphasizing the potential as therapeutic target regarding neuroprotection after HI.

4.5 HIE activates microglial NLRP3

By studying the microglial gene expression of NLRP3 pathway proteins after HIE, this study could confirm the involvement of microglia in regulating the inflammasome.

Microglia were isolated from the ipsilateral cortex at 24 h after HI because this brain region and this time point showed characteristics of NLRP3 inflammasome activation before. RT-PCR was performed to analyze NLRP3 activation specifically in microglia and FACS served to define the purity of the isolated cells.

Due to HI, NLRP3 associated genes were upregulated in cortical microglia. This upregulation was proven partially specific to NLRP3 activation with the use of the NLRP3 inhibitor Crid3, preventing a part of the increase in gene expression. This proved the inhibitor acting in microglia and further confirmed the importance of this cell type in

inflammasome activation and regulation as caspase-1 and IL-1β are specifically regulated by inflammasomes, particularly NLRP3 (Hornung et al., 2008).
The gene NLRP3 itself was not detected upregulated at 24 h after HI. This time point was already described inducing NLRP3 gene expression significantly in pre-sensitized inflammatory HI, while only a non-significant increase was observed in HI models without sensitization (Serdar et al., 2020; Bernis et al., 2022). The cortical brain region presents edema in the brain already early after HI (Xiao et al., 2014), indicating current inflammation. Thereby, the NLRP3 inflammasome could be activated earlier than the studied 24 h time point at gene expression level. As only one time point was analyzed, another time point analysis would be crucial to study the mechanism behind NLRP3 activation in microglia after HI.

Several studies have reported that microglia are key regulators of NLRP3 inflammasome activation in the central nervous system, highlighting their critical contribution to inflammatory signaling following hypoxic–ischemic injury. When comparing primary mouse microglia to astrocytes regarding gene expression of NLRP3, ASC and caspase-1, Gustin et al. showed unambiguous results. Microglia expressed the particular genes of the inflammasome pathway, whereas equally stimulated astrocytes did not (Gustin et al., 2015). These results indicated the NLRP3 inflammasome playing a role in activated microglia cells due to LPS and combined cytokine treatment, whereas the same stimuli did not lead to a functional NLRP3 inflammasome in astrocytes. In another study, neurons of the cell line PC12 were shown to upregulate the NLRP3, ASC and caspase-1 protein expression due to OGD only when they were cocultured with microglia and not isolated, whereas microglia expressed the proteins in both culture conditions (Gong et al., 2018).
This specific activation of the NLRP3 inflammasome in microglia could have several reasons. Microglia are the major responders to inflammation compared to astrocytes and neurons (Goshi et al., 2020). They represent a main source of activated NLRP3 early after ischemic injury (Gong et al., 2018) and they were already reported essential for NLRP3 activation in a peripheral inflammation-induced BBB disruption model (Yoon et al., 2025).

All of these studies suggested an important role for microglial cells in NLRP3 inflammasome activation. This study investigated the cell-specific NLRP3 activation at 24 h after HIE and highlighted the treatment with the NLRP3 inhibitor Crid3 reaching

microglia cells by inhibiting gene expression. As promising target for therapies intervening with cell damage following HI, microglia need to be further studied to reveal their potential as regulators of NLRP3 inflammasome activity.

4.6 NLRP3 inhibition as potential therapeutic target

The aim of this study was not only to gain insight into the mechanism of NLRP3 inflammasome activation after HI but also to provide a characterization of the potential therapeutic target NLRP3. Its regulation could be used translational to treat HIE in humans.

This study describes the inhibition of the inflammasome as neuroprotective in the Rice-Vannucci rat model. Brain edema was reduced due to NLRP3 inhibition and behavioral impairments were prevented. This beneficial outcome is promising regarding translational therapies. Nonetheless, the compound used for this mechanistic study, Crid3, cannot be applied in humans. During a phase II clinical trial, Crid3 induced liver toxicity and thereby was excluded for further clinical application (Li et al., 2022).

Since then, the research for replacing NLRP3 inhibitors is ongoing and recently, Wilhelmsen et al. described a novel small-molecule inhibitor which specifically inhibited primate NLRP3. BAL-0028 has a high binding affinity to NLRP3 and is more potent than Crid3 with a different mechanism of action (Wilhelmsen et al., 2025). This finding represents a promising outlook for further research in NLRP3 inhibition regarding translation in the clinic. The utilization of other NLRP3 inhibitors could achieve the same beneficial outcomes after HI insults as the present study described for Crid3. The regulation of NLRP3 was shown promising in this study and has to be further investigated to provide clinical value.

The second limitation of this study preventing it from being used as a template for clinical applications is the time point of treatment injection. The first injection was applied at 30 min before HI, representing an obstacle in the clinic because there will not be a treatment induced before the damage can be diagnosed.

Despite the limitations for direct translation, the statement of this study is still relevant for therapies when focusing on the beneficial effects of NLRP3 inhibition in the animal model.

Further, this study provides insight, that an isolated inhibition of NLRP3 could be neuroprotective but will not reach the same levels as healthy patients. A combination with another treatment, inhibiting another pathway of inflammation in the brain could be promising in finding the most efficient therapy for HIE.

In a model of acute lung injury, Wang et al. could demonstrate a benefit of treating the animals with Crid3 combined with anakinra, a recombinant IL-1 receptor antagonist protein with anti-inflammatory effects. The combinatory treatment improved the therapeutic effect in acute lung injury and reduced NLRP3 pathway activation at gene and protein level more than both compounds alone (Wang et al., 2021). Another study by Chen et al. used the combinatory treatment of Crid3 and Rapamycin in traumatic brain injury. Rapamycin is an inhibitor of mTOR (mechanistic target of rapamycin) and increases autophagy. The combined effect of Crid3 and Rapamycin provided better neuroprotection than both treatments alone (Chen et al., 2019b). These articles demonstrated the potential benefit of a combined treatment with Crid3.

The performed study demonstrated the involvement of microglia in NLRP3 inflammasome activation. Consequently, another future direction to research NLRP3 regulation in HIE could be a cell-specific approach aiming microglial NLRP3. The method of applying nanoparticles aiming microglia and loaded with a compound inhibiting NLRP3 could be suitable to cell-specifically inhibit NLRP3.

Nanoparticles targeting microglia were already shown to enable regulation of inflammation in the brain. Loaded with small interfering RNA (siRNA) as described by Wu et al. in the model of Parkinson’s disease or loaded with a stimulator of interferon genes (STING) inhibitor in the model of ischemic stroke reported by Zhang et al., the nanoparticles shifted the phenotype of microglia towards an anti-inflammatory state and reduced inflammation in the brain (Wu et al., 2023b; Zhang et al., 2025). Aiming for NLRP3 and NF-κB inhibition, Wahl et al. published a method using nanoligomers in a model of aging, which resulted in decreased inflammation and improved cognitive behavior (Wahl et al., 2024). Combining the approaches of inhibiting NLRP3 and targeting microglia, a cell-specific treatment could be designed. Whether it is more beneficial to inhibit NLRP3 specifically in microglia or across different cell types, needs further investigation.

The present model demonstrated the benefit of NLRP3 inflammasome inhibition on HIE consequences. Further experiments are necessary to find a suitable protocol that can be transferred to preclinical studies.

4.7 Limitations

This study outlined the importance of the NLRP3 inflammasome in the model of neonatal HIE with a specific focus on microglial NLRP3. Despite the many mutually confirming analyses, there are some limitations within this study.

When comparing biomolecular analyses and behavior experiments, the time points analyzed were not identical. To achieve a comparison at the same developmental stage of the rats' brains, protein expression analyses would need to be redone at the same time point the behavior assays were performed. Limited by the brains structure at this late time point, which hinders to distinguish between the different brain areas due to the HI-induced damage, this assessment would not be feasible.

The use of the NLRP3 inhibitor Crid3 represents a limitation of this study. As Crid3 was shown to induce liver toxicity during a phase II clinical trial (Li et al., 2022), this property of Crid3 prevents it from being applied translationally as a treatment. However, because of its high specificity, Crid3 still represents a suitable NLRP3 inhibitor for mechanistic studies and thereby was used in this study.

Another limitation is the missing analysis of the Crid3 effect in the animal model without HI. The group Sham+Crid3 was not included in this study because of the experiments previously performed *in vitro*. The *in vitro* results did not show any effect of Crid3 treatment on cell viability of primary microglia and neurons treated with microglia supernatant. Neuronal inflammation and apoptosis markers were not upregulated due to the Crid3 treatment, indicating no effect of the substance on neuronal damage.

4.8 Conclusion

This study aimed to characterize the NLRP3 inflammasome in the context of neonatal HIE. Starting with investigating the activation of the NLRP3 inflammasome due to HI *in vivo,* the relevance of this topic was presented. NLRP3 was upregulated after HI, and after

establishing primary microglia cell culture with OGD experiments mimicking HI, the same trend was observed. Microglia were shown to be one of the drivers of NLRP3 activation following HI, validated with the microglia isolation; and they were proven to induce neuronal damage in a NLRP3-dependent way. The inhibition of NLRP3 confirmed the hypothesis that NLRP3 increased inflammation in the brain, potentially leading to neuronal cell loss and brain damage. Additionally, neuroprotection was observed in long-term assays when NLRP3 was inhibited.

Taken together, this study characterized the NLRP3 inflammasome to be activated in neonatal HIE, specifically in microglia, and demonstrated the benefit of NLRP3 inhibition in neuroprotection after HI and thereby providing a potential therapeutic target.

5. Abstract

Worldwide, neonates are suffering from hypoxic-ischemic encephalopathy. The pathology can lead to neurological impairments and neonatal death and has an incidence of 1-3/1000 neonates in developed countries and 10-20 times as many in developing countries. Inflammation in the brain is one of the factors deciding the severity of disease progression.

The NLRP3 inflammasome senses and reacts to stress signals and is known to be activated following hypoxia-ischemia. However, the detailed mechanism of the NLRP3 regulation after hypoxia-ischemia and the cell-specific involvement needs further investigation.

As microglia are dominantly mediating inflammation in the brain and are known to express NLRP3, this study investigated the role of microglial cells in NLRP3 activation following hypoxia-ischemia.

The role of NLRP3 in hypoxic-ischemic encephalopathy was characterized by using the hypoxia-ischemia model after Rice and Vannucci in the neonatal rat and establishing an oxygen-glucose deprivation model in primary microglia.

This study presents the relevance of the NLRP3 activation following hypoxia-ischemia. Furthermore, the study demonstrates the beneficial effect of inhibiting NLRP3 on biomolecular level and on long-term outcomes in the animal. Microglia were presented as major drivers of NLRP3 regulation following hypoxia-ischemia. With the focus on microglial NLRP3, it was shown how activated NLRP3 is impacting the fate of neuronal cells. These results provide insight into the mechanisms of NLRP3 regulation and present a potential cell-specific target for therapeutic interventions.

6. List of figures

7. List of tables

8. References

Accogli, T., C. Hibos, and F. Vegran. 2023. Canonical and non-canonical functions of NLRP3. J Adv Res 53:137-151. doi: 10.1016/j.jare.2023.01.001

Adrian, M., M. Weber, M. C. Tsai, C. Glock, O. I. Kahn, L. Phu, T. K. Cheung, W. J. Meilandt, C. M. Rose, and C. C. Hoogenraad. 2023. Polarized microtubule remodeling transforms the morphology of reactive microglia and drives cytokine release. Nat Commun 14(1):6322. doi: 10.1038/s41467-023-41891-6

Ajami, B., J. L. Bennett, C. Krieger, W. Tetzlaff, and F. M. Rossi. 2007. Local self-renewal can sustain CNS microglia maintenance and function throughout adult life. Nat Neurosci 10(12):1538-1543. doi: 10.1038/nn2014

Akbal, A., A. Dernst, M. Lovotti, M. S. J. Mangan, R. M. McManus, and E. Latz. 2022. How location and cellular signaling combine to activate the NLRP3 inflammasome. Cell Mol Immunol 19(11):1201-1214. doi: 10.1038/s41423-022-00922-w

Askew, K., K. Li, A. Olmos-Alonso, F. Garcia-Moreno, Y. Liang, P. Richardson, T. Tipton, M. A. Chapman, K. Riecken, S. Beccari, A. Sierra, Z. Molnár, M. S. Cragg, O. Garaschuk, V. H. Perry, and D. Gomez-Nicola. 2017. Coupled Proliferation and Apoptosis Maintain the Rapid Turnover of Microglia in the Adult Brain. Cell Rep 18(2):391-405. doi: 10.1016/j.celrep.2016.12.041

Bellut, M., L. Papp, M. Bieber, P. Kraft, G. Stoll, and M. K. Schuhmann. 2021. NLPR3 inflammasome inhibition alleviates hypoxic endothelial cell death in vitro and protects blood-brain barrier integrity in murine stroke. Cell Death Dis 13(1):20. doi: 10.1038/s41419-021-04379-z

Bergsbaken, T., S. L. Fink, and B. T. Cookson. 2009. Pyroptosis: host cell death and inflammation. Nat Rev Microbiol 7(2):99-109. doi: 10.1038/nrmicro2070

Bernis, M. E., Y. Schleehuber, M. Zweyer, E. Maes, U. Felderhoff-Müser, D. Picard, and H. Sabir. 2022. Temporal Characterization of Microglia-Associated Pro- and Anti-Inflammatory Genes in a Neonatal Inflammation-Sensitized Hypoxic-Ischemic Brain Injury Model. Oxid Med Cell Longev 2022:2479626. doi: 10.1155/2022/2479626

Bessis, A., C. Béchade, D. Bernard, and A. Roumier. 2007. Microglial control of neuronal death and synaptic properties. Glia 55(3):233-238. doi: 10.1002/glia.20459

Beyer, M. M. S., N. Lonnemann, A. Remus, E. Latz, M. T. Heneka, and M. Korte. 2020. Enduring Changes in Neuronal Function upon Systemic Inflammation Are NLRP3 Inflammasome Dependent. J Neurosci 40(28):5480-5494. doi: 10.1523/jneurosci.0200-20.2020

Biber, K., H. Neumann, K. Inoue, and H. W. Boddeke. 2007. Neuronal 'On' and 'Off' signals control microglia. Trends Neurosci 30(11):596-602. doi: 10.1016/j.tins.2007.08.007

Blevins, H. M., Y. Xu, S. Biby, and S. Zhang. 2022. The NLRP3 Inflammasome Pathway: A Review of Mechanisms and Inhibitors for the Treatment of Inflammatory Diseases. Front Aging Neurosci 14:879021. doi: 10.3389/fnagi.2022.879021

Booshehri, L. M., and H. M. Hoffman. 2019. CAPS and NLRP3. J Clin Immunol 39(3):277-286. doi: 10.1007/s10875-019-00638-z

Borst, K., A. A. Dumas, and M. Prinz. 2021. Microglia: Immune and non-immune functions. Immunity 54(10):2194-2208. doi: 10.1016/j.immuni.2021.09.014

Borteçen, T., T. Müller, and J. Krijgsveld. 2023. An integrated workflow for quantitative analysis of the newly synthesized proteome. Nature Communications 14(1):8237. doi: 10.1038/s41467-023-43919-3

Boxer, M. B., A. M. Quinn, M. Shen, A. Jadhav, W. Leister, A. Simeonov, D. S. Auld, and C. J. Thomas. 2010. A highly potent and selective caspase 1 inhibitor that utilizes a key 3-cyanopropanoic acid moiety. ChemMedChem 5(5):730-738. doi: 10.1002/cmdc.200900531

Chang, Y., J. Zhu, D. Wang, H. Li, Y. He, K. Liu, X. Wang, Y. Peng, S. Pan, and K. Huang. 2020. NLRP3 inflammasome-mediated microglial pyroptosis is critically involved in the development of post-cardiac arrest brain injury. J Neuroinflammation 17(1):219. doi: 10.1186/s12974-020-01879-1

Chen, L., Y. Zeng, B. Ren, X. Wang, F. Zhao, J. Du, R. Zhang, and J. Deng. 2023a. ALDOC regulated the biological function and immune infiltration of gastric cancer cells. Int J Biochem Cell Biol 158:106407. doi: 10.1016/j.biocel.2023.106407

Chen, W., S. S. Foo, A. Zaid, T. S. Teng, L. J. Herrero, S. Wolf, K. Tharmarajah, L. D. Vu, C. van Vreden, A. Taylor, J. R. Freitas, R. W. Li, T. M. Woodruff, R. Gordon, D. M. Ojcius, H. I. Nakaya, T. D. Kanneganti, L. A. J. O'Neill, A. A. B. Robertson, N. J. King, A. Suhrbier, M. A. Cooper, L. F. P. Ng, and S. Mahalingam. 2017. Specific inhibition of NLRP3 in chikungunya disease reveals a role for inflammasomes in alphavirus-induced inflammation. Nat Microbiol 2(10):1435-1445. doi: 10.1038/s41564-017-0015-4

Chen, Y., X. Li, Q. Xiong, Y. Du, M. Luo, L. Yi, Y. Pang, X. Shi, Y. T. Wang, and Z. Dong. 2023b. Inhibiting NLRP3 inflammasome signaling pathway promotes neurological recovery following hypoxic-ischemic brain damage by increasing p97-mediated surface GluA1-containing AMPA receptors. J Transl Med 21(1):567. doi: 10.1186/s12967-023-04452-5

Chen, Y., J. Meng, F. Bi, H. Li, C. Chang, C. Ji, and W. Liu. 2019a. EK7 Regulates NLRP3 Inflammasome Activation and Neuroinflammation Post-traumatic Brain Injury. Front Mol Neurosci 12:202. doi: 10.3389/fnmol.2019.00202

Chen, Y., J. Meng, Q. Xu, T. Long, F. Bi, C. Chang, and W. Liu. 2019b. Rapamycin improves the neuroprotection effect of inhibition of NLRP3 inflammasome activation after TBI. Brain Res 1710:163-172. doi: 10.1016/j.brainres.2019.01.005

Coll, R. C., J. R. Hill, C. J. Day, A. Zamoshnikova, D. Boucher, N. L. Massey, J. L. Chitty, J. A. Fraser, M. P. Jennings, A. A. B. Robertson, and K. Schroder. 2019. MCC950 directly targets the NLRP3 ATP-hydrolysis motif for inflammasome inhibition. Nat Chem Biol 15(6):556-559. doi: 10.1038/s41589-019-0277-7

Coll, R. C., A. A. Robertson, J. J. Chae, S. C. Higgins, R. Muñoz-Planillo, M. C. Inserra, I. Vetter, L. S. Dungan, B. G. Monks, A. Stutz, D. E. Croker, M. S. Butler, M.

Haneklaus, C. E. Sutton, G. Núñez, E. Latz, D. L. Kastner, K. H. Mills, S. L. Masters, K. Schroder, M. A. Cooper, and L. A. O'Neill. 2015. A small-molecule inhibitor of the NLRP3 inflammasome for the treatment of inflammatory diseases. Nat Med 21(3):248-255. doi: 10.1038/nm.3806

Dai, X. J., N. Li, L. Yu, Z. Y. Chen, R. Hua, X. Qin, and Y. M. Zhang. 2015. Activation of BV2 microglia by lipopolysaccharide triggers an inflammatory reaction in PC12 cell apoptosis through a toll-like receptor 4-dependent pathway. Cell Stress Chaperones 20(2):321-331. doi: 10.1007/s12192-014-0552-1

Danladi, J., and H. Sabir. 2021. Perinatal Infection: A Major Contributor to Efficacy of Cooling in Newborns Following Birth Asphyxia. Int J Mol Sci 22(2)doi: 10.3390/ijms22020707

Das, B., C. Sarkar, V. S. Rawat, D. Kalita, S. Deka, and A. Agnihotri. 2021. Promise of the NLRP3 Inflammasome Inhibitors in In Vivo Disease Models. Molecules 26(16)doi: 10.3390/molecules26164996

Demarest, T. G., R. A. Schuh, J. Waddell, M. C. McKenna, and G. Fiskum. 2016. Sex-dependent mitochondrial respiratory impairment and oxidative stress in a rat model of neonatal hypoxic-ischemic encephalopathy. J Neurochem 137(5):714-729. doi: 10.1111/jnc.13590

Dempsey, C., A. Rubio Araiz, K. J. Bryson, O. Finucane, C. Larkin, E. L. Mills, A. A. B. Robertson, M. A. Cooper, L. A. J. O'Neill, and M. A. Lynch. 2017. Inhibiting the NLRP3 inflammasome with MCC950 promotes non-phlogistic clearance of amyloid-β and cognitive function in APP/PS1 mice. Brain Behav Immun 61:306-316. doi: 10.1016/j.bbi.2016.12.014

Dick, M. S., L. Sborgi, S. Rühl, S. Hiller, and P. Broz. 2016. ASC filament formation serves as a signal amplification mechanism for inflammasomes. Nature Communications 7(1):11929. doi: 10.1038/ncomms11929

Ding, H. S., Y. Huang, J. F. Qu, Y. J. Wang, Z. Y. Huang, F. Y. Wang, W. J. Yi, and X. X. Liu. 2023. Panaxynol ameliorates cardiac ischemia/reperfusion injury by suppressing NLRP3-induced pyroptosis and apoptosis via HMGB1/TLR4/NF-κB axis. Int Immunopharmacol 121:110222. doi: 10.1016/j.intimp.2023.110222

Ding, J., K. Wang, W. Liu, Y. She, Q. Sun, J. Shi, H. Sun, D.-C. Wang, and F. Shao. 2016. Pore-forming activity and structural autoinhibition of the gasdermin family. Nature 535(7610):111-116. doi: 10.1038/nature18590

Downs, K. P., H. Nguyen, A. Dorfleutner, and C. Stehlik. 2020. An overview of the non-canonical inflammasome. Mol Aspects Med 76:100924. doi: 10.1016/j.mam.2020.100924

Ehlting, A., M. Zweyer, E. Maes, Y. Schleehuber, H. Doshi, H. Sabir, and M. E. Bernis. 2022. Impact of Hypoxia-Ischemia on Neurogenesis and Structural and Functional Outcomes in a Mild-Moderate Neonatal Hypoxia-Ischemia Brain Injury Model. Life (Basel) 12(8)doi: 10.3390/life12081164

Falck, M., D. Osredkar, E. Maes, T. Flatebø, T. R. Wood, H. Sabir, and M. Thoresen. 2017. Hypothermic Neuronal Rescue from Infection-Sensitised Hypoxic-Ischaemic

Brain Injury Is Pathogen Dependent. Dev Neurosci 39(1-4):238-247. doi: 10.1159/000455838

Franke, M., M. Bieber, P. Kraft, A. N. R. Weber, G. Stoll, and M. K. Schuhmann. 2021. The NLRP3 inflammasome drives inflammation in ischemia/reperfusion injury after transient middle cerebral artery occlusion in mice. Brain Behav Immun 92:223-233. doi: 10.1016/j.bbi.2020.12.009

Ge, P., H. Duan, C. Tao, S. Niu, Y. Hu, R. Duan, A. Shen, Y. Sun, and W. Sun. 2023. TMAO Promotes NLRP3 Inflammasome Activation of Microglia Aggravating Neurological Injury in Ischemic Stroke Through FTO/IGF2BP2. J Inflamm Res 16:3699-3714. doi: 10.2147/jir.S399480

Georgopoulos, A. P., A. B. Schwartz, and R. E. Kettner. 1986. Neuronal population coding of movement direction. Science 233(4771):1416-1419. doi: 10.1126/science.3749885

Ginhoux, F., M. Greter, M. Leboeuf, S. Nandi, P. See, S. Gokhan, M. F. Mehler, S. J. Conway, L. G. Ng, E. R. Stanley, I. M. Samokhvalov, and M. Merad. 2010. Fate mapping analysis reveals that adult microglia derive from primitive macrophages. Science 330(6005):841-845. doi: 10.1126/science.1194637

Gong, Z., J. Pan, Q. Shen, M. Li, and Y. Peng. 2018. Mitochondrial dysfunction induces NLRP3 inflammasome activation during cerebral ischemia/reperfusion injury. J Neuroinflammation 15(1):242. doi: 10.1186/s12974-018-1282-6

Goshi, N., R. K. Morgan, P. J. Lein, and E. Seker. 2020. A primary neural cell culture model to study neuron, astrocyte, and microglia interactions in neuroinflammation. J Neuroinflammation 17(1):155. doi: 10.1186/s12974-020-01819-z

Guo, M. L., E. T. Chivero, S. E. Callen, and S. Buch. 2021. NLRP3 Inflammasome Is Involved in Cocaine-Mediated Potentiation on Behavioral Changes in CX3CR1-Deficient Mice. J Pers Med 11(10)doi: 10.3390/jpm11100963

Gustin, A., M. Kirchmeyer, E. Koncina, P. Felten, S. Losciuto, T. Heurtaux, A. Tardivel, P. Heuschling, and C. Dostert. 2015. NLRP3 Inflammasome Is Expressed and Functional in Mouse Brain Microglia but Not in Astrocytes. PLoS One 10(6):e0130624. doi: 10.1371/journal.pone.0130624

He, W., Z. Hu, Y. Zhong, C. Wu, and J. Li. 2023. The Potential of NLRP3 Inflammasome as a Therapeutic Target in Neurological Diseases. Mol Neurobiol 60(5):2520-2538. doi: 10.1007/s12035-023-03229-7

Hellström Erkenstam, N., P. L. Smith, B. Fleiss, S. Nair, P. Svedin, W. Wang, M. Boström, P. Gressens, H. Hagberg, K. L. Brown, K. Sävman, and C. Mallard. 2016. Temporal Characterization of Microglia/Macrophage Phenotypes in a Mouse Model of Neonatal Hypoxic-Ischemic Brain Injury. Front Cell Neurosci 10:286. doi: 10.3389/fncel.2016.00286

Hochheiser, I. V., M. Pilsl, G. Hagelueken, J. Moecking, M. Marleaux, R. Brinkschulte, E. Latz, C. Engel, and M. Geyer. 2022. Structure of the NLRP3 decamer bound to the cytokine release inhibitor CRID3. Nature 604(7904):184-189. doi: 10.1038/s41586-022-04467-w

Hornung, V., F. Bauernfeind, A. Halle, E. O. Samstad, H. Kono, K. L. Rock, K. A. Fitzgerald, and E. Latz. 2008. Silica crystals and aluminum salts activate the NALP3 inflammasome through phagosomal destabilization. Nat Immunol 9(8):847-856. doi: 10.1038/ni.1631

Hou, B., J. Yin, S. Liu, J. Guo, B. Zhang, Z. Zhang, L. Yang, X. Tan, Y. Long, S. Feng, J. Zhou, Y. Wu, X. Wang, S. Han, Z. Wang, and X. He. 2024. Inhibiting the NLRP3 Inflammasome with MCC950 Alleviates Neurological Impairment in the Brain of EAE Mice. Mol Neurobiol 61(3):1318-1330. doi: 10.1007/s12035-023-03618-y

Hu, J. J., X. Liu, S. Xia, Z. Zhang, Y. Zhang, J. Zhao, J. Ruan, X. Luo, X. Lou, Y. Bai, J. Wang, L. R. Hollingsworth, V. G. Magupalli, L. Zhao, H. R. Luo, J. Kim, J. Lieberman, and H. Wu. 2020. FDA-approved disulfiram inhibits pyroptosis by blocking gasdermin D pore formation. Nat Immunol 21(7):736-745. doi: 10.1038/s41590-020-0669-6

Huang, Y., Q. Cai, H. Liu, Y. Wang, and W. Ma. 2022. Remifentanil inhibits the inflammatory response of BV2 microglia and protects PC12 cells from damage caused by microglia activation. Bioengineered 13(5):13944-13955. doi: 10.1080/21655979.2022.2080421

Isik, S., B. Yeman Kiyak, R. Akbayir, R. Seyhali, and T. Arpaci. 2023. Microglia Mediated Neuroinflammation in Parkinson's Disease. Cells 12(7)doi: 10.3390/cells12071012

Ismael, S., H. A. Ahmed, T. Adris, K. Parveen, P. Thakor, and T. Ishrat. 2021. The NLRP3 inflammasome: a potential therapeutic target for traumatic brain injury. Neural Regen Res 16(1):49-57. doi: 10.4103/1673-5374.286951

Jha, S., S. Y. Srivastava, W. J. Brickey, H. Iocca, A. Toews, J. P. Morrison, V. S. Chen, D. Gris, G. K. Matsushima, and J. P. Ting. 2010. The inflammasome sensor, NLRP3, regulates CNS inflammation and demyelination via caspase-1 and interleukin-18. J Neurosci 30(47):15811-15820. doi: 10.1523/jneurosci.4088-10.2010

Jia, W., X. Lei, W. Dong, and Q. Li. 2018. Benefits of starting hypothermia treatment within 6 h vs. 6-12 h in newborns with moderate neonatal hypoxic-ischemic encephalopathy. BMC Pediatr 18(1):50. doi: 10.1186/s12887-018-1013-2

Jiang, C. T., W. F. Wu, Y. H. Deng, and J. W. Ge. 2020a. Modulators of microglia activation and polarization in ischemic stroke (Review). Mol Med Rep 21(5):2006-2018. doi: 10.3892/mmr.2020.11003

Jiang, H., H. He, Y. Chen, W. Huang, J. Cheng, J. Ye, A. Wang, J. Tao, C. Wang, Q. Liu, T. Jin, W. Jiang, X. Deng, and R. Zhou. 2017. Identification of a selective and direct NLRP3 inhibitor to treat inflammatory disorders. J Exp Med 214(11):3219-3238. doi: 10.1084/jem.20171419

Jiang, M., R. Li, J. Lyu, X. Li, W. Wang, Z. Wang, H. Sheng, W. Zhang, J. Karhausen, and W. Yang. 2020b. MCC950, a selective NLPR3 inflammasome inhibitor, improves neurologic function and survival after cardiac arrest and resuscitation. J Neuroinflammation 17(1):256. doi: 10.1186/s12974-020-01933-y

Jiang, Q., X. Geng, J. Warren, E. Eugene Paul Cosky, S. Kaura, C. Stone, F. Li, and Y. Ding. 2020c. Hypoxia Inducible Factor-1α (HIF-1α) Mediates NLRP3 Inflammasome-Dependent-Pyroptotic and Apoptotic Cell Death Following Ischemic Stroke. Neuroscience 448:126-139. doi: 10.1016/j.neuroscience.2020.09.036

Jiao, J., G. Zhao, Y. Wang, P. Ren, and M. Wu. 2020. MCC950, a Selective Inhibitor of NLRP3 Inflammasome, Reduces the Inflammatory Response and Improves Neurological Outcomes in Mice Model of Spinal Cord Injury. Front Mol Biosci 7:37. doi: 10.3389/fmolb.2020.00037

Jin, K., X. O. Mao, M. W. Eshoo, T. Nagayama, M. Minami, R. P. Simon, and D. A. Greenberg. 2001. Microarray analysis of hippocampal gene expression in global cerebral ischemia. Ann Neurol 50(1):93-103. doi: 10.1002/ana.1073

Kaufmann, B., A. Leszczynska, A. Reca, L. M. Booshehri, J. Onyuru, Z. Tan, A. Wree, H. Friess, D. Hartmann, B. Papouchado, L. Broderick, H. M. Hoffman, B. A. Croker, Y. P. Zhu, and A. E. Feldstein. 2022. NLRP3 activation in neutrophils induces lethal autoinflammation, liver inflammation, and fibrosis. EMBO reports 23(11)doi: 10.15252/embr.202154446

Kelley, N., D. Jeltema, Y. Duan, and Y. He. 2019. The NLRP3 Inflammasome: An Overview of Mechanisms of Activation and Regulation. Int J Mol Sci 20(13)doi: 10.3390/ijms20133328

Krishnan, S. M., Y. H. Ling, B. M. Huuskes, D. M. Ferens, N. Saini, C. T. Chan, H. Diep, M. M. Kett, C. S. Samuel, B. K. Kemp-Harper, A. A. B. Robertson, M. A. Cooper, K. Peter, E. Latz, A. S. Mansell, C. G. Sobey, G. R. Drummond, and A. Vinh. 2019. Pharmacological inhibition of the NLRP3 inflammasome reduces blood pressure, renal damage, and dysfunction in salt-sensitive hypertension. Cardiovasc Res 115(4):776-787. doi: 10.1093/cvr/cvy252

Kurinczuk, J. J., M. White-Koning, and N. Badawi. 2010. Epidemiology of neonatal encephalopathy and hypoxic-ischaemic encephalopathy. Early Hum Dev 86(6):329-338. doi: 10.1016/j.earlhumdev.2010.05.010

Lee, A. C., N. Kozuki, H. Blencowe, T. Vos, A. Bahalim, G. L. Darmstadt, S. Niermeyer, M. Ellis, N. J. Robertson, S. Cousens, and J. E. Lawn. 2013. Intrapartum-related neonatal encephalopathy incidence and impairment at regional and global levels for 2010 with trends from 1990. Pediatr Res 74 Suppl 1(Suppl 1):50-72. doi: 10.1038/pr.2013.206

Leu, S. Y., Y. L. Tsang, L. C. Ho, C. C. Yang, A. N. Shao, C. Y. Chang, H. K. Lin, P. J. Tsai, J. M. Sung, and Y. S. Tsai. 2023. NLRP3 inflammasome activation, metabolic danger signals, and protein binding partners. J Endocrinol 257(2)doi: 10.1530/joe-22-0184

Li, H., Y. Guan, B. Liang, P. Ding, X. Hou, W. Wei, and Y. Ma. 2022. Therapeutic potential of MCC950, a specific inhibitor of NLRP3 inflammasome. Eur J Pharmacol 928:175091. doi: 10.1016/j.ejphar.2022.175091

Li, M., B. Feng, L. Wang, S. Guo, P. Zhang, J. Gong, Y. Zhang, A. Zheng, and H. Li. 2015. Tollip is a critical mediator of cerebral ischaemia-reperfusion injury. J Pathol 237(2):249-262. doi: 10.1002/path.4565

Li, N., C. Liu, C. Wang, R. Chen, X. Li, Y. Wang, and C. Wang. 2021. Early changes of NLRP3 inflammasome activation after hypoxic-ischemic brain injury in neonatal rats. Int J Clin Exp Pathol 14(2):209-220.

Liu, J., H. Liao, Y. Chen, H. Zhu, X. Li, J. Liu, Q. Xiang, F. Zeng, and Q. Yang. 2022a. Resveratrol Inhibits Oxidative Stress and Regulates M1/M2-Type Polarization of Microglia via Mediation of the Nrf2/Shh Signaling Cascade after OGD/R Injury In Vitro. J Pers Med 12(12)doi: 10.3390/jpm12122087

Liu, Q., M. M. Zhang, M. X. Guo, Q. P. Zhang, N. Z. Li, J. Cheng, S. L. Wang, G. H. Xu, C. F. Li, J. X. Zhu, and L. T. Yi. 2022b. Inhibition of Microglial NLRP3 with MCC950 Attenuates Microglial Morphology and NLRP3/Caspase-1/IL-1β Signaling In Stress-induced Mice. J Neuroimmune Pharmacol 17(3-4):503-514. doi: 10.1007/s11481-021-10037-0

Liu, X., Z. Zhang, J. Ruan, Y. Pan, V. G. Magupalli, H. Wu, and J. Lieberman. 2016. Inflammasome-activated gasdermin D causes pyroptosis by forming membrane pores. Nature 535(7610):153-158. doi: 10.1038/nature18629

Liu, Z., M. Qu, L. Yu, P. Song, and Y. Chang. 2018. Artesunate Inhibits Renal Ischemia-Reperfusion-Mediated Remote Lung Inflammation Through Attenuating ROS-Induced Activation of NLRP3 Inflammasome. Inflammation 41(4):1546-1556. doi: 10.1007/s10753-018-0801-z

Lorek, A., Y. Takei, E. B. Cady, J. S. Wyatt, J. Penrice, A. D. Edwards, D. Peebles, M. Wylezinska, H. Owen-Reece, V. Kirkbride, and et al. 1994. Delayed ("secondary") cerebral energy failure after acute hypoxia-ischemia in the newborn piglet: continuous 48-hour studies by phosphorus magnetic resonance spectroscopy. Pediatr Res 36(6):699-706. doi: 10.1203/00006450-199412000-00003

Luan, P., X. Ding, J. Xu, L. Jiang, Y. Xu, Y. Zhu, R. Li, and J. Zhang. 2020. Salvianolate reduces neuronal apoptosis by suppressing OGD-induced microglial activation. Life Sci 260:118393. doi: 10.1016/j.lfs.2020.118393

Luo, X., H. Zeng, C. Fang, and B. H. Zhang. 2021. N-acetylserotonin Derivative Exerts a Neuroprotective Effect by Inhibiting the NLRP3 Inflammasome and Activating the PI3K/Akt/Nrf2 Pathway in the Model of Hypoxic-Ischemic Brain Damage. Neurochem Res 46(2):337-348. doi: 10.1007/s11064-020-03169-x

Lv, Q., F. Hong, Z. Sun, H. Shen, H. Lu, Y. Jin, L. Mao, and L. Song. 2025. OPA1 modulates NLRP3 inflammasome activation and microglial-mediated neuroinflammation in neonatal hypoxic-ischemic brain injury. J Neuroimmunol 407:578701. doi: 10.1016/j.jneuroim.2025.578701

Lv, Y., B. Sun, X. X. Lu, Y. L. Liu, M. Li, L. X. Xu, C. X. Feng, X. Ding, and X. Feng. 2020. The role of microglia mediated pyroptosis in neonatal hypoxic-ischemic brain damage. Biochem Biophys Res Commun 521(4):933-938. doi: 10.1016/j.bbrc.2019.11.003

Lv, Z., X. Luo, B. Hong, Q. Ye, J. Liu, and Y. Hu. 2022. CBL knockdown protects cardiomyocytes against hypoxia-reoxygenation injury by downregulating GRB2 expression. Exp Ther Med 23(2):188. doi: 10.3892/etm.2022.11111

MacKenzie, S. H., J. L. Schipper, and A. C. Clark. 2010. The potential for caspases in drug discovery. Curr Opin Drug Discov Devel 13(5):568-576.

Mangan, M. S. J., E. J. Olhava, W. R. Roush, H. M. Seidel, G. D. Glick, and E. Latz. 2018. Targeting the NLRP3 inflammasome in inflammatory diseases. Nat Rev Drug Discov 17(8):588-606. doi: 10.1038/nrd.2018.97

Marinelli, S., B. Basilico, M. C. Marrone, and D. Ragozzino. 2019. Microglia-neuron crosstalk: Signaling mechanism and control of synaptic transmission. Semin Cell Dev Biol 94:138-151. doi: 10.1016/j.semcdb.2019.05.017

Marshall, J. S., R. Warrington, W. Watson, and H. L. Kim. 2018. An introduction to immunology and immunopathology. Allergy Asthma Clin Immunol 14(Suppl 2):49. doi: 10.1186/s13223-018-0278-1

McKee, C. M., and R. C. Coll. 2020. NLRP3 inflammasome priming: A riddle wrapped in a mystery inside an enigma. J Leukoc Biol 108(3):937-952. doi: 10.1002/jlb.3mr0720-513r

Mengler, L., A. Khmelinskii, M. Diedenhofen, C. Po, M. Staring, B. P. F. Lelieveldt, and M. Hoehn. 2014. Brain maturation of the adolescent rat cortex and striatum: changes in volume and myelination. Neuroimage 84:35-44. doi: 10.1016/j.neuroimage.2013.08.034

Menu, P., and J. E. Vince. 2011. The NLRP3 inflammasome in health and disease: the good, the bad and the ugly. Clin Exp Immunol 166(1):1-15. doi: 10.1111/j.1365-2249.2011.04440.x

Ni, M., and M. Aschner. 2010. Neonatal rat primary microglia: isolation, culturing, and selected applications. Curr Protoc Toxicol Chapter 12:Unit 12.17. doi: 10.1002/0471140856.tx1217s43

Northington, F. J., D. M. Ferriero, D. L. Flock, and L. J. Martin. 2001. Delayed neurodegeneration in neonatal rat thalamus after hypoxia-ischemia is apoptosis. J Neurosci 21(6):1931-1938. doi: 10.1523/jneurosci.21-06-01931.2001

O'Brien, W. T., L. Pham, G. F. Symons, M. Monif, S. R. Shultz, and S. J. McDonald. 2020. The NLRP3 inflammasome in traumatic brain injury: potential as a biomarker and therapeutic target. J Neuroinflammation 17(1):104. doi: 10.1186/s12974-020-01778-5

O’Brien, W. T., L. Pham, G. F. Symons, M. Monif, S. R. Shultz, and S. J. McDonald. 2020. The NLRP3 inflammasome in traumatic brain injury: potential as a biomarker and therapeutic target. Journal of Neuroinflammation 17(1)doi: 10.1186/s12974-020-01778-5

Osredkar, D., H. Sabir, M. Falck, T. Wood, E. Maes, T. Flatebø, M. Puchades, and M. Thoresen. 2015. Hypothermia Does Not Reverse Cellular Responses Caused by Lipopolysaccharide in Neonatal Hypoxic-Ischaemic Brain Injury. Dev Neurosci 37(4-5):390-397. doi: 10.1159/000430860

Osredkar, D., M. Thoresen, E. Maes, T. Flatebø, M. Elstad, and H. Sabir. 2014. Hypothermia is not neuroprotective after infection-sensitized neonatal hypoxic-ischemic brain injury. Resuscitation 85(4):567-572. doi: 10.1016/j.resuscitation.2013.12.006

Paget, C., E. Doz-Deblauwe, N. Winter, and B. Briard. 2022. Specific NLRP3 Inflammasome Assembling and Regulation in Neutrophils: Relevance in Inflammatory and Infectious Diseases. Cells 11(7)doi: 10.3390/cells11071188

Palomino-Antolin, A., P. Narros-Fernández, V. Farré-Alins, J. Sevilla-Montero, C. Decouty-Pérez, A. B. Lopez-Rodriguez, N. Fernández, L. Monge, A. I. Casas, M. J. Calzada, and J. Egea. 2022. Time-dependent dual effect of NLRP3 inflammasome in brain ischaemia. Br J Pharmacol 179(7):1395-1410. doi: 10.1111/bph.15732

Paolicelli, R. C., A. Sierra, B. Stevens, M. E. Tremblay, A. Aguzzi, B. Ajami, I. Amit, E. Audinat, I. Bechmann, M. Bennett, F. Bennett, A. Bessis, K. Biber, S. Bilbo, M. Blurton-Jones, E. Boddeke, D. Brites, B. Brône, G. C. Brown, O. Butovsky, M. J. Carson, B. Castellano, M. Colonna, S. A. Cowley, C. Cunningham, D. Davalos, P. L. De Jager, B. de Strooper, A. Denes, B. J. L. Eggen, U. Eyo, E. Galea, S. Garel, F. Ginhoux, C. K. Glass, O. Gokce, D. Gomez-Nicola, B. González, S. Gordon, M. B. Graeber, A. D. Greenhalgh, P. Gressens, M. Greter, D. H. Gutmann, C. Haass, M. T. Heneka, F. L. Heppner, S. Hong, D. A. Hume, S. Jung, H. Kettenmann, J. Kipnis, R. Koyama, G. Lemke, M. Lynch, A. Majewska, M. Malcangio, T. Malm, R. Mancuso, T. Masuda, M. Matteoli, B. W. McColl, V. E. Miron, A. V. Molofsky, M. Monje, E. Mracsko, A. Nadjar, J. J. Neher, U. Neniskyte, H. Neumann, M. Noda, B. Peng, F. Peri, V. H. Perry, P. G. Popovich, C. Pridans, J. Priller, M. Prinz, D. Ragozzino, R. M. Ransohoff, M. W. Salter, A. Schaefer, D. P. Schafer, M. Schwartz, M. Simons, C. J. Smith, W. J. Streit, T. L. Tay, L. H. Tsai, A. Verkhratsky, R. von Bernhardi, H. Wake, V. Wittamer, S. A. Wolf, L. J. Wu, and T. Wyss-Coray. 2022. Microglia states and nomenclature: A field at its crossroads. Neuron 110(21):3458-3483. doi: 10.1016/j.neuron.2022.10.020

Peferoen, L. A., D. Y. Vogel, K. Ummenthum, M. Breur, P. D. Heijnen, W. H. Gerritsen, R. M. Peferoen-Baert, P. van der Valk, C. D. Dijkstra, and S. Amor. 2015. Activation status of human microglia is dependent on lesion formation stage and remyelination in multiple sclerosis. J Neuropathol Exp Neurol 74(1):48-63. doi: 10.1097/nen.0000000000000149

Placeres-Uray, F., A. S. Gorthy, M. D. Torres, and C. M. Atkins. 2025. Inhibition of microglia priming by NLRP3 reduces the impact of early life stress and mild TBI. J Neuroinflammation 22(1):185. doi: 10.1186/s12974-025-03512-5

Qin, X., J. Cheng, Y. Zhong, O. K. Mahgoub, F. Akter, Y. Fan, M. Aldughaim, Q. Xie, L. Qin, L. Gu, Z. Jian, X. Xiong, and R. Liu. 2019. Mechanism and Treatment Related to Oxidative Stress in Neonatal Hypoxic-Ischemic Encephalopathy. Front Mol Neurosci 12:88. doi: 10.3389/fnmol.2019.00088

Qiu, Z., Y. He, H. Ming, S. Lei, Y. Leng, and Z. Y. Xia. 2019. Lipopolysaccharide (LPS) Aggravates High Glucose- and Hypoxia/Reoxygenation-Induced Injury through Activating ROS-Dependent NLRP3 Inflammasome-Mediated Pyroptosis in H9C2 Cardiomyocytes. J Diabetes Res 2019:8151836. doi: 10.1155/2019/8151836

Ranjan, A. K., and A. Gulati. 2023. Advances in Therapies to Treat Neonatal Hypoxic-Ischemic Encephalopathy. J Clin Med 12(20)doi: 10.3390/jcm12206653

Rayamajhi, M., Y. Zhang, and E. A. Miao. 2013. Detection of pyroptosis by measuring released lactate dehydrogenase activity. Methods Mol Biol 1040:85-90. doi: 10.1007/978-1-62703-523-1_7

Rice, J. E., 3rd, R. C. Vannucci, and J. B. Brierley. 1981. The influence of immaturity on hypoxic-ischemic brain damage in the rat. Ann Neurol 9(2):131-141. doi: 10.1002/ana.410090206

Rocha-Ferreira, E., and M. Hristova. 2016. Plasticity in the Neonatal Brain following Hypoxic-Ischaemic Injury. Neural Plast 2016:4901014. doi: 10.1155/2016/4901014

Rosomoff, H. L., and D. A. Holaday. 1954. Cerebral blood flow and cerebral oxygen consumption during hypothermia. Am J Physiol 179(1):85-88. doi: 10.1152/ajplegacy.1954.179.1.85

Roy, A., S. Choudhury, R. Banerjee, P. Basu, and H. Kumar. 2021. Soluble LAG-3 and Toll-interacting protein: Novel upstream neuro-inflammatory markers in Parkinson's disease. Parkinsonism Relat Disord 91:121-123. doi: 10.1016/j.parkreldis.2021.09.019

Sabir, H., E. Scull-Brown, X. Liu, and M. Thoresen. 2012. Immediate hypothermia is not neuroprotective after severe hypoxia-ischemia and is deleterious when delayed by 12 hours in neonatal rats. Stroke 43(12):3364-3370. doi: 10.1161/strokeaha.112.674481

Sagulenko, V., S. J. Thygesen, D. P. Sester, A. Idris, J. A. Cridland, P. R. Vajjhala, T. L. Roberts, K. Schroder, J. E. Vince, J. M. Hill, J. Silke, and K. J. Stacey. 2013. AIM2 and NLRP3 inflammasomes activate both apoptotic and pyroptotic death pathways via ASC. Cell Death Differ 20(9):1149-1160. doi: 10.1038/cdd.2013.37

Schlaepfer, D. D., S. K. Hanks, T. Hunter, and P. v. d. Geer. 1994. Integrin-mediated signal transduction linked to Ras pathway by GRB2 binding to focal adhesion kinase. Nature 372(6508):786-791. doi: 10.1038/372786a0

Seemann, S., F. Zohles, and A. Lupp. 2017. Comprehensive comparison of three different animal models for systemic inflammation. J Biomed Sci 24(1):60. doi: 10.1186/s12929-017-0370-8

Serdar, M., K. Kempe, R. Herrmann, D. Picard, M. Remke, J. Herz, I. Bendix, U. Felderhoff-Müser, and H. Sabir. 2020. Involvement of CXCL1/CXCR2 During Microglia Activation Following Inflammation-Sensitized Hypoxic-Ischemic Brain Injury in Neonatal Rats. Front Neurol 11:540878. doi: 10.3389/fneur.2020.540878

Serdar, M., K. Kempe, M. Rizazad, J. Herz, I. Bendix, U. Felderhoff-Müser, and H. Sabir. 2019. Early Pro-inflammatory Microglia Activation After Inflammation-Sensitized

Hypoxic-Ischemic Brain Injury in Neonatal Rats. Front Cell Neurosci 13:237. doi: 10.3389/fncel.2019.00237

Sharif, H., L. Wang, W. L. Wang, V. G. Magupalli, L. Andreeva, Q. Qiao, A. V. Hauenstein, Z. Wu, G. Núñez, Y. Mao, and H. Wu. 2019. Structural mechanism for NEK7-licensed activation of NLRP3 inflammasome. Nature 570(7761):338-343. doi: 10.1038/s41586-019-1295-z

Shen, H., Q. Zhang, Q. Lv, H. Liu, C. Wang, F. Meng, Y. Guo, J. Pei, C. Yu, J. Tie, X. Chen, C. Zhang, H. Yu, and X. Wang. 2025a. Chronic ethanol exposure induces hippocampal neuroinflammation and neuronal damage via the astrocytic RUNX1/TOLLIP/TLR3 pathway. Brain Behav Immun 130:106081. doi: 10.1016/j.bbi.2025.106081

Shen, Q., S. Wang, K. Wu, L. Wang, W. Gong, G. Lu, W. Chen, C. Yuan, B. Tu, W. Li, Y. Wang, and W. Yang. 2025b. Identification of Grb2 protein as a potential mediator of macrophage activation in acute pancreatitis based on bioinformatics and experimental verification. Front Immunol 16:1575880. doi: 10.3389/fimmu.2025.1575880

Skrzypczak-Wiercioch, A., and K. Sałat. 2022. Lipopolysaccharide-Induced Model of Neuroinflammation: Mechanisms of Action, Research Application and Future Directions for Its Use. Molecules 27(17)doi: 10.3390/molecules27175481

Song, N., and T. Li. 2018. Regulation of NLRP3 Inflammasome by Phosphorylation. Front Immunol 9:2305. doi: 10.3389/fimmu.2018.02305

Squire, L. R., and S. Zola-Morgan. 1991. The medial temporal lobe memory system. Science 253(5026):1380-1386. doi: 10.1126/science.1896849

Stratoulias, V., J. L. Venero, M. Tremblay, and B. Joseph. 2019. Microglial subtypes: diversity within the microglial community. Embo j 38(17):e101997. doi: 10.15252/embj.2019101997

Swanson, K. V., M. Deng, and J. P. Ting. 2019. The NLRP3 inflammasome: molecular activation and regulation to therapeutics. Nat Rev Immunol 19(8):477-489. doi: 10.1038/s41577-019-0165-0

Tagin, M., H. Abdel-Hady, S. ur Rahman, D. V. Azzopardi, and A. J. Gunn. 2015. Neuroprotection for Perinatal Hypoxic Ischemic Encephalopathy in Low- and Middle-Income Countries. J Pediatr 167(1):25-28. doi: 10.1016/j.jpeds.2015.02.056

Tan, Y. L., Y. Yuan, and L. Tian. 2020. Microglial regional heterogeneity and its role in the brain. Mol Psychiatry 25(2):351-367. doi: 10.1038/s41380-019-0609-8

Tetorou, K., C. Sisa, A. Iqbal, K. Dhillon, and M. Hristova. 2021. Current Therapies for Neonatal Hypoxic-Ischaemic and Infection-Sensitised Hypoxic-Ischaemic Brain Damage. Front Synaptic Neurosci 13:709301. doi: 10.3389/fnsyn.2021.709301

Thayyil, S., S. Pant, P. Montaldo, D. Shukla, V. Oliveira, P. Ivain, P. Bassett, R. Swamy, J. Mendoza, M. Moreno-Morales, P. J. Lally, N. Benakappa, P. Bandiya, I. Shivarudhrappa, J. Somanna, U. B. Kantharajanna, A. Rajvanshi, S. Krishnappa, P. K. Joby, K. Jayaraman, R. Chandramohan, C. N. Kamalarathnam, M. Sebastian,

I. A. Tamilselvam, U. D. Rajendran, R. Soundrarajan, V. Kumar, H. Sudarsanan, P. Vadakepat, K. Gopalan, M. Sundaram, A. Seeralar, P. Vinayagam, M. Sajjid, M. Baburaj, K. D. Murugan, B. P. Sathyanathan, E. S. Kumaran, J. Mondkar, S. Manerkar, A. R. Joshi, K. Dewang, S. M. Bhisikar, P. Kalamdani, V. Bichkar, S. Patra, K. Jiwnani, M. Shahidullah, S. C. Moni, I. Jahan, M. A. Mannan, S. K. Dey, M. N. Nahar, M. N. Islam, K. H. Shabuj, R. Rodrigo, S. Sumanasena, T. Abayabandara-Herath, G. K. Chathurangika, J. Wanigasinghe, R. Sujatha, S. Saraswathy, A. Rahul, S. J. Radha, M. K. Sarojam, V. Krishnan, M. K. Nair, S. Devadas, S. Chandriah, H. Venkateswaran, C. Burgod, M. Chandrasekaran, G. Atreja, P. Muraleedharan, J. A. Herberg, W. K. Kling Chong, N. J. Sebire, R. Pressler, S. Ramji, and S. Shankaran. 2021. Hypothermia for moderate or severe neonatal encephalopathy in low-income and middle-income countries (HELIX): a randomised controlled trial in India, Sri Lanka, and Bangladesh. Lancet Glob Health 9(9):e1273-e1285. doi: 10.1016/s2214-109x(21)00264-3

Turvey, S. E., and D. H. Broide. 2010. Innate immunity. J Allergy Clin Immunol 125(2 Suppl 2):S24-32. doi: 10.1016/j.jaci.2009.07.016

Vannucci, R. C. 1990. Experimental biology of cerebral hypoxia-ischemia: relation to perinatal brain damage. Pediatr Res 27(4 Pt 1):317-326. doi: 10.1203/00006450-199004000-00001

Vannucci, R. C., J. Towfighi, and S. J. Vannucci. 2004. Secondary energy failure after cerebral hypoxia-ischemia in the immature rat. J Cereb Blood Flow Metab 24(10):1090-1097. doi: 10.1097/01.Wcb.0000133250.03953.63

Wahl, D., S. J. Risen, S. C. Osburn, T. Emge, S. Sharma, V. S. Gilberto, A. Chatterjee, P. Nagpal, J. A. Moreno, and T. J. LaRocca. 2024. Nanoligomers targeting NF-κB and NLRP3 reduce neuroinflammation and improve cognitive function with aging and tauopathy. Journal of Neuroinflammation 21(1):182. doi: 10.1186/s12974-024-03182-9

Wan, N., X. Liu, X. J. Zhang, Y. Zhao, G. Hu, F. Wan, R. Zhang, X. Zhu, H. Xia, and H. Li. 2015. Toll-interacting protein contributes to mortality following myocardial infarction through promoting inflammation and apoptosis. Br J Pharmacol 172(13):3383-3396. doi: 10.1111/bph.13130

Wang, L., W. Ren, Q. Wu, T. Liu, Y. Wei, J. Ding, C. Zhou, H. Xu, and S. Yang. 2022a. NLRP3 Inflammasome Activation: A Therapeutic Target for Cerebral Ischemia-Reperfusion Injury. Front Mol Neurosci 15:847440. doi: 10.3389/fnmol.2022.847440

Wang, P., H. Qian, M. Xiao, and J. Lv. 2023a. Role of signal transduction pathways in IL-1β-induced apoptosis: Pathological and therapeutic aspects. Immun Inflamm Dis 11(1):e762. doi: 10.1002/iid3.762

Wang, X., S. Chen, L. Zhao, and X. Shi. 2021. Protective effect of combination of anakinra and MCC950 against acute lung injury is achieved through suppression of the NF-κB-mediated-MAPK and NLRP3-caspase pathways. Int Immunopharmacol 97:107506. doi: 10.1016/j.intimp.2021.107506

Wang, Y., Y. J. Liu, M. M. Zhang, H. Zhou, Y. H. Gao, W. J. Cheng, Z. W. Ye, Z. Y. Yuan, G. H. Xu, C. F. Li, and L. T. Yi. 2022b. CY-09 Alleviates the Depression-like Behaviors via Inhibiting NLRP3 Inflammasome-Mediated Neuroinflammation in Lipopolysaccharide-Induced Mice. ACS Chem Neurosci 13(23):3291-3302. doi: 10.1021/acschemneuro.2c00348

Wang, Y., X. Xu, X. Shui, R. Ren, and Y. Liu. 2024. Molecular subtype identification of cerebral ischemic stroke based on ferroptosis-related genes. Sci Rep 14(1):9350. doi: 10.1038/s41598-024-53327-2

Wang, Z., X. Feng, G. Zhang, H. Li, F. Zhou, Y. Xie, T. Li, C. Zhao, W. Luo, Y. Xiong, and Y. Wu. 2023b. Artesunate ameliorates ligature-induced periodontitis by attenuating NLRP3 inflammasome-mediated osteoclastogenesis and enhancing osteogenic differentiation. Int Immunopharmacol 123:110749. doi: 10.1016/j.intimp.2023.110749

Wen, W., T. Sanelli, W. Ge, W. Strong, and M. J. Strong. 2006. Activated microglial supernatant induced motor neuron cytotoxicity is associated with upregulation of the TNFR1 receptor. Neurosci Res 55(1):87-95. doi: 10.1016/j.neures.2006.02.004

Wilhelmsen, K., A. Deshpande, S. Tronnes, M. Mahanta, M. Banicki, M. Cochran, S. Cowdin, K. Fortney, G. Hartman, R. E. Hughes, R. Montgomery, C. P. Portillo, P. Rubin, T. Salazar, Y. Wang, S. Yan, B. A. Morgan, A. Duisembekova, R. Riou, M. Marleaux, I. V. Hochheiser, H. Buthmann, D. Ferber, J. Torp, W. Wang, M. Cranston, C. M. McKee, T. J. Mawhinney, E. C. McKay, F. K. Eroglu, J. Kümmerle-Deschner, A. N. R. Weber, B. F. Py, M. Geyer, and R. C. Coll. 2025. Discovery of potent and selective inhibitors of human NLRP3 with a novel mechanism of action. J Exp Med 222(11)doi: 10.1084/jem.20242403

Wu, X., B. Wang, Y. Zhou, Z. Yang, L. Jiang, Z. Kou, J. Li, X. Ma, and J. Song. 2023a. NLRP3 inflammasome inhibitor MCC950 reduces cerebral ischemia/reperfusion induced neuronal ferroptosis. Neurosci Lett 795:137032. doi: 10.1016/j.neulet.2022.137032

Wu, Y., W. Wang, X. Qiu, Z. Lu, W. Ji, J. Shen, H. Peng, R. Zhao, J. Wang, T. Zhang, J. Yang, and X. Zhang. 2023b. A STIR nucleic acid drug delivery system for stirring phenotypic switch of microglia in Parkinson's disease treatments. Nano Research 16(5):7216-7226. doi: 10.1007/s12274-022-5353-5

Xia, S., L. R. t. Hollingsworth, and H. Wu. 2020. Mechanism and Regulation of Gasdermin-Mediated Cell Death. Cold Spring Harb Perspect Biol 12(3)doi: 10.1101/cshperspect.a036400

Xiao, A. J., W. Chen, B. Xu, R. Liu, E. Turlova, A. Barszczyk, C. L. Sun, L. Liu, M. Deurloo, G. L. Wang, Z. P. Feng, and H. S. Sun. 2014. Marine compound xyloketal B reduces neonatal hypoxic-ischemic brain injury. Mar Drugs 13(1):29-47. doi: 10.3390/md13010029

Xie, B., S. Li, W. Bai, Z. Li, and F. Lou. 2023. Artesunate Alleviates Hyperoxia-Induced Lung Injury in Neonatal Mice by Inhibiting NLRP3 Inflammasome Activation. Evid Based Complement Alternat Med 2023:7603943. doi: 10.1155/2023/7603943

Yan, W., Y. Shen, J. Huang, L. Lu, and Q. Zhang. 2021. MCC950 Ameliorates Acute Liver Injury Through Modulating Macrophage Polarization and Myeloid-Derived Suppressor Cells Function. Front Med (Lausanne) 8:752223. doi: 10.3389/fmed.2021.752223

Yang, C. C., L. D. Hsiao, H. C. Tseng, C. M. Kuo, and C. M. Yang. 2020a. Pristimerin Inhibits MMP-9 Expression and Cell Migration Through Attenuating NOX/ROS-Dependent NF-κB Activation in Rat Brain Astrocytes Challenged with LPS. J Inflamm Res 13:325-341. doi: 10.2147/jir.S252659

Yang, J., L. Wise, and K. I. Fukuchi. 2020b. TLR4 Cross-Talk With NLRP3 Inflammasome and Complement Signaling Pathways in Alzheimer's Disease. Front Immunol 11:724. doi: 10.3389/fimmu.2020.00724

Yang, L., Y. Zhang, X. Yu, D. Li, N. Liu, X. Xue, and J. Fu. 2023. Periventricular Microglia Polarization and Morphological Changes Accompany NLRP3 Inflammasome-Mediated Neuroinflammation after Hypoxic-Ischemic White Matter Damage in Premature Rats. J Immunol Res 2023:5149306. doi: 10.1155/2023/5149306

Yang, Y., H. Wang, M. Kouadir, H. Song, and F. Shi. 2019. Recent advances in the mechanisms of NLRP3 inflammasome activation and its inhibitors. Cell Death Dis 10(2):128. doi: 10.1038/s41419-019-1413-8

Ye, Y., T. Jin, X. Zhang, Z. Zeng, B. Ye, J. Wang, Y. Zhong, X. Xiong, and L. Gu. 2019. Meisoindigo Protects Against Focal Cerebral Ischemia-Reperfusion Injury by Inhibiting NLRP3 Inflammasome Activation and Regulating Microglia/Macrophage Polarization via TLR4/NF-κB Signaling Pathway. Frontiers in Cellular Neuroscience Volume 13 - 2019(Original Research) doi: 10.3389/fncel.2019.00553

Yoon, S. H., C. Y. Kim, E. Lee, C. Lee, K. S. Lee, J. Lee, H. Park, B. Choi, I. Hwang, J. Kim, T. G. Kim, J. Son, Y. M. Hyun, S. Hong, and J. W. Yu. 2025. Microglial NLRP3-gasdermin D activation impairs blood-brain barrier integrity through interleukin-1β-independent neutrophil chemotaxis upon peripheral inflammation in mice. Nat Commun 16(1):699. doi: 10.1038/s41467-025-56097-1

Ystgaard, M. B., K. Scheffler, R. Suganthan, M. Bjørås, T. Ranheim, E. L. Sagen, B. Halvorsen, O. D. Saugstad, and A. Yndestad. 2019. Neuromodulatory Effect of NLRP3 and ASC in Neonatal Hypoxic Ischemic Encephalopathy. Neonatology 115(4):355-362. doi: 10.1159/000497200

Ystgaard, M. B., Y. Sejersted, E. M. Løberg, E. Lien, A. Yndestad, and O. D. Saugstad. 2015. Early Upregulation of NLRP3 in the Brain of Neonatal Mice Exposed to Hypoxia-Ischemia: No Early Neuroprotective Effects of NLRP3 Deficiency. Neonatology 108(3):211-219. doi: 10.1159/000437247

Zhang, L., B. Liu, J. Han, T. Wang, and L. Han. 2020. Competing endogenous RNA network analysis for screening inflammation-related long non-coding RNAs for acute ischemic stroke. Mol Med Rep 22(4):3081-3094. doi: 10.3892/mmr.2020.11415

Zhang, X., J. Guo, Y. Zhang, S. Zhao, J. Chen, J. Jiang, X. Hu, B. Zhou, and K. Zhang. 2025. Intranasal delivery of LB244-loaded M2 microglia membrane nanoparticles

for targeted treatment of neuroinflammation after I/R brain injury. Mater Today Bio 35:102412. doi: 10.1016/j.mtbio.2025.102412

Zhang, X., Z. Wang, Y. Zheng, Q. Yu, M. Zeng, L. Bai, L. Yang, M. Guo, X. Jiang, and J. Gan. 2023. Inhibitors of the NLRP3 inflammasome pathway as promising therapeutic candidates for inflammatory diseases (Review). Int J Mol Med 51(4)doi: 10.3892/ijmm.2023.5238

Zheng, Q., H. Zhao, D. Jia, X. Han, Z. Liu, and M. Zhao. 2021. Overexpression of TOLLIP Protects against Acute Kidney Injury after Paraquat Intoxication through Inhibiting NLRP3 Inflammasome Activation Modulated by Toll-Like Receptor 2/4 Signaling. Mediators Inflamm 2021:5571272. doi: 10.1155/2021/5571272

Zhou, K. Q., S. K. Dhillon, L. Bennet, A. J. Gunn, and J. O. Davidson. 2022. Targeting Persistent Neuroinflammation after Hypoxic-Ischemic Encephalopathy-Is Exendin-4 the Answer? Int J Mol Sci 23(17)doi: 10.3390/ijms231710191

Zhou, T., Z. Huang, X. Sun, X. Zhu, L. Zhou, M. Li, B. Cheng, X. Liu, and C. He. 2017. Microglia Polarization with M1/M2 Phenotype Changes in rd1 Mouse Model of Retinal Degeneration. Front Neuroanat 11:77. doi: 10.3389/fnana.2017.00077

9. Appendix

Supplementary Table 1: Overview of animal experiments including gender distribution in treatment groups. Listed details about experiments and animal number. * Animals not sacrificed, but further kept for other analyses.

Experiment	Groups	Time points for		Analysis method	Animals		
		Injection	Analysis		Analyzed	♂ / ♀	Died
Hypoxia-ischemia/ Time point analysis	Sham		4 h	WB	6	6/0	-
	HI/NT		4 h	WB	12	5/7	-
	Sham		12 h	WB	6	3/2	-
	HI/NT		12 h	WB	11	2/9	2
	Sham		24 h	WB	6	6/0	-
	HI/NT		24 h	WB	12	7/5	-
	Sham		36 h	WB	6	2/3	-
	HI/NT		36 h	WB	11	4/7	2
	Sham		48 h	WB	6	3/2	-
	HI/NT		48 h	WB	10	5/5	-
Hypoxia-ischemia/ Inhibitor treatment	Sham		24 h	WB	5	2/3	-
	HI/Vehicle	- 30 min/ + 24 h	24 h	WB	16	8/8	-
	HI/Crid5		24 h	WB	16	8/8	-
	Sham		24 h	MACS	6	3/3	-
	HI/Vehicle	- 30 min/ + 24 h	24 h	MACS	12	6/6	-
	HI/Crid5		24 h	MACS	12	6/6	-
	Sham		48 h	WB	5	3/2	-
	HI/Vehicle	- 30 min/ + 24 h	48 h	WB	9	5/4	3
	HI/Crid5		48 h	WB	7	3/4	3
	HI/Crid10		48 h	WB	7	5/2	3
	HI/Crid20		48 h	WB	6	4/2	4
	HI/Vehicle	+ 1 h/ + 24 h	48 h	WB	8	4/4	1
	HI/Crid5		48 h	WB	9	6/3	-
	HI/Crid10		48 h	WB	8	5/3	-
	HI/Crid20		48 h	WB	8	6/2	-
	Sham		P 14	MRI	5*	2/3	-
	HI/Vehicle	- 30 min/ + 24 h	P 14	MRI	12*	7/5	-
	HI/Crid5		P 14	MRI	12*	7/5	-
	Sham		P 46-48	Catwalk	5*	2/3	-
	HI/Vehicle	- 30 min/ + 24 h	P 46-48	Catwalk	12*	7/5	-
	HI/Crid5		P 46-48	Catwalk	12*	7/5	-
	Sham		P 74-76	NOR	5*	2/3	-
	HI/Vehicle	- 30 min/ + 24 h	P 74-76	NOR	12*	7/5	-
	HI/Crid5		P 74-76	NOR	12*	7/5	-
	Sham		P 81	MRI	5*	2/3	-
	HI/Vehicle	- 30 min/ + 24 h	P 81	MRI	12*	7/5	-
	HI/Crid5		P 81	MRI	12*	7/5	-

Supplementary Table 2: Overview of pilot experiments treating HIE with the NLRP3 inhibitor Crid3. Listed details about concentration and injection time points of Crid3.

Experiments	**Concentration**	**Injection time points**						**Outcome/ inhibition**
		before HI	**after HI**					
1st experiment	50 mg/kg		0 h	4 h		24 h		not effective
2nd experiment	25 mg/kg		0 h	3 h	6 h	24 h		
3rd experiment	20 mg/kg	30 min	0 h		6 h	24 h		
4th experiment	3 mg/kg			1h				
	5 mg/kg			1h				
5th experiment	10 mg/kg	30 min				24 h	48 h	

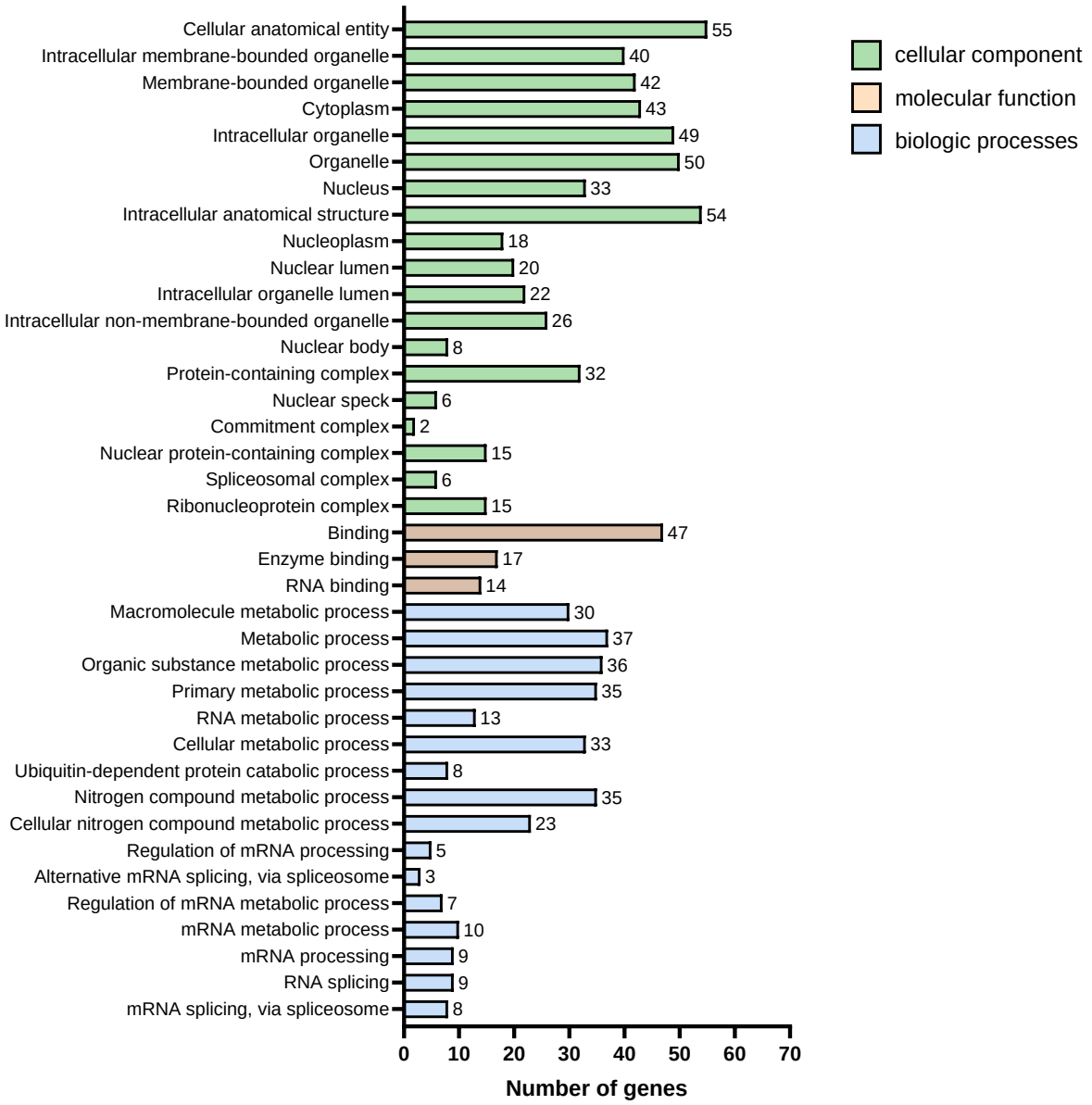

Supplementary Figure 1: Gene ontology analysis of NLRP3-specific synthesized proteins in microglia after OGD. Primary microglia were exposed to 6 h of OGD (0.1 % O_2). 30 min before, cells were treated with 1 µM Crid3 to inhibit NLRP3 (OC). During 24 h of reoxygenation, the protein synthesis was labelled with AHA. Supernatant was collected and processed for MS analysis. Gene ontology analysis was performed with string-db.org.

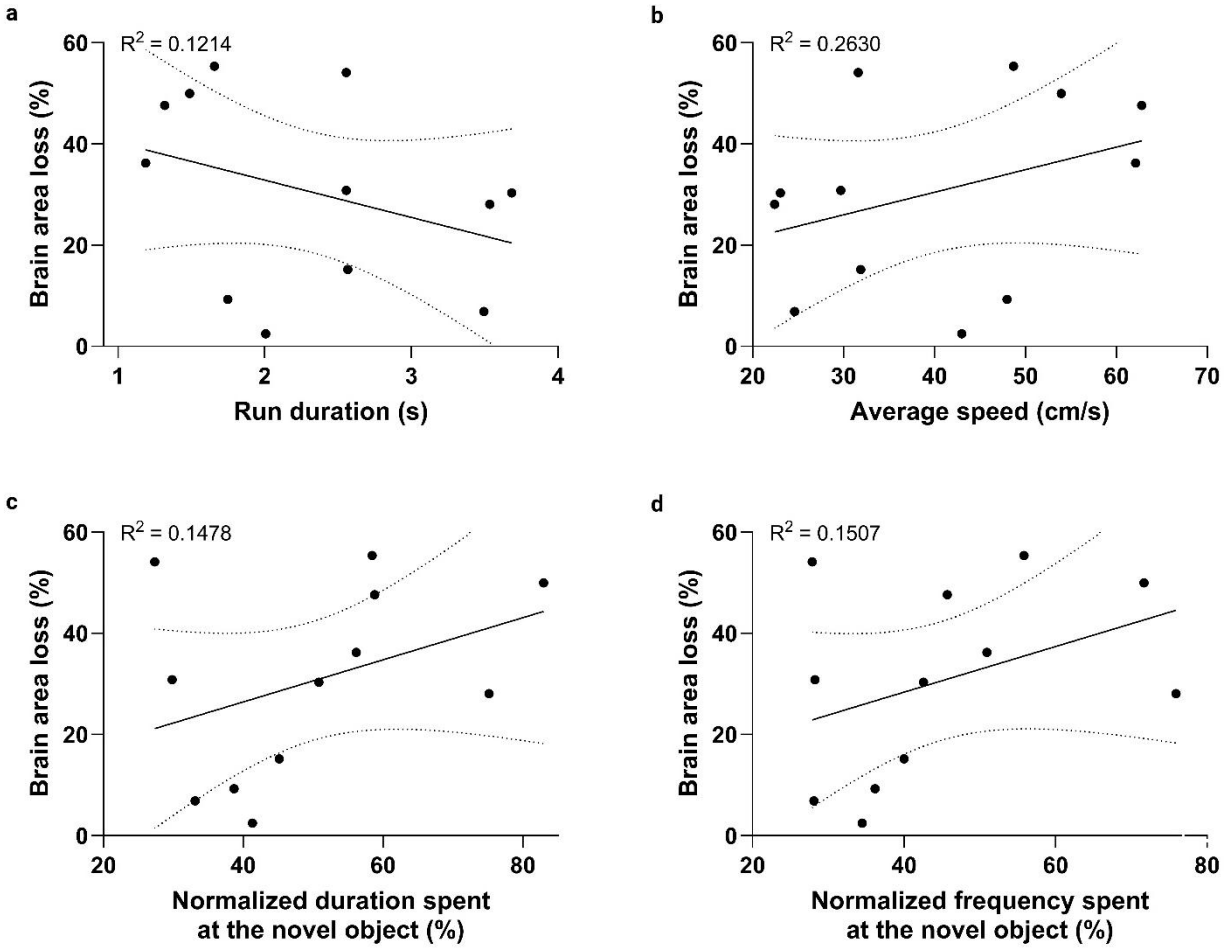

Supplementary Figure 2: Correlation of behavior with brain damage assessments. **a-b** Motoric behavior results from CatWalk correlated to brain area loss of HI/Vehicle treated animals. **c-d** Cognitive behavior results from novel object recognition correlated to brain area loss of HI/Vehicle treated animals. Non-parametric Spearman correlation was performed. Linear regression is represented with a 95 % interval and the coefficient of determination (R^2).

10. Statement of own contribution

The study was carried out at the DZNE institute in Bonn under the supervision of Prof. Dr. med. Hemmen Sabir. The study was designed by Prof. Dr. med. Hemmen Sabir (PI), Dr. Maria Eugenia Bernis (Postdoc) and me, Hannah Burkard (PhD student). The animal experiments were carried out by Prof. Dr. med. Hemmen Sabir (PI), Dr. Maria Eugenia Bernis (Postdoc), Anna-Sophie Bremer (PhD student), Elke Maes (technical assistant) and me. The behavioral assays were performed by Anna-Sophie Bremer (PhD student) and me. The animal tissue was collected by Anna-Sophie Bremer (PhD student), Elke Maes (technical assistant) and me. The subsequent analyses of tissue were carried out by me. Primary microglia cell culture was conducted by me, as well as further experiments and analyses of the cells. Microglia isolation after animal experiments was carried out by Dr. Maria Eugenia Bernis (Postdoc), Anna-Sophie Bremer (PhD student), Elke Maes (technical assistant) and me. Following FACS analysis was performed by Dr. Maria Eugenia Bernis (Postdoc) and RNA isolation and RT-PCR were performed by me. The sample labelling for proteomic analysis was carried out by me. The mass spectrometry was carried out by the laboratory of Dr. Felix Meissner of the University Hospital Bonn by Dr. Jonas Walter (Postdoc). Data analysis, interpretation and statistical evaluation were carried out by me. I confirm that I have written this thesis independently and have not used any sources or aids other than those specified by me.

11. Acknowledgements

First and foremost, I would like to express my sincere gratitude to my supervisor, Prof. Dr. med. Hemmen Sabir, for giving me the opportunity to conduct my doctoral research in his laboratory on such a relevant topic. I am thankful for his continuous support and interesting discussions. His door was always open for questions and feedback. I am also grateful for encouraging my participation in scientific conferences which shaped my independent scientific work and supported the development of this study.

I am also deeply grateful to my second examiner, Prof. Dr. rer. medic Ivo Bendix, as well as to my third and fourth examiners, Prof. Dr. rer. med. Andreas Müller and Prof. Dr. med. Albert Becker. By participating in the annual progress meetings, they continuously accompanied this project and enriched it with constructive feedback and valuable scientific input.

Special thanks go to Dr. Maria Eugenia Bernis, who served as my main contact throughout this project. Her advice and practical support were invaluable, and I truly appreciate her taking the time for any questions and for encouragement in crucial moments.

I would also like to thank all current and former members of our research group. In particular, I am deeply grateful to my fellow PhD colleague Anna-Sophie Bremer, with whom I shared this journey side by side – without her, many difficult meetings and frustrating results would have been far harder to endure. I would also like to thank Elke Maes for her encouraging and compassionate nature, as well as her constant support, which meant a great deal to me, and my former colleagues Margit Zweyer and Kora Grzelak for their invaluable help and the enjoyable company.

Furthermore, I would like to thank the Animal Facility and the Microscopy Facility for their support and technical expertise, which were essential for the success of this work.

Finally, I am profoundly grateful to my family and friends for their encouragement, understanding, and support throughout these years. A very special thank you goes to Dominik, who patiently listened to my worries every single day and always had something uplifting or funny to say, helping me through the entire journey.

This thesis is dedicated to all of them.